Nucleon form factors from Lattice QCD for neutrino oscillation experiments

DISSERTATION ZUR ERLANGUNG DES DOKTORGRADES
DER NATURWISSENSCHAFTEN (DR. RER. NAT.) DER FAKULTÄT
FÜR PHYSIK DER UNIVERSITÄT REGENSBURG

vorgelegt von

LORENZO BARCA

aus

COSENZA

im Jahr 2022

Der Promotionsgesuch wurde eingereicht am: *30.09.2022*
Datum Promotionskolloquium: *23.11.2022*
Die Arbeit wurde angeleitet von: *Prof. Dr. Gunnar Bali*

Vorsitzender: *Prof. Dr. Jörg Wunderlich*
1. Gutachter: *Prof. Dr. Gunnar Bali*
2. Gutachter: *Prof. Dr. Christoph Lehner*
weiterer Prüfer: *Prof. Dr. Juan Diego Urbina*

Abstract

The investigation of neutrino oscillations is an ongoing world-leading research that aims to understand fundamental neutrino properties. In particular, the observation that neutrinos can oscillate from one flavor to another suggests that these elementary particles have a very small but non-zero mass. However, high precision is required to reconstruct the neutrino energy with Monte Carlo generators and extract parameters such as the CP violating phase δ. The experiments are most frequently built such that the neutrino beams scatter against heavy nuclei targets and these cross sections are non-trivial to parametrize, depending on the energy scale at which the experiment is carried out. Some of the parameters that enter in these cross sections and that represent systematic uncertainties are the so-called nucleon form factors. These functions can be extracted non-perturbatively with lattice simulations by simulating the theory that describes the strong interactions, also known as Quantum ChromoDynamics (QCD). One of the major challenges faced in the lattice QCD determination of the nucleon matrix elements is excited state contamination, particularly nucleon-pion contamination. State-of-the-art analyses take into account this contamination with multistate fits based on Chiral Perturbation Theory, which is an effective field theory where the degrees of freedom are pion and nucleon fields. In this project, we confront the problem directly. Since the primary source of contamination is understood to be related to nucleon-pion states production, we compute this contribution with lattice QCD simulations and consider it for the ground state. The outcome on a single ensemble is promising and confirms the ChPT-inspired approaches. Furthermore, the nucleon-pion term that is computed and taken into account is proportional to the matrix element $\langle N\pi|\mathscr{J}|N\rangle$, which is phenomenologically interesting by itself as it enters in the CC1π and NC1π experimental processes, which occur in the neutrino oscillation experiments and are considered in the event reconstruction. This pilot study represents the first initiative for determining nucleon matrix elements with the variational method with a basis made of nucleon and nucleon-pion operators. We plan to continue this work by including more statistics, extending it to more ensembles, and computing for the first time $\langle N\pi|\mathscr{J}|N\rangle$.

Dedico questo traguardo alla mia amata famiglia,
che ha visto compiere i miei primi passi
e mi ha aiutato a superare tanti momenti di difficolta'.

CONTENTS

CHAPTER

ONE

INTRODUCTION

The introduction is organised as follows.

In Sec. 1.1, I will introduce the current theory that describes the interactions of fundamental particles. In Sec. 1.2 and 1.3, I will discuss processes that play an important role in some of the world-leading experiments in particle physics. In Sec. 1.4, I will introduce neutrino oscillations whose experimental discovery made a great impact and I will review some of the most important experiments that are investigating this phenomenon.

In the final section, I will motivate my research project by emphasising the importance of the quantities that I compute and the role they play in these experiments.

1.1 The Standard Model: a brief introduction

The role of physics is to describe the events that occur in nature in terms of simpler phenomena. However, the deeper one digs into the matter, the more there is yet to understand.

In the last centuries, we have learned that the ordinary matter in the Universe is made up of atoms, which are composed of nuclei and electrons. We have discovered that nuclei are composed of particles we call protons and neutrons, which were understood to be elementary until the last century. Today, we know they are composite and that they are made up of more elementary particles we call quarks and gluons.

There are other elementary particles in nature, and at the current level of understanding they interact through four fundamental forces: the electromagnetic, weak, strong, and gravitational forces. Some particles interact only through a single force, while others interact via different fundamental forces.

The theory of particle physics that describes the first three of the four fundamental forces is the Standard Model. Understanding its limitations is very important to investigate any sign of physics that goes beyond it. Describing the Standard Model with deep care would take more

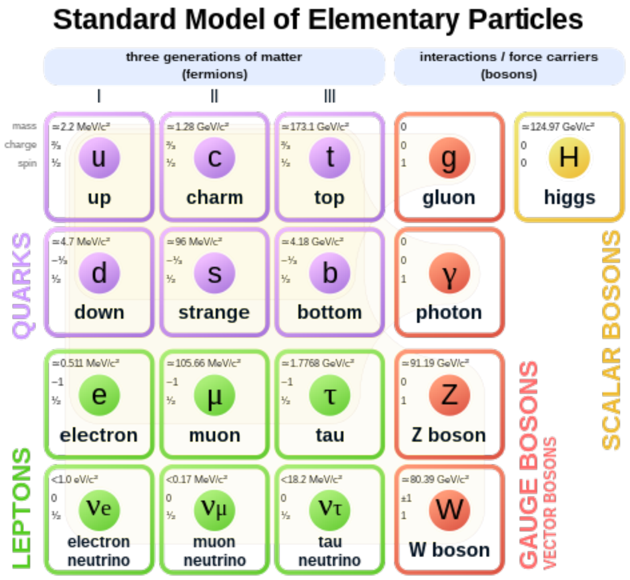

Figure 1.1:
Classification of elementary particles in the Standard Model for ordinary matter. For each lepton, there corresponds an antilepton that forms the antimatter.

than one book. Therefore I limit the content and mention the parts I retain that are essential for this work. According to this model, ordinary matter is composed of elementary particles, divided into fermions and bosons; see Fig. 1.1 for the classification. Following the spin-statistics theorem, the latter have integer spin, and the fundamental bosons are the gluon, the photon, the Higgs, the Z-boson, and the $W^{\pm}$ bosons. The fermions have half-integer spin, and the elementary ones are classified into quarks and leptons.

According to the Standard Model, only quarks interact strongly, i.e. via strong interactions because unlike leptons, they possess color charge. In particular, due to a phenomenon called confinement, which can be explained through the theory of strong interactions, the quarks cannot be isolated, and they are confined within composite particles, which are called hadrons.

The mesons (one quark and one antiquark) and the baryons (three quarks) are the two main types of hadrons. The two most well-known baryons are the proton and the neutron. The particles interact by exchanging gauge bosons and in the case of weak interactions, the mediators are the $W^{\pm}$ and Z bosons, which were discovered in 1983 with the experiments UA1 and UA2, see [23, 32]. As shown in from Fig. 1.1, the neutrinos are in the last row. These are elementary particles that interact only via the weak force, and very recently, experiments have found that they have a mass. Still, it is so tiny that it is very challenging to measure.

For the following sections, I will focus on unresolved questions about the nature of the neutrinos and the world-leading experiments that address these questions.

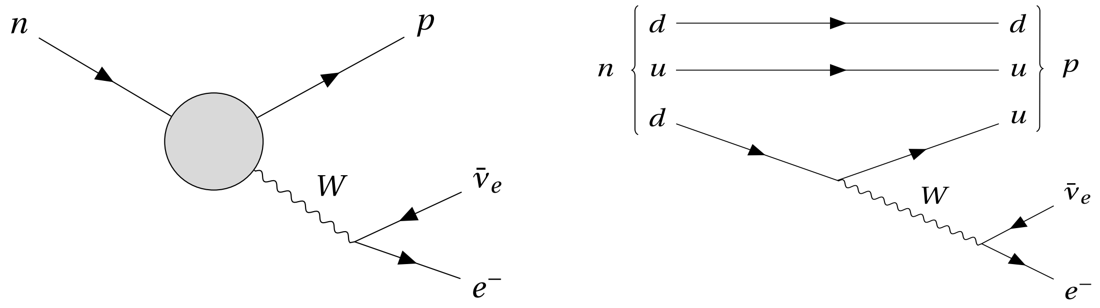

Figure 1.2:
The decay of a free neutron to a proton. On the left, the interaction is seen at the level of the baryons that exchange a $W^{\pm}$-boson. On the right, the nucleons are written in terms of their constituent (valence) quarks, and we see that there are two spectator quarks and one active quark d that changes into u by the exchange of a $W^{\pm}$ boson. The Feynman diagrams were created using the package described in [71].

1.2 Neutron β-decay

In 1930, Wolfgang Pauli postulated the existence of a neutral particle, the neutrino, to explain how the neutron β-decay could conserve energy, momentum, and angular momentum. The β-decay is the following process:

$$n \to p + e^- + \bar{\nu}_e \,, \tag{1.1}$$

which describes the decay of a free neutron into a proton, an electron and an electron antineutrino. The process is mediated by the W-boson and it is represented in Fig. 1.2.

An important quantity for decays and scattering processes is the scattering matrix element $\langle f|\hat{S}|i\rangle$, which represents the transition of an initial state $|i\rangle$ to a final state $\langle f|$ and $\hat{S}$ is the scattering operator or S-matrix. In particular, $|\langle f|\hat{S}|i\rangle|^2$ represents the probability that an initial state $|i\rangle$ transforms into a final state $\langle f|$.

In the Standard Model, the weak interactions are described by a vector minus an axial current, and in the case of the hadronic part of the β-decay, the exchange of a W-boson between a u-quark and a d-quark is represented by the hadronic current

$$\mathcal{J}^h_\mu = \bar{d}\gamma_\mu(\mathbb{1}-\gamma_5)u \equiv \mathcal{V}_\mu - \mathcal{A}_\mu \,, \tag{1.2}$$

with $\mathcal{V}_\mu = \bar{d}\gamma_\mu u$ and $\mathcal{A}_\mu = \bar{d}\gamma_\mu\gamma_5 u$ being the vector and the axial current, respectively, which are made of Dirac spinors $\bar{e}, \nu_e, \bar{d}, u$ and the CKM matrix element V_{ud} [53, 101]. The symbols γ_μ and γ_5 are Dirac matrices, and a possible matrix representation is discussed in App. A.

It is straightforward to show that the scattering matrix element is proportional to the squared modulus of the nucleon weak matrix elements, that is

$$|\langle f|\hat{S}|i\rangle|^2 \propto \left|\langle p|\mathcal{J}^h_\mu|n\rangle\right|^2 \,, \tag{1.3}$$

which, according to the decomposition in eq. (1.2), can be rewritten in terms of a nucleon vector and axial matrix element, respectively $\langle p|\mathcal{V}_\mu|n\rangle$ and $\langle p|\mathcal{A}_\mu|n\rangle$. [1]

Suppose that the initial neutron has a momentum p, and the final proton has momentum p', so that the momentum carried by the current is $q = p' - p$, then the nucleon matrix elements can be decomposed in terms of the so-called nucleon form factors $G(q^2)$, Dirac matrices γ_μ, γ_5, proton and neutron spinors $\bar{u}_p(p')$, $u_n(p)$. This is called Lorentz decomposition and for the axial current, the Lorentz decomposition reads

$$\langle p|\mathcal{A}_\mu|n\rangle = \bar{u}_p(p')\left[\gamma_\mu\gamma_5 G_A(Q^2) + \frac{q_\mu}{2m_N}\gamma_5 G_{\tilde{P}}(Q^2)\right]u_n(p)\,, \tag{1.4}$$

where $Q^2 = -q^2$, $G_A(Q^2)$ is the nucleon axial form factor, and $G_{\tilde{P}}(Q^2)$ is the nucleon induced-pseudoscalar form factor. As regards the nucleon vector matrix element, its Lorentz decomposition reads

$$\langle p|\mathcal{V}_\mu|n\rangle = \bar{u}_p(p')\left[\gamma_\mu F_1(Q^2) + \frac{i\sigma_{\mu\nu}q^\nu}{2m_N}F_2(Q^2)\right]u_n(p)\,. \tag{1.5}$$

In the experiments of neutron β-decay, the momentum transferred is very small and it can be considered negligible with respect to the nucleon mass m_N, so that only the term proportional to $G_A(Q^2 = 0)$ will contribute to eq. (1.4). In this limit, the axial form factor is called axial charge ($g_A \equiv G_A(Q^2 = 0)$) and it is accurately measured experimentally using polarized ultracold neutrons by the UCNA collaboration ([121, 49]),

$$g_A = 1.2772 \pm 0.0020\,. \tag{1.6}$$

Other experiments like PERKEO II [127] report $\lambda = g_A/g_V = 1.2767(16)$. Note that what is computed experimentally is the ratio $\lambda = g_A/g_V$ and in the SM, $g_V = 1$ up to second order corrections in isospin breaking [6, 68] due to the conservation of the vector current.

Neutrinos are very interesting particles, and there is still a lot to understand about their nature. A property of neutrinos that needs to be investigated is whether they are equivalent to their antiparticle. In this case, they would be referred to as Majorana particles. The KATRIN experiment aims to work at very high precision and to observe a very rare process that would happen if the neutrinos were Majorana particles: the neutrinoless double beta decay, introduced in [79]. Most importantly, the experiment aims to determine the electron neutrino mass m_{ν_e} through the tritium β-decay. The most updated value is an upper limit of $m_{\nu_e} < 0.8$ eV with 90% CL, see [15, 14].

1.3 Elastic and Quasielastic neutrino-nucleon scattering

The Elastic and Quasielastic neutrino-nucleon scattering are processes that involve a neutrino interacting with a nucleon target through a Z-boson or $W^\pm$-bosons, and the Feynman diagrams

---

[1] An attempt at a theory that describes well the beta radiation at sufficiently low energy was made in 1934 by E. Fermi, see [74].

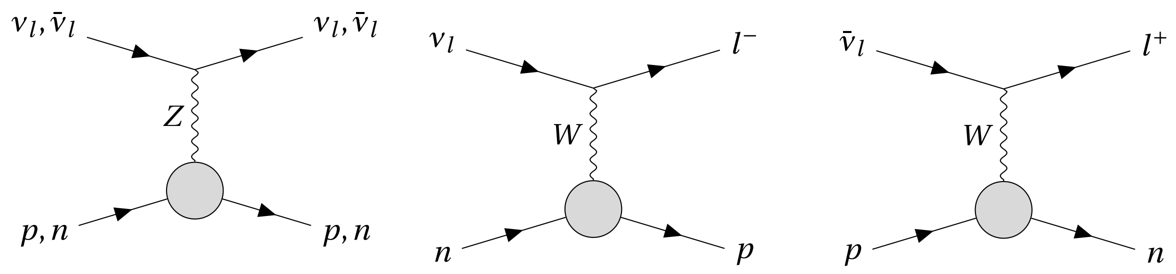

Figure 1.3:
Elastic and Quasielastic neutrino and antineutrino scattering off nucleon targets. (left) Neutral current (NC) weak interaction, mediated by a Z boson. (middle, right) Charged current weak processes, mediated by W bosons.

are represented in Fig. 1.3. Some authors refer to Quasielastic scattering when the nucleons are quasi-free in the nuclei. A comparison between the processes mediated by the W-bosons in Fig. 1.3 and Fig. 1.2 shows that a crossing symmetry relates the two and thus the scattering amplitudes are similar.

Following [75, 122, 40, 137, 25], in the case of muon (anti)neutrino-nucleon scattering, the differential cross section is

$$\frac{d\sigma^{(\nu_\mu p, \bar\nu_\mu p)}}{dQ^2} = \frac{G_F^2 m_N^2 |V_{ud}|^2}{8\pi E_\nu^2}\left[A(Q^2) \mp B(Q^2)\frac{s-u}{m_N^2} + C(Q^2)\frac{(s-u)^2}{m_N^4}\right] . \tag{1.7}$$

The plus sign in eq. (1.7) is for neutrino scattering, while the minus sign is for antineutrino scattering. The expressions for the functions $A(Q^2)$, $B(Q^2)$, and $C(Q^2)$ are

$$\begin{aligned} A = \frac{m_\mu^2 + Q^2}{m_N^2}\Big[&(1+\tau)G_A^2 - (1-\tau)(F_1^2 - \tau F_2^2) + 4\tau F_1 F_2 + \\ &- \frac{m_\mu^2}{4m_N^2}\Big((F_1+F_2)^2 + (G_A + 2G_{\tilde P})^2 - 4(1+\tau)G_{\tilde P}^2\Big)\Big] , \end{aligned} \tag{1.8}$$

$$B = 4\tau\, G_A(F_1 + F_2) , \tag{1.9}$$

$$C = \frac{1}{4}\left[G_A^2 + F_1^2 + \tau F_2^2\right] \tag{1.10}$$

and

$$s - u = 4m_N E_\nu - Q^2 - m_\mu^2 , \qquad \tau = \frac{Q^2}{4m_N^2} . \tag{1.11}$$

The Pauli and Dirac form factors F_1 and F_2 are known from electron-hadron scattering, but for the axial form factors, one often adopts the dipole parametrization

$$G_A(Q^2) = \frac{g_A}{\left(1 - \frac{Q^2}{M_A^2}\right)^2} \tag{1.12}$$

and uses the determination of the axial charge, see eq. (1.6), to extract the axial mass M_A. The parametrization in eq. (1.12) corresponds to an exponential spatial distribution for the axial charge within the nucleon, and there is no proof that this assumption is correct.

These processes are essential as they enter in the neutrino oscillations experiments, a phenomenon that is introduced in the next section.

1.4 Neutrino oscillations

The neutrino oscillations are quantum mechanical phenomena whose possibility was first noted by Pontecorvo in 1957 [132], then studied independently by Maki, Nakagawa, and Sakata in [112] and again by Pontecorvo in 1967, see [133]. In this paper, the author discussed the possibility of observing this phenomenon by tracking the neutrinos produced in the Sun. He anticipated the solar neutrino problem, according to which the number of detected solar (electron) neutrinos observed on earth is smaller than the flux predicted by the Standard Solar Model, see [24]. This puzzle is now explained by the fact that the electron neutrinos produced in the solar p-p chains transform to muon or tau neutrinos while travelling toward earth, which can occur if they are not massless. Since neutrinos are massless in the Standard Model, this phenomenon is beyond the Standard Model (BSM).

The flavor eigenstates of neutrinos $|\nu_\alpha\rangle$ are different from the mass eigenstates $|\nu_i\rangle$, but the two are related by a unitary matrix U, called Pontecorvo-Maki-Nakagawa-Sakata (PMNS) matrix that is

$$|\nu_\alpha\rangle = \sum_i U^*_{\alpha i} |\nu_i\rangle \ . \tag{1.13}$$

A possible parametrization for the PMNS matrix is given by introducing mixing angles θ_{ij} between different neutrinos and three phases δ, α_1 and α_2, such that it reads

$$\begin{aligned} U &= \begin{bmatrix} U_{e1} & U_{e2} & U_{e3} \\ U_{\mu 1} & U_{\mu 2} & U_{\mu 3} \\ U_{\tau 1} & U_{\tau 2} & U_{\tau 3} \end{bmatrix} \\ &= \begin{bmatrix} 1 & 0 & 0 \\ 0 & c_{23} & s_{23} \\ 0 & -s_{23} & c_{23} \end{bmatrix} \begin{bmatrix} c_{13} & 0 & s_{13}e^{-i\delta} \\ 0 & 1 & 0 \\ -s_{13}e^{i\delta} & 0 & c_{13} \end{bmatrix} \begin{bmatrix} c_{12} & s_{12} & 0 \\ -s_{12} & c_{12} & 0 \\ 0 & 0 & 1 \end{bmatrix} \begin{bmatrix} e^{i\alpha_1/2} & 0 & 0 \\ 0 & e^{i\alpha_2/2} & 0 \\ 0 & 0 & 1 \end{bmatrix} , \end{aligned} \tag{1.14}$$

where for shortening the notation $c_{ij} = \cos\theta_{ij}$, $s_{ij} = \sin\theta_{ij}$. The phase factors α_1 and α_2 are non-zero if neutrinos are Majorana particles, i.e. if the neutrino is identical to its antineutrino and they do not enter into oscillation processes, thus they cannot be determined from neutrino oscillations experiments. The other phase factor δ is relevant for the CP symmetry: a non-zero value would mean that neutrinos oscillate differently than antineutrinos, see [3] and below. The mass eigenstates $|\nu_i\rangle$ can be described, for example, by plane waves, so that

$$|\nu_i(t)\rangle = e^{-i(E_i t - \mathbf{p}_i\cdot\mathbf{x})}\,|\nu_i(0)\rangle \tag{1.15}$$

and in the ultrarelativistic limit ($p_i \equiv |\mathbf{p}_i| \gg m_i$), the probability that a neutrino with flavor α transforms to a neutrino with flavor β after travelling a length L is

$$\begin{aligned} P(\nu_\alpha \to \nu_\beta) = \left|\langle \nu_\beta(L)|\nu_\alpha\rangle\right|^2 = \delta_{\alpha\beta} &- 4\sum_{i>j} \mathrm{Re}\left(U^*_{\alpha i}U_{\beta i}U_{\alpha j}U^*_{\beta j}\right)\sin^2\left(\frac{\Delta m^2_{ij}L}{4E}\right) \\ &+ 2\sum_{i>j} \mathrm{Im}\left(U^*_{\alpha i}U_{\beta i}U_{\alpha j}U^*_{\beta j}\right)\sin\left(\frac{\Delta m^2_{ij}L}{2E}\right), \end{aligned} \tag{1.16}$$

where $\Delta m^2_{ij} \equiv m_i^2 - m_j^2$ is the difference of the squared masses. It is clear that for massless neutrinos, the probability in eq. (1.16) would be zero, and no oscillation would occur. However, this phenomenon has been observed several times and proves that neutrinos have a non-vanishing, though tiny, mass. The neutrino oscillations are also sensitive to the phase factor δ, which enters in the second sum in eq. (1.16), and it is relevant for the CP asymmetry

$$A^{(\alpha\beta)}_{\mathrm{CP}} = P(\nu_\alpha \to \nu_\beta) - P(\bar{\nu}_\alpha \to \bar{\nu}_\beta) = 4\sum_{i>j} \mathrm{Im}\left(U^*_{\alpha i}U_{\beta i}U_{\alpha j}U^*_{\beta j}\right)\sin\left(\frac{\Delta m^2_{ij}L}{2E}\right). \tag{1.17}$$

There exist quite a few neutrino oscillation experiments that aim to improve the accuracy of the results. Notice that in eq. (1.16) the neutrino oscillations are sensitive to Δm^2_{ij}; therefore, it is not possible to determine the individual masses of the mass eigenstates neutrinos through these experiments. This leads to the uncertainty for the mass hierarchy of flavor eigenstates neutrinos since they are related by eq. (1.13).

Improving the precision in the determination of the PMNS entries $U_{\alpha i}$ could say if neutrinos oscillate differently than antineutrinos, giving rise to CP violation.

In these experiments, further complications arise as the target is not made of free nucleons. Some nuclear models are required to connect neutrino-nuclei scattering with neutrino-nucleon scattering of eq. (1.7).

Some of the neutrino oscillation experiments are SNO [37] in Canada and T2K [2] in Japan, which were awarded the Nobel prize in physics in 2015 for the discovery that neutrinos oscillate. Other ongoing and planned neutrino oscillation experiments are, for example, DUNE, MINERvA, NOvA, and MiniBooNE at Fermilab [4, 13, 5, 8], OPERA at CERN and LNGS [7], Hyper-Kamiokande [95], and many others.

For example, in the MiniBooNE experiment at Fermilab, see [9, 8, 10, 11, 12], a muon neutrino beam is directed at a detector filled with 800 tons of mineral oil. An excess of electron neutrino events has been found in these experiments and it supports the neutrino oscillation phenomenon. In this experiment, the NUANCE v3 event generator [61] is employed to estimate neutrino interaction rates in the alkenes target medium. The NUANCE generator takes into account all the possible interaction processes in the neutrino energy region relevant for MiniBooNE, that is $0 < E_\nu < 3$ GeV. For this reconstruction, they find that processes including pion production in the final state must be taken into account.

In particular, the largest background is from single-pion production ($CC1\pi$, $NC1\pi$), and the final state can be a $\Delta(1232)$ resonance, a radial excitation of the nucleon like the Roper resonance $N^*(1440)$, or a two-particle state $N\pi$, which are all detected as $N\pi$ states with different transition amplitudes. For this reason, not only single-nucleon matrix elements of the form $\langle N|\mathscr{J}|N\rangle$ are needed, but also $\langle N\pi|\mathscr{J}|N\rangle$, $\langle N^*|\mathscr{J}|N\rangle$ and $\left\langle \Delta^+\middle|\mathscr{J}\middle|N\right\rangle$, see [103] for a detailed discussion.

1.5 Motivation and goal

Several world-leading experiments are addressing questions related to neutrino physics that need to be answered. The mixing angles of the PMNS matrix and the CP-violating phase δ can be calculated through oscillation experiments, while the Majorana phase α_i and the neutrino masses can be obtained from the neutrinoless double-beta decay of certain nuclei if discovered. However, very high precision is needed in the determination of the parameters that enter in the cross sections of neutrino-nucleon scattering at the detector level. Through lattice simulations, it is possible to compute such parameters and help achieve this goal. In the next chapter, I will introduce Lattice QCD, which is the discretized version of the theory of strong interactions, and I will show how it is possible to determine the nucleon matrix elements of the form $\langle N|\mathscr{J}|N\rangle$ and $\langle N\pi|\mathscr{J}|N\rangle$, that are required for neutrino oscillation experiments. These nucleon matrix elements must be computed at a non-perturbative regime, i.e., at low energy. At this scale, the perturbative calculations fail. However, it is possible to discretize the theory and compute the observables statistically, as I will explain in the next chapter.

By discretizing the theory of strong interactions, some systematics are introduced:

- discretization effects, due to a non-zero the lattice spacing a, that is the distance between two adjacent lattice sites. The limit $a \to 0$ will be taken by considering different a and it is named the "continuum limit";
- volume effects V, which should disappear when taking the "infinite volume limit" ($V \to \infty$) by computing the observables using ensembles with different (though finite) volumes;
- limited volume size because for computational reasons, it is prohibitive to generate ensembles with very large volumes as the computational times would be unfeasible;

- unphysical quark masses, which are introduced to lower the computational costs of the simulations. Using effective field theory the observables are then extrapolated to the "physical point" ($m_{\pi^0} \approx 135$ MeV).

The work presented in this thesis represents a pilot study that nobody has done before. In particular, the main goal is to extract not only nucleon form factors like $G_A(q^2)$ and $G_{\tilde{P}}(q^2)$, that enter in the weak cross sections of processes like $\nu_l \; n \to l^- \; p$ and $\bar{\nu}_l \; p \to l^+ \; n$, but also the matrix elements $\langle N\pi|\mathcal{J}|N\rangle$ that are important in the reconstruction of the neutrino energy at the detector level, see the discussion at the end of the previous section. Furthermore, it is needed to understand excited state contamination in the nucleon correlation functions, as will be discussed in more detail in Chap. 3.

In this project, the matrix elements are computed using a single ensemble, i.e., a single lattice volume, lattice spacing, and quark mass, but in the future, we plan to include more ensembles in the analysis and compute $\langle \Delta^+ \middle| \mathcal{J} |N\rangle$, so that I will extrapolate both $\langle \Delta^+ \middle| \mathcal{J} |N\rangle$ and $\langle N\pi|\mathcal{J}|N\rangle$ to the physical point.

CHAPTER

TWO

QCD: FROM THE CONTINUUM TO THE LATTICE

2.1 A brief overview of the strong force

Quantum Chromodynamics is the quantum field theory that describes the interaction between quarks, antiquarks, and gluons. The quarks are elementary particles and fermions of spin 1/2, with six different flavors and three generations, see Fig. 1.1. They carry not only electric charge but also a color charge of three different types: red, green, and blue. In their fundamental representation, they are represented by Dirac spinor fields $q_{\alpha}^{f,c}(x)$, f refers to the flavor being up, $down$, $strange$, $charm$, $bottom$, and top, while $c = r, g, b$ refers to the color indices and $\alpha = 1, 2, 3, 4$ to the Dirac indices. The antiquarks are the antiparticles of the quarks. They belong to the antifundamental representation of $SU(3)$ and carry anticolor. The gluons are massless vector bosons with spin 1 and act as mediators of the strong force, similarly to the photons in QED for the electromagnetic force and to the W and Z bosons for the weak force. The main difference is that the gluons carry two charges: one color and one anticolor.

Like QED, the QCD action will be constructed from first principles starting from the free Lagrangian of the quarks and requiring that the action is invariant under any transformations of the $SU(3)$ color group. In the free theory, since the quarks are fermions, they must obey the Dirac equation and therefore the Lagrangian density is

$$\mathscr{L}_{\text{free}}[\bar{q}, q] = \sum_{f} \bar{q}^{f}(x)\big(i\partial\!\!\!/ - m_f\big)q^{f}(x)\,, \tag{2.1}$$

where $\bar{q}^{f}(x) = q^{f}(x)^{\dagger}\gamma^{0}$, which is the adjoint quark field and $\partial\!\!\!/ \equiv \gamma^{\mu}\partial_{\mu}$, following Feynman's (slashed) notation. The Lagrangian density in eq. (2.1) is intended in Minkowski spacetime.

The corresponding free action

$$\mathrm{S}_{\text{free}}[\bar{q}, q] = \int d^{4}x\, \mathscr{L}_{\text{free}}[\bar{q}, q] \tag{2.2}$$

is not invariant under the $SU(3)$ local gauge transformation $\Omega(x)$,

$$q^f(x) \quad \longrightarrow \quad q'^f(x) = \Omega(x)\, q^f(x) \,, \tag{2.3}$$

$$\bar{q}^f(x) \quad \longrightarrow \quad \bar{q}'^f(x) = \bar{q}^f(x)\, \Omega(x)^\dagger \,, \tag{2.4}$$

unless, similarly to QED, we replace in eq. (2.1) the partial derivative with the covariant derivative ($\partial_\mu \to D_\mu$),

$$D_\mu(x) = \partial_\mu - igA_\mu(x) \,, \tag{2.5}$$

where we introduce the gluon field $A_\mu(x) = \sum_a t_a A^a_\mu(x)$, with $a = 1,...,8$. The parameter g in eq. (2.5) is the strong coupling constant and $t_a = \frac{1}{2}\lambda_a$, where λ_a are the eight generators of $SU(3)$, i.e. the Gell-Mann matrices, which satisfy

$$\left[\lambda_a, \lambda_b\right] = 2i \sum_c f^{abc} \lambda_c \,. \tag{2.6}$$

The f^{abc} are called structure constants. For the action to be gauge invariant, the gluon field must transform under $SU(3)$ accordingly

$$A_\mu(x) \quad \longrightarrow \quad A'_\mu(x) = \Omega(x) A_\mu(x) \Omega(x)^\dagger + \frac{i}{g}\left(\partial_\mu \Omega(x)\right)\Omega(x)^\dagger \,. \tag{2.7}$$

Finally, the gauge invariant QCD Lagrangian in Minkowski spacetime reads

$$\mathscr{L}_{\mathrm{QCD}}(x) = \sum_f \bar{q}^f(x)\left(i\not{D} - m_f\right) q^f(x) - \frac{1}{4} G_{a\mu\nu}(x) G^{\mu\nu}_a(x) \,, \tag{2.8}$$

and we can construct the Feynman rules and diagrams to perform perturbative calculations. The last term in the QCD Lagrangian density is the kinetic term for the field $A_\mu(x)$ and $G_{\mu\nu}(x) = t_a G^{\mu\nu}_a(x)$ is the field strength tensor, defined by

$$G_{\mu\nu}(x) \equiv \frac{i}{g}\left[D_\mu, D_\nu\right] = \partial_\mu A_\nu(x) - \partial_\nu A_\mu(x) - ig\left[A_\mu(x), A_\nu(x)\right] \,. \tag{2.9}$$

In this equation, the symbols $[,]$ refer to the commutator, and the main difference between QCD and QED is the term $\left[A_\mu(x), A_\nu(x)\right]$. In contrast to QED, where the commutator of $U(1)$ gauge fields is zero, in QCD this term does not vanish, and the group of matrices A_μ is therefore non-Abelian. This term gives new Feynman rules to consider, and contrary to QED, there are 3-gluon and 4-gluon vertices (gluon self-interactions) to take into account.

We can rewrite the QCD Lagrangian density of eq. (2.8) in terms of the free quarks, Lagrangian density $\mathscr{L}_{\mathrm{free}}[\bar{q}, q]$ of eq. (2.1), the interaction Lagrangian density $\mathscr{L}_{\mathrm{I}}[\bar{q}, q, A_\mu]$ and the gluonic Lagrangian density $\mathscr{L}_{\mathrm{G}}[A_\mu]$, where

$$\mathscr{L}_{\mathrm{I}}[\bar{q}, q, A_\mu] = -g \sum_f \bar{q}^f(x) \gamma^\mu q^f(x) A_\mu(x) \,, \tag{2.10}$$

$$\mathscr{L}_{\mathrm{G}}[A_\mu] = -\frac{1}{4} G_{a\mu\nu}(x) G^{\mu\nu}_a(x) \,. \tag{2.11}$$

For future purposes, it is helpful to define $\mathscr{L}_{\mathrm{F}}[\bar{q}, q] = \mathscr{L}_{\mathrm{free}}[\bar{q}, q, A_\mu] + \mathscr{L}_{\mathrm{I}}[\bar{q}, q, A_\mu]$, so that the QCD action takes the form

$$\mathrm{S}_{\mathrm{QCD}}[\bar{q}, q, A_\mu] = \int d^4x\, \mathscr{L}_{\mathrm{QCD}}[\bar{q}, q, A_\mu] = \mathrm{S}_{\mathrm{F}}[\bar{q}, q, A_\mu] + \mathrm{S}_{\mathrm{G}}[\bar{q}, q, A_\mu]\,, \tag{2.12}$$

with

$$\mathrm{S}_{\mathrm{F}}[\bar{q}, q, A_\mu] = \int d^4x \sum_f \bar{q}^f(x)\big(i\not{D} - m_f\big)q^f(x)\,, \tag{2.13}$$

$$\mathrm{S}_{\mathrm{G}}[\bar{q}, q, A_\mu] = -\int d^4x\, \frac{1}{2}\,\mathrm{Tr}\big\{G_{\mu\nu}(x)G^{\mu\nu}(x)\big\}\,. \tag{2.14}$$

The reader can verify that the QCD action of eq. (2.12) is invariant under $SU(3)$ gauge transformation $\Omega(x)$. I recommend the textbooks [147, 128, 113], for a more detailed introduction to QCD. Non-Abelian gauge theories like QCD exhibit asymptotic freedom, one of the most important characteristics of the strong interactions. At high energies, the quarks interact weakly, allowing perturbative calculations that can be performed using the Feynman diagrams.

At low energies, the interaction gets stronger, leading to the confinement of quarks and gluons within hadrons. This aspect of the theory is not mathematically proven because the perturbative calculations fail at low energy scales. However, there is a tool that allows physicists to make predictions at this scale: Lattice QCD.

2.2 QCD on the lattice

For some of the following sections, I follow the structure of [146], and I refer to [82]. As stated in the last part of the previous section, the perturbative calculations with Feynman diagrams fail at low energy. In this section, I discretize the theory of strong interactions and show that is possible to simulate it using (super)computers and make predictions at low energy scales.

Using the path integral formalism, it is possible to write the expectation values of multi-local gauge-invariant operators O, which depends on the fields A_μ, q and $\bar{q}$, like

$$\langle\, \mathrm{O}(\bar{q}, q, A_\mu)\,\rangle = \frac{1}{\mathcal{Z}_{QCD}} \int \mathscr{D}[\bar{q}, q]\, \mathscr{D}[A_\mu]\, \mathrm{O}(\bar{q}, q, A_\mu)\;\; e^{iS_{QCD}[\bar{q},q,A_\mu]}\,, \tag{2.15}$$

where the integral is over all the possible configurations of the fields and $\mathcal{Z}_{QCD}$ is the QCD partition function, defined by

$$\mathcal{Z}_{QCD} = \int \mathscr{D}[\bar{q}, q]\, \mathscr{D}[A_\mu]\, e^{iS_{QCD}[\bar{q},q,A_\mu]}\,. \tag{2.16}$$

Eq. (2.15) is also known as the correlation function and the symbols $\mathscr{D}[\bar{q}, q]$, $\mathscr{D}[A_\mu]$ are integral measures of the quark fields and gluon fields, respectively. To interpret the Green's function as a statistical probability, we perform the so-called Wick rotation

$$x^0 = \tau \qquad \longrightarrow \qquad -it\,, \tag{2.17}$$

which is essentially a rotation from real to imaginary time. This transformation has consequences on the representation of objects like Dirac gamma matrices, four-vectors and the action, but the main difference is that

$$iS_{QCD}[\bar{q}, q, A_\mu] \qquad \longrightarrow \qquad -S_E[\bar{q}, q, A_\mu]\,, \tag{2.18}$$

where the label "E" stands for Euclidean. The reason is that after the transformation in eq. (2.17), the metric has the Euclidean signature. [1] Thus, with the transformation of eq. (2.17), the four-vectors change as follows

$$x^\mu_{\mathbf{M}} = (x^0_{\mathbf{M}}, \mathbf{x_M}) \qquad \longrightarrow \qquad x^\mu_E = (\mathbf{x}_E, x^4_E) = (\mathbf{x_M}, i x^0_{\mathbf{M}})\,. \tag{2.19}$$

Notice that in the Euclidean metric, the temporal component is in the fourth direction and I will not distinguish between covariant and contravariant expressions when the objects are in the Euclidean metric. The main point is that after this transformation, the correlation function of eq. (2.15) becomes

$$\langle\, \mathrm{O}(\bar{q}, q, A_\mu)\,\rangle = \frac{1}{\mathcal{Z}_E} \int \mathcal{D}[\bar{q}, q]\mathcal{D}[A_\mu]\; \mathrm{O}[\bar{q}, q, A_\mu]\; e^{-S_E[\bar{q},q,A_\mu]}\,, \tag{2.20}$$

where the Euclidean partition function reads

$$\mathcal{Z}_E = \int \mathcal{D}[\bar{q}, q]\mathcal{D}[A_\mu]\; e^{-S_E[\bar{q},q,A_\mu]}\,. \tag{2.21}$$

In Euclidean spacetime, the correlation function in eq. (2.20) has an expression that is suitable to simulate through importance sampling, that is explained in the next sections. We then transform the infinite physical volume into a finite $3D$ hypercubic volume. The total size is $V = L^3 \times T$, where L and T are the spatial and temporal lattice extent, respectively. The spatial extent L is divided into N_s lattice sites equally spaced by the lattice spacing a, so that $L = aN_s$, while the temporal extent is made up of N_t lattice sites, again equally spaced by the same amount a, so that $T = aN_t$. The set of all lattice sites is

$$\Lambda = \left\{ n \mid n_1, n_2, n_3 \in \{0, 1, ..., N_s - 1\}, n_4 \in \{0, 1, ... N_t - 1\} \right\} \tag{2.22}$$

and the continuum spacetime coordinates x, that in eq. (2.15) were interpreted in Minkowski spacetime, are replaced by discrete lattice coordinates

$$x^\mu_E = \left\{ an^\mu \mid n^1, n^2, n^3 \in \{0, 1, ..., N_s - 1\},\; n^4 \in \{0, 1, ... N_t - 1\} \right\}. \tag{2.23}$$

---

[1] For more details on the convention that I use herein and the two metrics, I refer to the App. A.

The four-momentum carried out by the particle reads $p_E^\mu = (\mathbf{p}_E, p_E^4)$, which is also discretized such that

$$\mathbf{p}_E = \frac{2\pi}{L}\,\mathbf{n}\,, \qquad \mathbf{n} = (n_1, n_2, n_3)\,, \qquad \text{with } n_i = -\frac{N_s}{2} + 1, ..., \frac{N_s}{2}\,, \tag{2.24}$$

and the maximum momentum in each direction is $\max\{p_i\} = \pi a^{-1}$, while the minimum non-zero momentum is $\min\{p_i\} = \pi L^{-1}$. Therefore the lattice spacing a works as a momentum cut-off (ultraviolet regulator), while L works as an infrared regulator. Normally, the volume is chosen to be as large as possible to make volume effects as small as possible, but the larger the volume gets, the less feasible the computations of lattice objects, above all the propagators, see Sec. (2.7). Therefore, the observables are computed on different finite volumes V and lattice spacings a and then one carefully extrapolates the data to the physical limit ($V \to \infty$, $a \to 0$). Once we have discretized the spacetime, we proceed with discretizing the QCD action of eq. (2.12). There are different ways to discretize the action and in this work we adopt the Wilson-Clover discretization, which will be discussed in the following sections.

2.3 Fermionic action: from naive to the improved version

In the following, I will consider only Euclidean objects, and for more clarity, I will drop the subscript "E". Still, they should not be confused with the respective objects in Minkowski spacetime. In the continuum theory and Minkowski spacetime, the action for the free quark fields is written in eq. (2.2). The Euclidean and naive discretized version is

$$\mathrm{S}^{\text{naive}}_{\text{free}}[\bar{q}, q] = a^4 \sum_{n\in\Lambda} \sum_f \Big(\bar{q}^f(n) \sum_\mu \gamma_\mu \frac{q^f(n+\hat{\mu}) - q^f(n-\hat{\mu})}{2a} \Big) + m_f \bar{q}^f(n) q^f(n)\,, \tag{2.25}$$

where the integral is replaced with a finite sum over all lattice sites, the quark fields are located at the lattice coordinates $x_n = an$, but we omit the lattice spacing in brackets for shorthand notation, and the continuum derivative is replaced by the symmetric discretized expression. From now on, I will work with lattice units, and the physical units can be retrieved with dimensional analysis. Analogously to the continuum theory, this action lacks $SU(3)$ gauge invariance. Likewise, we require that on the lattice, the action preserves $SU(3)$ gauge invariance, and we introduce the gauge links $U_\mu(n)$,

$$U_\mu(n) = \exp\Big\{ igA_\mu(n) \Big\} = \mathbb{1} + igA_\mu(n) + \mathcal{O}(a^2)\,, \tag{2.26}$$

which are elements of $SU(3)$ that connect the point n with the adjacent point $n + \hat{\mu}$ (see Fig. 2.1) and that transform under a discretized $SU(3)$ gauge transformation $\Omega(n)$ according to

$$U_\mu(n) \qquad \longrightarrow \qquad U'_\mu(n) = \Omega(n)\; U_\mu(n)\; \Omega(n+\hat{\mu})^\dagger\,. \tag{2.27}$$

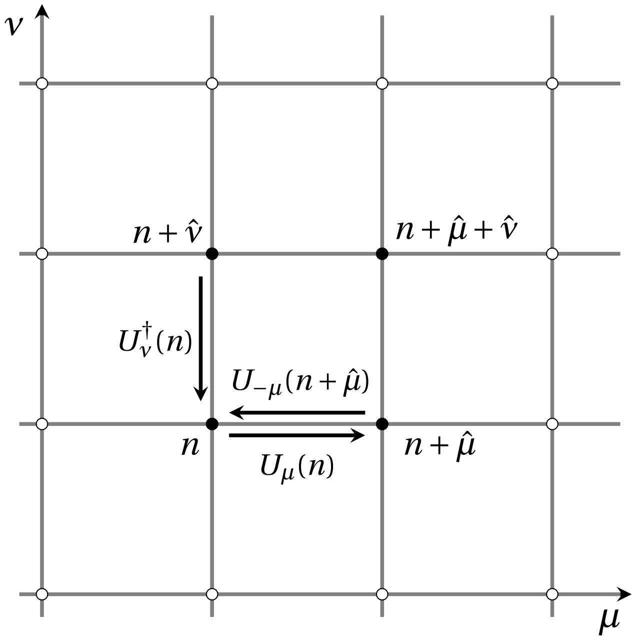

Figure 2.1:
This is a 2D representation of a section of a lattice face. The quarks are located on the lattice sites and the gauge fields are represented by the links that connect the adjacent lattice sites.

With this definition of the gauge links, we define the discretized derivative operators

$$\nabla_\mu q^f(n) = \left[U_\mu(n) q^f(n+\hat{\mu}) - q^f(n)\right], \tag{2.28}$$

$$\nabla^*_\mu q^f(n) = \left[q^f(n) - U_{-\mu}(n) q^f(n-\hat{\mu})\right], \tag{2.29}$$

where for convenience, we define $U_{-\mu}(n) \equiv U_\mu(n-\hat{\mu})^\dagger$ and the naive gauge invariant fermionic action takes the expression

$$\mathrm{S}_\mathrm{F}^\mathrm{naive}[\bar{q}, q, U] = \sum_{n\in\Lambda} \sum_f \left[m_f \bar{q}^f(n) q^f(n) + \bar{q}^f(n) \sum_{\mu=1}^{4} \gamma_\mu \frac{\nabla_\mu + \nabla^*_\mu}{2} q^f(n)\right]. \tag{2.30}$$

It is easy to see, by expanding in powers of a, that the eq. (2.30) gives the correct continuum limit up to $\mathcal{O}(a)$. Unfortunately, this naive discretization has problems when we calculate the quark propagator in momentum space.[2] The problem is that, for finite lattice spacing, in momentum space the propagator has 16 poles instead of a single one at $p_\mu = 0$. The other 15 poles are unphysical and they are called doublers.

---

[2] The details of its derivation are written, for example, in Chap. 9 of [147] and Chap. 5 of [82]

There are many solutions being proposed for this problem. In 1977 [144], Wilson suggested adding to the naive action the quadratic term

$$-\frac{1}{2}\sum_{n\in\Lambda}\sum_{f}\sum_{\mu=1}^{4}\bar{q}^{f}(n)\left(\nabla_{\mu}-\nabla_{\mu}^{*}\right)q^{f}(n)\,, \tag{2.31}$$

which in the continuum has the expression

$$\int d^4x\sum_{f}\bar{q}^{f}(x)\partial^{\mu}\partial_{\mu}q(x) \tag{2.32}$$

and that vanishes when $a\to 0$. The advantage of this new term is that, while it does not contribute to the physical pole, the (unwanted) doublers decouple from the theory in the continuum limit. For more details you can read Sec. 5.2.2 of [82]. To compactify the notation, we define the hopping parameter

$$\kappa_f=\frac{1}{2(m_f+4)}\,, \tag{2.33}$$

which has a critical value at $\kappa_c = 1/8$, where chiral symmetry is restored, but it gets shifted by quantum effects. The renormalized mass can be calculated from the fermion self-energy as in [131]. Adding the Wilson term in eq. (2.31) to the naive action in eq. (2.30) we obtain the Wilson fermion action

$$\mathrm{S}_{\mathrm{F}}^{\mathrm{Wilson}}[\bar{q},q,U]=\sum_{f}\left(m_f+4\right)\sum_{n\in\Lambda}\bar{q}^{f}(n)\left(q^{f}(n)-\kappa_f\sum_{\mu=\pm1}^{\pm4}(1-\gamma_{\mu})U_{\mu}(n)q^{f}(n+\hat{\mu})\right). \tag{2.34}$$

This action is gauge invariant, does not suffer from the doubling fermions and approaches the continuum action up to $\mathcal{O}(a)$ discretization errors. In the literature, it is rewritten like

$$\mathrm{S}_{\mathrm{F}}^{\mathrm{Wilson}}[\bar{q},q,U]=\sum_{f}\sum_{n\in\Lambda}\bar{q}^{f}(n)D^{W}(n,m)q(m)\,, \tag{2.35}$$

where $D^W(n,m)$ is the Wilson Dirac operator that reads

$$D^{W}(n,m)=C\left(\mathbb{1}-\kappa_f H(n,m)\right) \tag{2.36}$$

and the various terms that are introduced are

$$C=m_f+4\,, \tag{2.37}$$

$$H(n,m)=\sum_{\mu=\pm1}^{\pm4}(1-\gamma_{\mu})\;U_{\mu}(n)\;\delta_{n+\hat{\mu},m}\,. \tag{2.38}$$

The constant C is irrelevant and it can be absorbed in a redefinition of the quark fields $q\to\sqrt{C}q$, $\bar{q}\to\sqrt{C}\bar{q}$. The matrix H contains all the nearest neighbour terms in the Wilson operator and thus is usually referred to as the hopping matrix.

2.4 Wilson gauge action

It is left to add the discretized version of the pure gauge theory term, defined in eq. (2.14). By using the gauge transformation for the gauge links in eq. (2.27), one can see that the closed loop that we represent in Fig. 2.2 and that has the expression

$$P_{\mu\nu}(n) = U_\mu(n)U_\nu(n+\hat{\mu})U_\mu(n+\hat{\nu})^\dagger U_\nu(n)^\dagger \tag{2.39}$$

is clearly a gauge invariant quantity. This product of gauge links is called plaquette.

By using the definition in eq. (2.26) and by expanding in powers of a, the term

$$\mathrm{S}_{\mathrm{G}}^{\mathrm{Wilson}}[U] = -\frac{\beta}{3}\sum_{n\in\Lambda}\sum_{\mu<\nu}\Big(1 - P_{\mu\nu}(n)\Big) \tag{2.40}$$

gives the correct continuum limit of the pure gauge action up to $\mathcal{O}(a^2)$, where we also use the Baker-Campbell-Hausdorff formula

$$e^A e^B = e^{A+B+\frac{1}{2}[A,B]+\dots} \,. \tag{2.41}$$

In eq. (2.40), we introduce the parameter

$$\beta = \frac{6}{g^2}\,, \tag{2.42}$$

which characterizes the gauge action and fixes the scale. In conclusion, combining the pure gauge action of eq. (2.40) with the fermionic action in eq. (2.34), the full lattice QCD action reads

$$\mathrm{S}_{\mathrm{QCD}}^{\mathrm{Wilson}}[\bar{q},q,U] = \mathrm{S}_{\mathrm{F}}^{\mathrm{Wilson}}[\bar{q},q] + \mathrm{S}_{\mathrm{G}}^{\mathrm{Wilson}}[U]\,. \tag{2.43}$$

2.5 Symanzik improvement

The Wilson fermionic action in eq. (2.34) approaches the continuum limit up to $\mathcal{O}(a)$ lattice artefacts, while $\mathrm{S}_{\mathrm{G}}^{\mathrm{Wilson}}[U]$ in eq. (2.40) up to $\mathcal{O}(a^2)$ discretization errors. It is possible to add more terms in the fermionic Wilson action to achieve an approach towards the continuum limit up to $\mathcal{O}(a^2)$. This procedure is called Symanzik improvement.

2.5.1 Wilson-Clover action

Following Chap. 9 of [82], the only term that can be added to the Wilson fermionic action and that is not redundant due to the Dirac equation is proportional to

$$\sum_f\sum_{n\in\Lambda}\bar{q}^f(n)\sigma_{\mu\nu}G_{\mu\nu}q^f(n)\,. \tag{2.44}$$

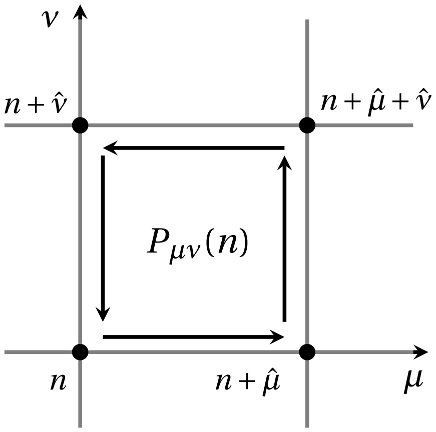

Figure 2.2:
What is represented here is the simplest closed loop that the gauge links may form, which is called plaquette.

Notice that we do not distinguish the covariant and the contravariant symbols as the metric tensor is Euclidean. In [134], the authors Sheikholeslami and Wohlert propose that the improved fermionic action

$$\mathrm{S}_{\mathrm{F}}^{\mathrm{SW}}[\bar{q},q] = \mathrm{S}_{\mathrm{F}}^{\mathrm{Wilson}}[\bar{q},q] + c_{\mathrm{SW}} \sum_{f} \sum_{n\in\Lambda} \bar{q}^{f}(n)\sigma_{\mu\nu}G_{\mu\nu}q(n) \ , \tag{2.45}$$

where

$$G_{\mu\nu} = \frac{-i}{8}\Big(Q_{\mu\nu}(n) - Q_{\nu\mu}(n)\Big) \tag{2.46}$$

is the lattice field strength tensor, a discretized version of eq. (2.9) and

$$Q_{\nu\mu}(n) = P_{\mu\nu}(n) + P_{\mu-\nu}(n) + P_{-\mu-\nu}(n) + P_{-\mu\nu}(n) \tag{2.47}$$

is the sum of all the adjacent plaquettes. This sum has the shape of a clover and therefore the Sheikholeslami-Wohlert action of eq. (2.45) is generally known as clover action $\mathrm{S}_{\mathrm{F}}^{\mathrm{clover}}$. In order to achieve full $\mathcal{O}(a)$-improvement, the local operators $\mathcal{J}$ appearing for instance in matrix elements $\langle N' | \mathcal{J} | N \rangle$ must also be Symanzik-improved. The $\mathcal{O}(a)$-improved axial current is

$$\mathscr{A}_{\mu}^{(\mathrm{imp})}(x) = \mathscr{A}_{\mu}(x) + c_A \partial_{\mu}\mathscr{P}(x) \ , \tag{2.48}$$

while the pseudoscalar current is already $\mathcal{O}(a)$-improved, i.e.

$$\mathscr{P}^{(\mathrm{imp})}(x) = \mathscr{P}(x) \ . \tag{2.49}$$

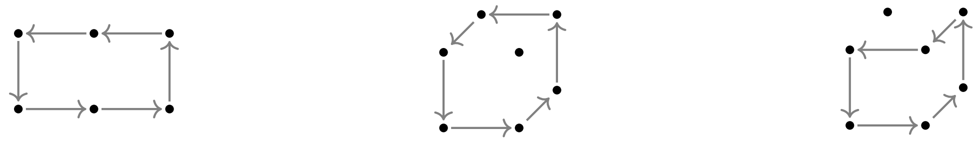

$\mathscr{P}_1^{(6)}$ $\mathscr{P}_2^{(6)}$ $\mathscr{P}_3^{(6)}$

Figure 2.3: These are some possible closed gauge loops of dimension six.

2.5.2 Lüscher-Weisz improved gauge action

Although the Wilson gauge action is already $\mathscr{O}(a)$-improved, it is possible to improve it even further. In [109], Lüscher and Weisz propose the tree-level Symanzik-improved gauge action

$$\mathrm{S}_{\mathrm{G}}^{\mathrm{LW}}[U] = c_1^{(4)} \mathrm{S}_{\mathrm{G}}^{\mathrm{Wilson}}[U] + \frac{\beta}{3} \sum_{i=1}^{3} c_i^{(6)} \sum_{\mathbb{C} \in \mathscr{P}_i^{(6)}} Re\,\mathrm{Tr}\{\mathbb{1} - U(\mathbb{C})\} , \tag{2.50}$$

where $c_k^{(n)}$ are coefficients that can be computed perturbatively or non-perturbatively, $\mathscr{P}_i^{(6)}$ is the set of all elementary loops of type i and dimension six, represented in Fig. 2.3, and $U(\mathbb{C})$ is the oriented product of link variables along a path $\mathbb{C}$. In the same paper, it is stated that a single free parameter x such that $|x| < 1/16$ is sufficient to ensure the positivity of the action. In particular, the coefficients are

$$c_1^{(4)} = \frac{5}{3} - 24x , \qquad c_1^{(6)} = -\frac{1}{12} + x , \qquad c_2^{(6)} = 0 , \qquad c_3^{(6)} = x . \tag{2.51}$$

Within the CLS effort, whose definition is explained at the end of the next section, the choice is simply $x = 0$, so that

$$\mathrm{S}_{\mathrm{G}}^{\mathrm{CLS}}[U] = \frac{5}{3}\, \mathrm{S}_{\mathrm{G}}^{\mathrm{Wilson}}[U] - \frac{\beta}{36} \sum_{\mathbb{C} \in \mathscr{P}_1^{(6)}} Re\,\mathrm{Tr}\{\mathbb{1} - U(\mathbb{C})\} . \tag{2.52}$$

2.6 The Wick theorem

Finally, having constructed the Euclidean version of the QCD action, we can compute numerically the integral in eq. (2.20), whose Euclidean version is

$$\langle\, \mathrm{O}(\bar{q}, q, U)\, \rangle = \frac{1}{\mathcal{Z}} \int \mathscr{D}[\bar{q}, q] \mathscr{D}[U]\; \mathrm{O}(\bar{q}, q, U)\; e^{-\mathrm{S}[\bar{q}, q, U]} , \tag{2.53}$$

where we have replaced S_E with its discretized and $\mathscr{O}(a)$-improved version S, which reads

$$\mathrm{S}[\bar{q}, q, U] = \mathrm{S}_{\mathrm{F}}^{\mathrm{SW}}[\bar{q}, q, U] + \mathrm{S}_{\mathrm{G}}^{\mathrm{CLS}}[U] . \tag{2.54}$$

Let me recall that the clover action is defined in eq. (2.45) and the pure gauge action in eq. (2.52). The integral over quark variables could be transformed in a more feasible way for simulations because the quark fields obey the anticommutation relations

$$\{q^{f_1}(n),\ q^{f_2}(n')\} = 0\,, \qquad\qquad \{\bar{q}^{f_1}(n),\ \bar{q}^{f_2}(n')\} = 0\,. \tag{2.55}$$

Let us consider the fermionic integral which appears in eq. (2.53) and that is

$$\langle\, \mathrm{O}(\bar{q}, q, U)\,\rangle = \frac{1}{\mathcal{Z}_F}\int \mathcal{D}[\bar{q}, q]\ \mathrm{O}(\bar{q}, q, U)\ e^{-S_F[\bar{q},q,U]}\,, \tag{2.56}$$

where the fermionic partition function is

$$\mathcal{Z}_F = \int \mathcal{D}[\bar{q}, q]\ e^{-S_F[\bar{q},q,U_\mu]} \tag{2.57}$$

and S_F could be any fermionic action we discussed. In particular, S_F can be rewritten in terms of the Dirac operators $\mathcal{D}_f$ for each flavor f like

$$S_F[\bar{q}, q, U] = \sum_f \sum_{n,m\in\Lambda} \bar{q}^{f,a}_{\alpha}(n) \mathcal{D}_f(n,m)^{ab}_{\alpha\beta}\ q^{f,b}_{\beta}(m)\,, \tag{2.58}$$

and we have explicitly written the color and spin indices. For example, the Dirac operator that gives the naive fermionic action of eq. (2.30) is thus given by

$$\mathcal{D}_f(n,m)^{ab}_{\alpha\beta} = m_f \delta_{\alpha\beta}\delta_{ab}\delta_{n,m} + \sum_{\mu=1}^{4} \gamma^{\mu}_{\alpha\beta}\left(U^{ab}_{\mu}(n)\delta_{n+\hat{\mu},m} + U^{ab}_{-\mu}(n)\delta_{n-\hat{\mu},m}\right)\,. \tag{2.59}$$

Notice that this Dirac operator satisfies the γ^5-hermiticity property that is

$$\gamma^5 \mathcal{D}_f \gamma^5 = \mathcal{D}_f^{\dagger}\,. \tag{2.60}$$

The quark fields in eq. (2.57) may be integrated out for each flavor using the so-called *Matthews-Salam formula*, see [115, 116], so that

$$\int d\bar{q}^f\, dq^f\ e^{-\bar{q}^f \mathcal{D}_f q^f} \propto \det[\mathcal{D}_f] \tag{2.61}$$

and the fermionic partition function results in a product of fermionic determinants

$$\mathcal{Z}_F = \prod_f \det\bigl(\mathcal{D}_f\bigr)\,. \tag{2.62}$$

Another key formula for calculating fermionic expectation values $\langle \ldots \rangle_F$ is given by the Wick theorem. Suppose that the multi-local operator O is a product of local quark fields, i.e. O =

$q^{i_1}\bar{q}^{j_1}\cdots q^{i_n}\bar{q}^{j_n}$, where the symbols i_1 and j_1 are multi-indices that embed all the quantum numbers of the fermionic fields (color, spin, flavor, lattice site).

The Wick theorem states that the fermionic expectation value $\langle \mathrm{O}\rangle_F$ is then given by

$$\begin{aligned}\langle q^{i_1}\bar{q}^{j_1}\cdots q^{i_n}\bar{q}^{j_n}\rangle_F &= \frac{1}{Z_F}\int\prod_{k=1}^{N} dq_k d\bar{q}_k \left(q_{i_1}\bar{q}_{j_1}\cdots q_{i_n}\bar{q}_{j_n}\right)\exp\Big(-\sum_{l,m=1}^{N}\bar{q}_l\mathscr{D}_{lm}q_m\Big)\\ &= (-1)^n\sum_{P(1,\ldots,n)}\mathrm{sign}(P)(\mathscr{D}^{-1})_{i_1 j_{P_1}}\cdots(\mathscr{D}^{-1})_{i_n j_{P_n}}\,,\end{aligned}\tag{2.63}$$

where the sum is over all the permutations $P(1,...,n)$ of the numbers $1,...,n$ and $\mathrm{sign}(P)$ is the sign of the permutation P. The objects $\mathscr{D}^{-1}$ that appear are the inverse Dirac operators, i.e. Dirac propagators. Finally, after integrating out the fermionic part, the integral in eq. (2.53) becomes

$$\langle\, \mathrm{O}(\bar{q},q,U)\,\rangle = \frac{1}{\mathcal{Z}}\int\mathscr{D}[U]\;\; e^{-\mathscr{S}_G[U_\mu]}\,\prod_f \det\!\big(a^4\mathscr{D}_f\big)\,\langle\, \mathrm{O}(\bar{q},q,U)\,\rangle_W\,,\tag{2.64}$$

where $\langle\, \mathrm{O}(\bar{q},q,U)\,\rangle_W$ corresponds to the Wick contractions that give rise to the fermion propagators in eq. (2.63) and it depends on the structure of the operators O.

To give a few practical applications of eq. (2.63), and of the Wick contractions, consider the bilinear interpolating operators

$$\mathrm{O}_d(x)^{ab}_{\alpha\beta} = \bar{d}^a_\alpha(x)d^b_\beta(x)\,,\qquad\qquad \bar{\mathrm{O}}_d(y)^{ce}_{\gamma\epsilon} = \bar{d}^c_\gamma(y)d^e_\epsilon(y)\,.\tag{2.65}$$

The multi-index i_1 in eq. (2.63) is replaced with (d,a,α,x), where d is the quark flavor, a and α are the color and spin indices, respectively, and x is the spacetime coordinate. The Wick contractions that are needed for the fermionic expectation value are

$$\langle \mathrm{O}_d(x)^{ab}_{\alpha\beta}\rangle_W = \langle \bar{d}^a_\alpha(x)d^b_\beta(x)\rangle_W = -\mathscr{D}_d^{-1}(x,x)^{ba}_{\beta\alpha}\,,\tag{2.66}$$

$$\langle \mathrm{O}_d(x)^{ab}_{\alpha\beta}\,\bar{\mathrm{O}}_d(y)^{ce}_{\gamma\epsilon}\rangle_W = \mathscr{D}_d^{-1}(x,x)^{ba}_{\beta\alpha}\,\mathscr{D}_d^{-1}(y,y)^{ec}_{\epsilon\gamma} - \mathscr{D}_d^{-1}(x,y)^{bc}_{\beta\gamma}\,\mathscr{D}_d^{-1}(y,x)^{ea}_{\epsilon\alpha}\,.\tag{2.67}$$

Notice that there is only one permutation for the Wick contractions in eq. (2.66) and two permutations for those in eq. (2.67) because there are two pairs of d quarks in the latter. The relative minus sign between the two terms in the last equation is due to $\mathrm{sign}(P)$ in eq. (2.63), which comes from the anticommutation rules of the fermionic fields.

Although all the six quark flavors should be considered in eq. (2.64), only those with the smallest masses will contribute to this integral significantly.

In the first lattice simulations, $\det\big(\mathscr{D}_f\big)$ was set to 1, which is called *quenched approximation* and corresponds to neglecting the contribution of the quark fields on the gluon fields. In the language of perturbation theory, it is equivalent to neglecting fermionic loops in Feynman diagrams. In this quenched set-up, valence quarks were introduced to obtain hadronic correlation functions.

This limit is equivalent to assuming that quark and antiquark masses are very large and it has been proven surprisingly successful for the determination of different quantities that, in general, are not sensitive to the neglected quark loop diagrams, like some hadron masses. For instance, in 1993, continuum limits of eight hadron mass ratios reproduced the experimental results within an error of 6%, see [41]. However, examples of quantities that are affected by the quenched approximation are the η' mass and strange meson spectrum. For a review of the goodness of this approximation, see [86]. Today the simulations are performed with $\det(\mathscr{D}_f) \neq 1$, with strange and charm quarks not decoupled, respectively referred to as $N_f = 2+1$ and $N_f = 2+1+1$, where the two light quarks are degenerate.

However, the computation of an integral such as the one in eq. (2.64) is very expensive as it is high-dimensional. The numerical method for computing this type of integral is the Monte Carlo integration, and to perform the importance sampling for the Monte Carlo integration, one needs to generate gauge links with a Markov process, according to the probability distribution

$$P[U_\mu] = \frac{1}{\mathcal{Z}} e^{-S[U_\mu]} \prod_f \det(\mathscr{D}_f) \,. \tag{2.68}$$

Once they reach thermal equilibrium, the gauge links U_i are stored and can be reused to calculate statistical quantities by importance sampling. The gauge links that reach thermal equilibrium are also referred to as gauge configurations, and a set of gauge configurations is called an ensemble. As an example, the correlation function in eq. (2.64) can be computed by

$$\langle\, \mathrm{O}(\bar{q}, q, U) \,\rangle = \frac{1}{N} \sum_{i=1}^{N} \langle\, \mathrm{O}[\bar{q}, q, U_i] \,\rangle_W + \mathcal{O}\left(\frac{1}{\sqrt{N}}\right) , \tag{2.69}$$

where N is the number of gauge configurations, and $\mathcal{O}\left(\frac{1}{\sqrt{N}}\right)$ is the order of the statistical error.

Of course, it is convenient to generate as many gauge configurations N as possible to improve the statistical errors. However, this procedure can be pretty costly, depending on the choice of the action, its parameters, and the lattice volume. One of the central aims of the Coordinated Lattice Simulations initiative (CLS hereafter[3]) is to generate a variety of ensembles with different volumes V, kappas κ_f - the latter is related to the free quark mass by eq. (2.33) and β, which is related to the strong coupling g via eq. (2.42) and to the lattice spacing a, so that it is possible to extrapolate the quantities to the physical limit ($a \to 0$, $V \to \infty$, $m_\pi = m_\pi^{phys}$).

2.7 The Dirac propagator on the lattice

From now on, I keep the full notation x and y for the spacetime coordinates in the brackets. In the previous expressions of eqs. (2.66)-(2.67), $\mathscr{D}_d^{-1}(x, y)$ represents the quark propagator - with

---

[3] see the webpage https://wiki-zeuthen.desy.de/CLS/CLS and [50, 125]

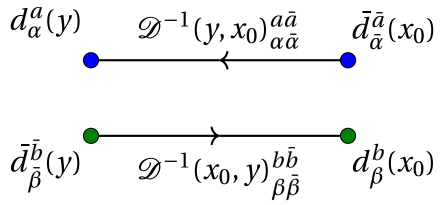

Figure 2.4:
The colored dots represent the location of the quarks and antiquarks on the lattice. The propagator between the blue dots is the forward d-quark propagator, while the one between the green dots is the backward propagator.

flavor *down* -, which is the most important quantity in lattice QCD simulations. It is a complex object with 3×3 color indices, 4×4 spin indices and $V\times V$ coordinates; for this reason it is called *all-to-all* propagator. Practically, it would take a lot of computer time to compute it numerically and would require a huge amount of memory to store it. Consider for example a volume with $N_s = 24$ and $N_t = 48$. The memory needed for the complex propagator of size $(3\times 4\times N_s^3 \times N_t)^2$ would be $\sim \mathscr{O}(10^6)$ GB, which is unfeasible for the computers today.

However, in some cases, we would only need the propagator

$$\mathscr{D}^{-1}(y,x_0)^{ba}_{\beta\alpha}\,, \tag{2.70}$$

which is called *point-to-all* because it describes the propagation of a particle from a fixed lattice site x_0 to any point on the lattice y. These objects are computed starting from a Dirac vector $\chi(x,x_0)^{ba_0}_{\beta\alpha_0}$, which is equivalent to the point-to-all propagator with a fixed color index a_0 and spin index α_0. Here I remove the flavor subscript f to simplify the notation.

The point-to-all is then computed by solving a system of linear equations,

$$\sum_y \mathscr{D}(x,y)^{cb}_{\gamma\beta}\,\mathscr{D}^{-1}(y,x_0)^{ba_0}_{\beta\alpha_0} = \chi(x,x_0)^{ca_0}_{\gamma\alpha_0}\,, \tag{2.71}$$

with

$$\chi(x,x_0)^{ca_0}_{\gamma\alpha_0} = \delta(x-x_0)\delta_{ca_0}\delta_{\gamma\alpha_0} \tag{2.72}$$

being the vector source for the inversion, which for the moment is localised at a single lattice site and it is called point source. The sum over color and spin indices is implied and $\mathscr{D}(x,y)$ is the Dirac operator. Eq. (2.71) is usually referred as inversion and it is performed using iterative solver algorithms, since $\mathscr{D}$ is a huge sparse matrix.

The simulation time is often dominated by the inversions, therefore one normally seeks for fast algorithms to perform them, see [78].

In the simulations, it may occur that not only the forward propagator $\mathscr{D}^{-1}(y,x_0)$ is needed, but also the backward propagator $\mathscr{D}^{-1}(x_0,y)$, which describes the quark propagating in the opposite direction, see Fig. 2.4. The backward propagators are not computed iteratively by solving a linear system, but using the γ^5-hermiticity of the action, see eq. (2.60), which results in the γ^5-hermiticity of the propagator,

$$\mathscr{D}^{-1}(x_0,y) = \gamma^5 \mathscr{D}^{-1}(y,x_0)^\dagger \gamma^5\,. \tag{2.73}$$

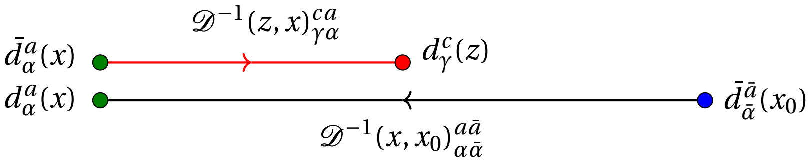

Figure 2.5: At the bottom there is the point-to-all propagator, while on top there is the all-to-all, marked by a red line.

Therefore, the backward propagators are computed from the forward propagators. It may also occur that the all-to-all propagators are needed to compute correlation functions. In some cases, they can be computed with the sequential method technique and in other cases with stochastic methods like the One-End trick. Both will be discussed in the next sections.

2.8 Sequential method

This technique can be used to compute lattice objects that are made up of products of an all-to-all propagator and point-to-all propagators. Consider for example the lattice object

$$S(z,x_0)^{c\bar{a}}_{\gamma\bar{\alpha}} = \mathscr{D}^{-1}(z,x)^{ca}_{\gamma\alpha}\,\mathscr{D}^{-1}(x,x_0)^{a\bar{a}}_{\alpha\bar{\alpha}}\,, \tag{2.74}$$

which is depicted in Fig. 2.5 and it is equivalent to the product of an all-to-all and a point-to-all propagator in color and spin space. We can avoid computing the all-to-all propagator and directly compute $S(z,x_0)$, by using $\mathscr{D}^{-1}(x,x_0)$ as a source for the inversion, similarly to $\chi(x,x_0)$ in eq. (2.71). Eq. (2.74) could be any linear combination $\tilde{S}(x,x_0)$ of point-to-all propagators and gamma matrices, i.e.

$$S(z,x_0)^{c\bar{a}}_{\gamma\bar{\alpha}} = \mathscr{D}^{-1}(z,x)^{ca}_{\gamma\alpha}\,\tilde{S}(x,x_0)^{a\bar{a}}_{\alpha\bar{\alpha}} \tag{2.75}$$

and $\tilde{S}(x,x_0)$ may contain any algebraic expressions that contain products of γ matrices, color contractions, et cetera. Hence, to obtain $S(z,x_0)$ in practice, we solve the linear system

$$\sum_z \mathscr{D}(x,z)^{ac}_{\alpha\gamma} S(z,x_0)^{c\bar{a}}_{\gamma\bar{\alpha}} = \tilde{S}(x,x_0)^{a\bar{a}}_{\alpha\bar{\alpha}}\,. \tag{2.76}$$

Since $S(z,x_0)$ is computed sequentially through combinations of point-to-all propagators, it will be referred to as the sequential propagator, while $\tilde{S}(x,x_0)$ is the sequential source.

In some cases, we need to project the interpolating operator at the lattice site x on a non-zero momentum $\mathbf{p}$. This is done by applying a momentum phase to the sequential source before the inversion, i.e.

$$S^{\mathbf{p}}(z,x_0)^{c\bar{a}}_{\gamma\bar{\alpha}} = \mathscr{D}^{-1}(y,x)^{ca}_{\gamma\alpha}\,e^{-i\mathbf{p}\cdot\mathbf{x}}\,\tilde{S}(x,x_0)^{a\bar{a}}_{\alpha\bar{\alpha}}\,. \tag{2.77}$$

Notice that in some cases, one should take into account the origin offset x_0, and the momentum projection at the sink becomes $e^{-i\mathbf{p}\cdot(\mathbf{x}-\mathbf{x_0})}$.

This technique was introduced in [114] to investigate the nucleon structure [29, 27], and it is now widely used also for other hadron structures like meson structure [77] and for baryon semileptonic decays to study CKM matrix elements [119, 120].

In this project, the sequential method was largely used, and in most cases, we use the sequential propagator $S(z, x_0)$ as a source for a second sequential propagator.

2.9 One-End Trick

As we see in the next chapter, the correlation functions are computed by evaluating traces of γ matrices and propagators. In some cases, the all-to-all propagators are needed, and it may occur that they cannot be computed with the sequential method (see Sec. 2.8). However, it may be possible to compute some correlation functions statistically with the so-called One-End trick, which was introduced in [47] and it is based on stochastic methods, see [76, 118, 117].

Consider, for example, two interpolating operators $\mathrm{O}_1(y)$ and $\bar{\mathrm{O}}_2(z)$ located respectively at $y = (\mathbf{y}, t)$ and $z = (\mathbf{z}, \tau)$, with t a fixed timeslice, such that the resulting correlation function at zero momentum is

$$C_{2pt}(t-\tau) = \sum_{\mathbf{y}}\sum_{\mathbf{z}} \langle \mathrm{O}_1(\mathbf{y}, t)\ \bar{\mathrm{O}}_2(\mathbf{z}, \tau)\rangle = \sum_{\mathbf{y}}\sum_{\mathbf{z}} \mathrm{Tr}\{\Gamma_1 \mathscr{D}^{-1}(z, y)\Gamma_2 \mathscr{D}^{-1}(y, z)\}\ , \tag{2.78}$$

and by using the γ^5-hermiticity property of the propagator it can be rewritten like

$$C_{2pt}(t-\tau) = \sum_{\mathbf{y}}\sum_{\mathbf{z}} \mathrm{Tr}\Big\{\gamma^5 \Gamma_1 \mathscr{D}^{-1}(z, y)\Gamma_2 \gamma^5 \mathscr{D}^{-1}(z, y)^{\dagger}\Big\}\ . \tag{2.79}$$

The propagators that appear in eq. (2.79) are all-to-all, or more clearly t-to-all, and we omit their flavor for clarity. They can be constructed by generating N_{stoc} random vectors $\eta^{(r)}(x)$ at the fixed timeslice T, with $r = 1, ..., N_{stoc}$ and with the properties

$$\langle \eta^{(r)}(x)\rangle_r \equiv \frac{1}{N_{stoc}} \sum_{r=1}^{N_{stoc}} \eta^{(r)}(x)^a_\alpha = 0\ , \tag{2.80}$$

$$\langle \eta^{(r)}(x)^a_\alpha \left(\eta^{(r)}(z)^{\dagger}\right)^b_\beta \rangle_r = \delta_{\mathbf{xz}}\delta_{ab}\delta_{\alpha\beta} + \mathscr{O}\left(\frac{1}{\sqrt{N_{stoc}}}\right)\ , \tag{2.81}$$

where $\langle \cdots \rangle_r$ represents the stochastic average over the N_{stoc} noise vectors, as shown in eq. (2.80). We invert the Dirac operator $\mathscr{D}^{-1}$ on each source $\eta^{(r)}(x)$ to obtain the solutions $\psi^{(r)}(z)$ and $\psi^{(r)}_{\Gamma_2}(z)$, that are

$$\psi^{(r)}(z) = \sum_{\mathbf{y}} \mathscr{D}^{-1}(z, y)\eta^{(r)}(y)\ , \tag{2.82}$$

$$\psi^{(r)}_{\Gamma_2}(z) = \sum_{\mathbf{y}} \mathscr{D}^{-1}(z, y)\left(\Gamma_2\gamma^5\right)^{\dagger} \eta^{(r)}(y)\ . \tag{2.83}$$

With these definitions, the two-point functions in eq. (2.79) take the form

$$C_{2pt}(t-\tau) = \sum_{r=1}^{N_{stoc}} \sum_{\mathbf{z}} \mathrm{Tr}\Big\{\gamma^5 \Gamma_1 \psi^{(r)}(z) \psi^{(r)}_{\Gamma_2}(z)^\dagger\Big\} . \tag{2.84}$$

For this project, we use the One-End trick to compute current-to-pion correlation functions with zero and non-zero momenta on both ends, where $\Gamma_1 = \Gamma$ and $\Gamma_2 = \gamma_5$, with $\Gamma \in \{\gamma^5, \gamma_\mu, \gamma_\mu\gamma^5\}$, so that eq. (2.79) becomes

$$C^{\mathbf{p}',\mathbf{q}}_{2pt}(t-\tau) = \sum_{\mathbf{y}} \sum_{\mathbf{z}} e^{-i\mathbf{p}'\cdot\mathbf{y}} e^{i\mathbf{q}\cdot\mathbf{z}} \mathrm{Tr}\Big\{\mathscr{D}^{-1}(z,y)^\dagger\, \gamma^5 \Gamma\, \mathscr{D}^{-1}(z,y)\Big\} . \tag{2.85}$$

We invert the Dirac operator on each source $\eta^{(r)}(x)$, and for one solution vector, we first project the source on the momentum $\mathbf{p}'$ by applying a conjugate phase. This results in the solutions $\psi^{(r)}(z)$ and $\psi^{(r)}_{\mathbf{p}'}(z)$, which are

$$\psi^{(r)}(z) = \sum_{\mathbf{y}} \mathscr{D}^{-1}(z,y) \eta^{(r)}(y) , \tag{2.86}$$

$$\psi^{(r)}_{\mathbf{p}'}(z) = \sum_{\mathbf{y}} \mathscr{D}^{-1}(z,y)\, e^{i\mathbf{p}'\cdot\mathbf{y}} \eta^{(r)}(y) \tag{2.87}$$

and eq. (2.85) can be rewritten like

$$C^{\mathbf{p}',\mathbf{q}}_{2pt}(t-\tau) = \sum_{r=1}^{N_{stoc}} \sum_{\mathbf{z}} e^{i\mathbf{q}\cdot\mathbf{z}}\ \mathrm{Tr}\Big\{\psi^{(r)}_{\mathbf{p}'}(z)^\dagger\, \gamma^5 \Gamma \psi^{(r)}(z)\Big\} . \tag{2.88}$$

There are many ways to generate noise vectors that follow a distribution $\mathbb{D}$, which has zero mean (see eq. (2.80)) and has the orthonormal property of eq. (2.81). In [67], the authors proved that sources with $\mathbb{Z}(2)$ noise, i.e. $\mathbb{D} = \mathbb{Z}(2) = \{+1, -1\}$, deviate less from the orthonormal condition of eq. (2.81), see Tab.1 of the above mentioned paper. We follow [76] with their optimal choice and use the complex number distribution $\mathbb{D} = \mathbb{Z}(2) \otimes i\mathbb{Z}(2)$, that is

$$\mathbb{D} = \left\{ \frac{1}{\sqrt{2}} (\pm 1 \pm i) \right\} , \tag{2.89}$$

which corresponds to $\mathbb{Z}(2)$ random noise vector both in the real and imaginary parts. This method is used in the literature also in combination with the sequential method to compute form factors in the light-light system, see [140, 141] and charm-light semileptonic decays [73].

2.10 Wuppertal Quark Smearing

The Wuppertal quark smearing is an iterative procedure to smooth the local interpolating operator $\mathrm{O}(x)$ at the level of the quarks. It was introduced in [89] to increase the overlap of the

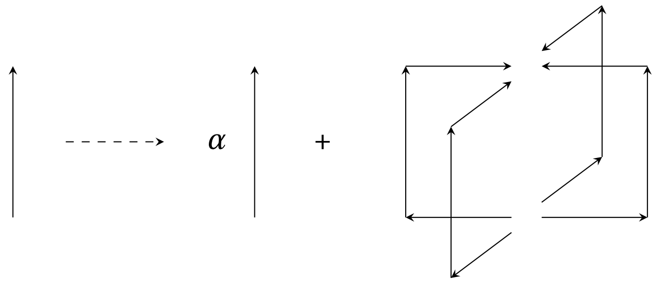

Figure 2.6:
The gauge links are averaged over their neighbouring incomplete plaquettes, each one with the shape of a staple.

hadron interpolating operator with the ground state (see discussion next chapter). In particular, the definition of the Wuppertal Smearing operator Φ_W applied to the quark fields $q(x)$ is

$$\Phi_W q(x) = \frac{1}{1+2d\kappa_s}\Big(q(x) + \kappa_s \sum_{\mu=\pm 1}^{\pm d} U_\mu(x) q(x+\hat{\mu})\Big) , \tag{2.90}$$

where $d = 3$ is the spatial dimension and κ_s is the smearing parameter characterizing the quark field's extension. This smoothing technique involves only the spatial components $\mu = 1, ..., d$ of the gauge fields U_μ. The Wuppertal operator can be applied n times iteratively and it can be expressed in terms of a lattice covariant Laplacian $\nabla^2 \equiv (\partial_i)^2$, so that

$$\Phi_W^{(n)} q(x) = \Big(\mathbb{1} + \frac{\kappa_s}{1+2d\kappa_s}\nabla^2\Big)^n q(x) . \tag{2.91}$$

With the definition of the covariant lattice derivative in eqs. (2.28)-(2.29), the discretized Laplacian operator applied to the quark fields $q(x)$ is

$$\nabla^2 q(x) = \sum_{\mu=\pm 1}^{\pm d} \Big(\nabla_\mu - \nabla_\mu^*\Big) q(x) = -2d q(x) + \sum_{\mu=\pm 1}^{\pm d} U_\mu(x) q(x+\hat{\mu}) . \tag{2.92}$$

After n steps, the quark fields are extended on the lattice with a Gaussian shape and the smearing radius is defined by

$$r_W^2 = \frac{\sum_{x\in\Lambda} |\mathbf{x}|^2 |q(x)|^2}{\sum_{x\in\Lambda} |q(x)|^2} . \tag{2.93}$$

For this project we have employed this smoothing technique and set $\kappa_s = 0.25$ with $n = 150$ iterations, but there are other types of quark smearing like Jacobi smearing [21].

2.11 Link smearing: APE smoothing

The APE smoothing is a particular type of gauge link smearing that is applied to the spatial directions $i = 1, 2, 3$ of the gauge links $U_i(x)$. These are averaged recursively over their neighbouring incomplete plaquettes called staples, as depicted in Fig. 2.6.

It has the following expression:

$$U_i^{(n+1)}(x) = \mathbb{P}_{SU(3)}\left\{\alpha U_i^{(n)}(x) + \sum_{j\neq i} C_{ij}^{(n)}(x)\right\}, \tag{2.94}$$

where the label n corresponds to the number of iterations and the term $C_{\mu\nu}^{(n)}(x)$ corresponds to the average of the gauge links over the staples; visualise it with the help of Fig. (2.6), i.e.

$$C_{\mu\nu}^{(n)}(x) = \sum_{\rho=\pm\nu} U_\rho^{(n)}(x)\; U_\mu^{(n)}(x+\hat{\rho})\; U_{-\rho}^{(n)}(x+\hat{\rho}+\hat{\mu})\,. \tag{2.95}$$

In eq. (2.94), $\mathbb{P}_{SU(3)}$ is the projecting operator defined by

$$\mathbb{P}_{SU(3)}\left\{V\right\} = X \in SU(3) \mid \max\left\{\,\mathrm{Re}\,\mathrm{Tr}\left\{\mathrm{XV}^\dagger\right\}\,\right\}, \tag{2.96}$$

which projects back the gauge links onto the group $SU(3)$ by maximizing the real part of the trace $\mathrm{Tr}\{XV^\dagger\}$. This method has had success in increasing the overlap with the physical states for different projects, including observation of string breaking effects [26] and searches for glueballs [17]. In this project, we have employed the APE link smearing with $\alpha = 2.5$ and $n = 25$ iterations, but there are other types of link smearing like HYP [92] and Stout smearing [126].

CHAPTER

THREE

UNVEILING THE NUCLEON STRUCTURE

In this chapter, I will discuss two-point functions and three-point functions of hadron operators. In particular, I will focus on the nucleon operators and show how to extract the finite-volume nucleon mass from the nucleon two-point functions and the nucleon matrix elements at finite-volume from the nucleon three-point functions.

I will conclude the chapter by discussing the contamination from excited states on the lattice and identify the main source of contamination.

3.1 Standard convention

The u- and d- quark propagators are defined as the Wick contractions of the specific quark and antiquarks, i.e.,

$$U^{a,b}_{\alpha\beta}(x,y) = \langle u^a_\alpha(x)\ \bar{u}^b_\beta(y)\rangle\ , \qquad D^{a,b}_{\alpha\beta}(x,y) = \langle d^a_\alpha(x)\ \bar{d}^b_\beta(y)\rangle\ , \tag{3.1}$$

where $q^a_\alpha(x)$ and $\bar{q}^b_\beta(y)$ are respectively the annihilation and the creation q-quark operator, with q being u or d. Notice the convention for the propagators and the symbol of Wick contractions with respect to eq. (2.66).

Second, in the previous chapters, I used $\mathscr{D}(x,y)$ for the Dirac operator, e.g. eq. (2.59), and $\mathscr{D}^{-1}(x,y)$ for its inverse, i.e. the Dirac propagator. From this chapter, I use the convention $\mathscr{D}^{-1}(x,y) \to D(x,y)$ for the propagators to simplify the notation. The Latin superscripts a, b in eq. (3.1) represent the color indices, and the Greek subscripts α, β are Dirac indices.

We also work in the isospin symmetry limit where the u-quarks and d-quarks have the same mass, i.e., are degenerate. In this limit, the two propagators are equivalent, and we will use

$$U(x,y) = D(x,y)\ . \tag{3.2}$$

However, it is relevant to mention that before carrying out the Wick contractions, one has to differentiate between u ad d quarks. As regards the representation for the gamma matrices, we adopt the same as it is implemented in the software packages that we use (CHROMA, GRID, GPT), and that corresponds to the DeGrand-Rossi basis. In the App. A, I write both the representation of the gamma matrices that we adopt and the Weyl (chiral) representation, often used in the continuum by some textbooks.

3.2 Two-point correlation functions

Let me recall that a general Euclidean two-point correlation function between two interpolating operators O_1 and $\bar{\mathrm{O}}_2$, respectively located at x and y is defined by

$$C_{2pt}(x,y) = \frac{\int \mathscr{D}[U]\mathscr{D}[q]\mathscr{D}[\bar{q}]\, e^{-S[U,q,\bar{q}]}\mathrm{O}_1(x)\ \bar{\mathrm{O}}_2(y)}{\int \mathscr{D}[U]\mathscr{D}[q]\mathscr{D}[\bar{q}]\, e^{-S[U,q,\bar{q}]}}\ , \tag{3.3}$$

where S is the prescribed QCD action. As explained in Sec. 2.6, we integrate out the fermionic variables and generate N gauge configurations U_i through a Markov process. In this way, the two-point function is computed statistically by

$$C_{2pt}(x,y) = \frac{1}{N}\sum_{i=1}^{N}\langle \mathrm{O}_1(U_i,q,\bar{q};x)\ \bar{\mathrm{O}}_2(U_i,q,\bar{q};y)\rangle + \mathscr{O}\left(\frac{1}{\sqrt{N}}\right)\ , \tag{3.4}$$

where $\langle \mathrm{O}_1(x)\ \bar{\mathrm{O}}_2(y)\rangle$ corresponds to the Wick contractions of the two interpolating operators. In the next sections, I will consider nucleon O_N and pion O_π interpolating operators. We will omit the statistical average over the gauge configurations, but we will implicitly intend it.

3.2.1 Pion two-point functions

In order to compute the pion two-functions statistically on the lattice, we first construct the (negative) pion interpolating operators at a fixed source position $x_0 = (\mathbf{x}_0, t_0)$ and sink $x = (x, t)$,

$$\mathrm{O}_{\pi^-}(x) = \bar{u}^a_\beta(x)\ \gamma^5_{\beta\alpha}\ d^a_\alpha(x)\ , \tag{3.5}$$

$$\bar{\mathrm{O}}_{\pi^-}(x_0) = -\bar{d}^{\bar{a}}_{\bar{\alpha}}(x_0)\ \gamma^5_{\bar{\alpha}\bar{\beta}}\ u^{\bar{a}}_{\bar{\beta}}(x_0)\ , \tag{3.6}$$

where the conventional minus sign is such that the correlation function is positive.

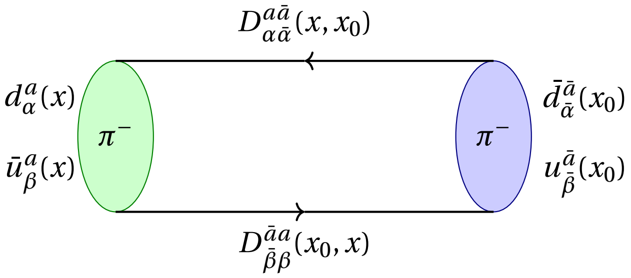

Figure 3.1:
A schematic plot of the propagators involved in the pion two-point functions. There is a forward and a backward point-to-all propagator.

The Wick contractions of these pion interpolating operators are

$$\begin{aligned} C^{\pi}_{2pt}(x, x_0) &= \langle \mathrm{O}_{\pi^-}(x)\, \bar{\mathrm{O}}_{\pi^-}(x_0)\rangle \\ &= -\langle\, \bar{u}^a_\beta(x)\gamma^5_{\beta\alpha} d^a_\alpha(x)\ \bar{d}^{\bar{a}}_{\bar{\alpha}}(x_0)\gamma^5_{\bar{\alpha}\bar{\beta}} u^{\bar{a}}_{\bar{\beta}}(x_0)\,\rangle \\ &= \langle\, \gamma^5_{\beta\alpha}\gamma^5_{\bar{\alpha}\bar{\beta}} u^{\bar{a}}_{\bar{\beta}}(x_0)\bar{u}^a_\beta(x)\ d^a_\alpha(x)\bar{d}^{\bar{a}}_{\bar{\alpha}}(x_0)\,\rangle \\ &= \gamma^5_{\beta\alpha}\gamma^5_{\bar{\alpha}\bar{\beta}}\ U^{\bar{a}a}_{\bar{\beta}\beta}(x_0, x)\ D^{a\bar{a}}_{\alpha\bar{\alpha}}(x, x_0) \\ &= \mathrm{Tr}\left\{\gamma^5 U(x_0, x)\gamma^5 D(x, x_0)\right\}\,. \end{aligned} \tag{3.7}$$

In the third line of eq. (3.9), I use the antisymmetric relations of the quark operators and the Wick's theorem to factorize the fermionic contractions. In order to project the interpolating operators on the momentum $\mathbf{p}_\pi = \frac{2\pi}{L}\mathbf{n}$, we apply the Fourier Transform as explained in App. A and eq. (3.7) becomes

$$C^{\pi}_{2pt}(\mathbf{p}_\pi, t, t_0) = \sum_{\mathbf{x}} e^{-i\mathbf{p}_\pi\cdot(\mathbf{x}-\mathbf{x}_0)} \langle \mathrm{O}_{\pi^-}(\mathbf{x}, t)\ \bar{\mathrm{O}}_{\pi^-}(\mathbf{x}_0, t_0)\rangle\,. \tag{3.8}$$

We also work in the isospin symmetry limit so that $U(x, x_0) = D(x, x_0)$.

Thus, the final expression for the pion two-point functions at finite momentum $\mathbf{p}_\pi$ is

$$C^{\pi}_{2pt}(\mathbf{p}_\pi, t, t_0) = \sum_{\mathbf{x}} e^{-i\mathbf{p}_\pi\cdot(\mathbf{x}-\mathbf{x}_0)}\,\mathrm{Tr}\left\{\gamma^5 D(x_0, x)\gamma^5 D(x, x_0)\right\}\,, \tag{3.9}$$

where $D(x, x_0)$ is the forward propagator and $D(x_0, x)$ is the backward propagator, and they are represented in Fig. 3.1. We can employ the γ^5-hermiticity of the Dirac propagator, see eq. (2.73) and rewrite eq. (3.7) in terms of just the point-to-all propagator $D(x, x_0)$, like

$$C^{\pi}_{2pt}(\mathbf{p}_\pi, t, t_0) = \sum_{\mathbf{x}} e^{-i\mathbf{p}_\pi\cdot(\mathbf{x}-\mathbf{x}_0)}\,\mathrm{Tr}\Big\{D(x, x_0)^\dagger D(x, x_0)\Big\}\,, \tag{3.10}$$

where the trace is taken over color and spin indices. One can compute the Fourier Transform of the product inside the brackets in eq. (3.10) for every gauge configuration and have a statistical average of the pion two-point functions, see eq. (3.4).

On the other end, we can employ the spectral decomposition and insert a complete set of states between the two interpolating operators in eq. (3.8),

$$\mathbb{1} = \sum_n \frac{1}{2E_n} |n\rangle \langle n| \ , \tag{3.11}$$

where I omit a conventional volume factor V in the denominator so that the spectral decomposition for the pion two-point functions reads

$$\begin{aligned} C^{\pi}_{2pt}(\mathbf{p}_\pi, t, t_0) &= \sum_{\mathbf{x},n} e^{-i\mathbf{p}_\pi\cdot(\mathbf{x}-\mathbf{x}_0)} \frac{1}{2E_n} \langle\Omega|\mathrm{O}_{\pi^-}(\mathbf{x},t)|n\rangle \langle n|\bar{\mathrm{O}}_{\pi^-}(\mathbf{x}_0,t_0)|\Omega\rangle \\ &= \frac{e^{-E_\pi(t-t_0)}}{2E_\pi} \left\langle\Omega\middle|\mathrm{O}_{\pi^-}(\mathbf{p}_\pi)\middle|\pi(\mathbf{p}_\pi)\right\rangle \left\langle\pi(\mathbf{p}_\pi)\middle|\bar{\mathrm{O}}_{\pi^-}(\mathbf{p}_\pi)\middle|\Omega\right\rangle + \ldots \end{aligned} \tag{3.12}$$

In the second line, I assume that the dominant states that are created from the vacuum $|\Omega\rangle$ by our interpolating operators are pions $\left|\pi(\mathbf{p}_\pi)\right\rangle$, and I use the space translation and time evolution operators to the operator $\mathrm{O}_\pi(\mathbf{x},t)$, as explained in Sec. A.4 of the App. A.

However, every state $|\tilde n\rangle$ with the same quantum numbers as the pions could be created and it is included in the dots. Generally, these states could be either excited states ("ES" in the following) or multi-particle states ("MPS"), and they fall off exponentially with an energy higher than E_π. Therefore they will be exponentially suppressed at large time t, and in this limit, we expect that the ground state, which is the pion in this case, is dominant.

The finite-volume energy is parametrised by the form $E_\pi = \sqrt{\left|\mathbf{p}_\pi\right|^2 + m_\pi^2}$ and thus it depends on the lattice momentum $\mathbf{p}_\pi$ and on the finite-volume mass m_π. The energy E_π and the matrix elements $\langle\Omega|\, \mathrm{O}_{\pi^-} \left|\pi(\mathbf{p}_\pi)\right\rangle$ can be extracted from a fit to the two-point pion correlation functions.

From now on, I will consider a trivial source position $x_0 = 0 = (\mathbf{0}, 0)$ for brevity and without loss of generality. However, in the actual simulation, I create the source at a non-zero position.

3.2.2 Nucleon two-point functions

We define the annihilation nucleon operator O_N at the sink $x = (\mathbf{x}, t)$ and the creation nucleon operator $\bar{\mathrm{O}}_N$ at the source $0 = (\mathbf{0}, 0)$ [1] in the following way

$$\mathrm{O}_{N,\gamma}(x) = \epsilon^{abc} \left(d^a_\alpha(x)\, \tilde C_{\alpha\beta}\, u^b_\beta(x) \right) q^c_\gamma(x) \ , \tag{3.13}$$

$$\bar{\mathrm{O}}_{N,\bar\gamma}(0) = \epsilon^{\bar a\bar b\bar c}\, \bar q^{\bar c}_{\bar\gamma}(0) \left(\bar u^{\bar b}_{\bar\beta}(0)\, \tilde C_{\bar\beta\bar\alpha}\, \bar d^{\bar a}_{\bar\alpha}(0) \right) , \tag{3.14}$$

where $\tilde C = C\gamma^5$. With this convention, the proton and nucleon interpolating operators are constructed respectively when $q = u, d$. The nucleon two-point functions read

$$C^N_{2pt}(\mathbf{p}_N, t) = \sum_{\mathbf{x}} e^{-i\mathbf{p}_N\cdot\mathbf{x}} \langle\, \mathbb{P}_{\bar\gamma\gamma}\, \mathrm{O}_{N,\gamma}(\mathbf{x},t)\, \bar{\mathrm{O}}_{N,\bar\gamma}(\mathbf{0},0)\, \rangle = \sum_{\mathbf{x}} e^{-i\mathbf{p}_N\cdot\mathbf{x}}\, C^N_{2pt}(\mathbf{x},t) \ , \tag{3.15}$$

---

[1] In the general case of a non-zero origin, one has to take into account the momentum phase related to the source position in the Fourier transform as in eq. (A.47) of App. A.

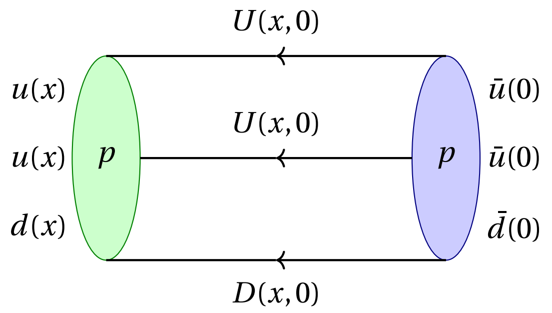

Figure 3.2:
A schematic plot of the propagators involved in the nucleon two-point functions. There are only forward point-to-all propagators and the color and spin indices are not explicitly written because there are two different Wick contractions for the u-quarks.

where $\mathbb{P}$ is the spin-parity projector and $\mathbf{p}_N$ is the momentum of the nucleon. The positive parity projector is $\mathbb{P}^+ = \frac{1}{2}(\mathbb{1} + \gamma^4)$, which is the Euclideanisation of $\mathbb{P}^+ = \frac{1}{2}(\mathbb{1} + \gamma^0)$. Here, I adopt the lattice representation, which is the DeGrand-Rossi basis, but in the App. A I also provide the Weyl (chiral) representation, which some textbooks prefer.

The other spin-parity projectors that are being used herein are

$$\mathbb{P}^{\pm} = \frac{1}{2}(\mathbb{1} \pm \gamma^4) \,, \tag{3.16}$$

$$\mathbb{P}^{j}_{\uparrow/\downarrow} = \frac{1}{2}(\mathbb{1} \pm i\gamma^5\gamma^j) \,, \tag{3.17}$$

$$\mathbb{P}^{+j}_{\uparrow/\downarrow} = \mathbb{P}^{+}\mathbb{P}^{j}_{\uparrow/\downarrow} \,, \tag{3.18}$$

$$\mathbb{P}^{+j}_{\updownarrow} = \frac{1}{2}(\mathbb{P}^{+j}_{\downarrow} - \mathbb{P}^{+j}_{\uparrow}) = \mathbb{P}^{+}(-i\gamma^5\gamma^j) \,, \tag{3.19}$$

where $\mathbb{P}^{j}_{\uparrow/\downarrow}$ are respectively the spin up/down projectors along the direction j, which can be used in combination with $\mathbb{P}^+$ to form $\mathbb{P}^{+j}_{\uparrow/\downarrow}$. In particular, after performing the Wick contractions with the proton interpolators and with the positive parity projector $\mathbb{P}^+$, we obtain

$$C^{p}_{2pt}(\mathbf{x}, t) = \epsilon^{abc}\epsilon^{\bar{a}\bar{b}\bar{c}}\, \mathbb{P}^{+}_{\bar{\gamma}\gamma}\, \tilde{C}_{\alpha\beta}\, \tilde{C}_{\bar{\beta}\bar{\alpha}}\, D^{a\bar{a}}_{\alpha\bar{\alpha}}(x,0)\Big(U^{c\bar{c}}_{\gamma\bar{\gamma}}(x,0)U^{b\bar{b}}_{\beta\bar{\beta}}(x,0) - U^{c\bar{b}}_{\gamma\bar{\beta}}(x,0)U^{b\bar{c}}_{\beta\bar{\gamma}}(x,0)\Big)\,. \tag{3.20}$$

In the isospin symmetry limit, $U(x,0) = D(x,0)$, so that combining eq. (3.15) with eq. (3.20) we get

$$C^{N}_{2pt}(\mathbf{p}_N, t) = \sum_{\mathbf{x}} e^{-i\mathbf{p}_N\cdot\mathbf{x}}\, \epsilon^{abc}\epsilon^{\bar{a}\bar{b}\bar{c}}\, \mathbb{P}^{+}_{\bar{\gamma}\gamma}\, \tilde{C}_{\alpha\beta}\tilde{C}_{\bar{\beta}\bar{\alpha}}\, D^{a\bar{a}}_{\alpha\bar{\alpha}}(x,0)\Big(D^{c\bar{c}}_{\gamma\bar{\gamma}}(x,0)D^{b\bar{b}}_{\beta\bar{\beta}}(x,0) - D^{c\bar{b}}_{\gamma\bar{\beta}}(x,0)D^{b\bar{c}}_{\beta\bar{\gamma}}(x,0)\Big)\,. \tag{3.21}$$

Since the nucleons are fermions, in the spectral decomposition of the nucleon two-point functions, we have to consider the spin of the particles so that

$$\begin{aligned}
C_{2pt}^{N}(\mathbf{p}_N, t) &= \sum_{\mathbf{x}} e^{-i\mathbf{p}_N\cdot\mathbf{x}} \sum_{n,\sigma} \frac{1}{2E_n} \mathbb{P}^{+}_{\bar{\gamma}\gamma} \, \langle \Omega | \mathrm{O}_{N,\gamma}(\mathbf{x}, t) | n, \sigma \rangle \, \langle n, \sigma | \bar{\mathrm{O}}_{N,\bar{\gamma}} | \Omega \rangle \\
&= \frac{e^{-E_N t}}{2E_N} \sum_{\sigma} \mathbb{P}^{+}_{\bar{\gamma}\gamma} \, \big\langle \Omega \big| \mathrm{O}_{N,\gamma}(\mathbf{p}_N) \big| N(\mathbf{p}_N, \sigma) \big\rangle \, \big\langle N(\mathbf{p}_N, \sigma) \big| \bar{\mathrm{O}}_{N,\gamma} \big| \Omega \big\rangle + \ldots \\
&= \frac{e^{-E_N t}}{2E_N} \sum_{\sigma} \mathbb{P}^{+}_{\bar{\gamma}\gamma} \, |Z_N|^2 \, u_N(\mathbf{p}_N, \sigma) \, \bar{u}_N(\mathbf{p}_N, \sigma) + \ldots \\
&= \frac{e^{-E_N t}}{2E_N} \, |Z_N|^2 \, \mathrm{Tr}\left\{ \frac{1}{2} (\mathbb{1} + \gamma^4) \, (-i \not{p}_N + m_N) \right\} + \ldots \\
&= |Z_N|^2 \, \frac{E_N + m_N}{E_N} \, e^{-E_N t} + \ldots
\end{aligned} \tag{3.22}$$

where in the third line, I define the overlap factors Z_N and the nucleon spinors $u_{N,\gamma}$ through the matrix elements

$$\big\langle \Omega \big| \mathrm{O}_{N,\gamma}(\mathbf{p}_N) \big| N(\mathbf{p}_N, \sigma) \big\rangle = Z_N \, u_{N,\gamma}(\mathbf{p}_N, \sigma) \, , \tag{3.23}$$

while in the fourth line, I use one of the relations for the Dirac spinors in Euclidean spacetime, that is

$$\sum_{\sigma} u_N(\mathbf{p}_N, \sigma) \, \bar{u}_N(\mathbf{p}_N, \sigma) = (-i \not{p}_N + m_N) \tag{3.24}$$

and in the final line, I compute the traces of Dirac matrices (see eq. (A.36) in App. A)). At large t, extracting the effective energy E_N^{eff} from a fit to the nucleon two-point functions is possible. In particular, at zero momentum $\mathbf{p} = \mathbf{0}$, we have that $E_N = m_N$ and the spectral decomposition of the nucleon two-point function gives

$$C_{2pt}^{N}(\mathbf{p}_N = \mathbf{0}, t) = \; 2|Z_N|^2 \, e^{-m_N t} \; + \; \ldots \tag{3.25}$$

The effective mass can be extracted at large t from a ratio of the two-point function at subsequent timeslices:

$$m_N^{\mathrm{eff}} = a^{-1} \log \left(\frac{C_{2pt}^{N}(\mathbf{p}_N = \mathbf{0}, t)}{C_{2pt}^{N}(\mathbf{p}_N = \mathbf{0}, t + a)} \right) . \tag{3.26}$$

We computed eq. (3.21) using local nucleon operators and smeared nucleon operators. The latter were constructed by applying the Wuppertal smearing operator to the quark fields and the APE link smoothing to the gauge links. In more detail, we smeared at the source position by inverting the Dirac operator on a smeared source, i.e.,

$$\sum_{x} \mathscr{D}(y, x)^{cb}_{\gamma\beta} \, D(x, \Phi 0)^{ba_0}_{\beta\alpha_0} = \Phi_W^{(n)} \, \chi(y, 0)^{ca_0}_{\gamma\alpha_0} \, , \tag{3.27}$$

where $\Phi_W^{(n)}$ is the Wuppertal smearing operator defined in Sec. 2.10 and $\chi(y, 0)$ is a point source. We use the notation $D(x, \Phi 0)$ for the Dirac propagator that is smeared at the source 0.

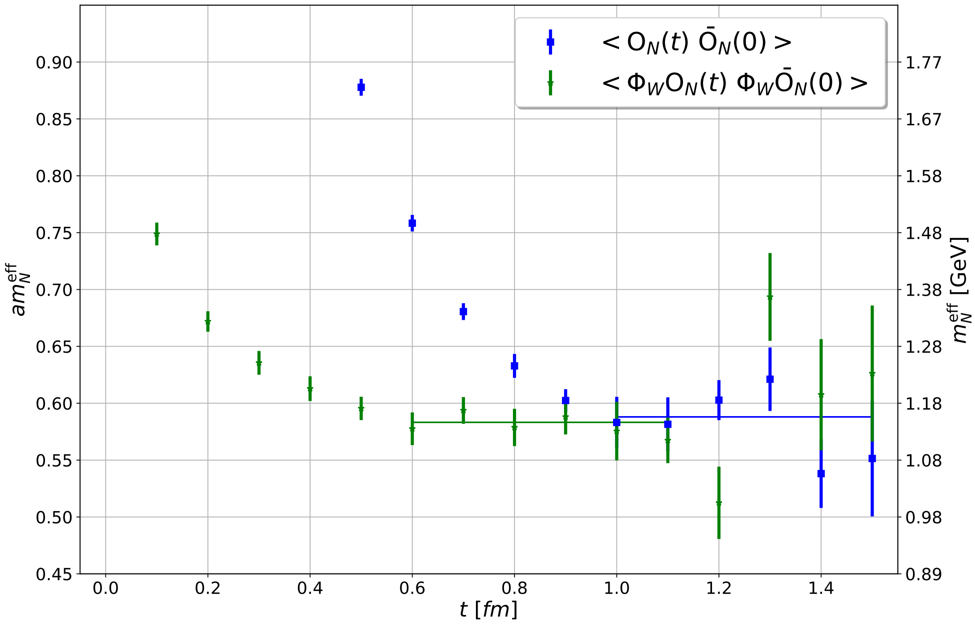

Figure 3.3:
In this plot, we show the effective mass calculated with eq. (3.26) using local and smeared nucleon operators. In the legend, the smeared nucleon operators are labelled by $\Phi_W O_N$. On the left, the y-axis is presented in lattice units, while on the right, it is shown in physical units (GeV).

We then smear at the sink x the source-smeared propagator $D(x, \Phi 0)$ by applying the smearing operator again to the propagator $D(x, \Phi 0)$ and we obtain $D(\Phi x, \Phi 0) = \Phi_W^{(n)} D(x, \Phi 0)$. We use the CLS ensemble A653, whose parameters are gathered in Tab. F.1 and we compute the nucleon two-point functions using local and smeared nucleon operators. In Fig. 3.3, we compare the nucleon effective masses calculated with eq. (3.26) using local and smeared operators. In both cases, there is evidence of a plateau region around the same value. However, with the smearing, the plateau starts earlier. In particular, with smeared nucleon interpolators, we find

$$m_N^{\text{eff}} = (0.583 \pm 0.006)\ a^{-1} = (1148.5 \pm 11.8)\ \text{MeV}\,. \tag{3.28}$$

It is clear that the nucleon mass on this ensemble is slightly heavier than the physical one, which is ~ 938 MeV. The conversion from lattice units (a^{-1}) to physical units (MeV), is done by recalling that $a \approx 0.1$ fm on this ensemble and that 1 fm $\approx$ (1/197) MeV^{-1}.

3.3 Nucleon three-point functions

With the insertion of an intermediate current

$$\mathscr{J}_k(z) = \bar{\psi}_\delta(z) \frac{\sigma_k}{2}\, \Gamma_{\delta\delta'} \psi_{\delta'}(z) \tag{3.29}$$

at $z = (\mathbf{z}, \tau)$, between the nucleon interpolating operators in eqs. (3.14)-(3.13), it is possible to compute the nucleon three-point functions, which have the following path integral representation

$$C_{3pt}^{\mathscr{J}_k}(x, z, 0) = \frac{\int \mathscr{D}[U]\mathscr{D}[\psi]\mathscr{D}[\bar{\psi}]\, e^{-S[U,\psi,\bar{\psi}]} \mathrm{O}_N(x)\ \mathscr{J}_k(z)\ \bar{\mathrm{O}}_N(0)}{\int \mathscr{D}[U]\mathscr{D}[\psi]\mathscr{D}[\bar{\psi}]\, e^{-S[U,\psi,\bar{\psi}]}} \,. \tag{3.30}$$

On the lattice, the nucleon three-point function reads

$$\begin{aligned} C_{3pt}^{\mathbb{P};\mathscr{J}_k}(\mathbf{p}'_N, t; \mathbf{q}, \tau) &= \sum_{\mathbf{x},\mathbf{z}} e^{-i\mathbf{p}'_N\cdot\mathbf{x}}\, e^{i\mathbf{q}\cdot\mathbf{z}} \,\langle\, \mathbb{P}_{\bar{\gamma}\gamma}\, \mathrm{O}_{N,\gamma}(\mathbf{x}, t)\ \mathscr{J}_k(\mathbf{z}, \tau)\ \bar{\mathrm{O}}_{N,\bar{\gamma}}(\mathbf{0}, 0)\,\rangle \\ &= \sum_{\mathbf{x},\mathbf{z}} e^{-i\mathbf{p}'_N\cdot\mathbf{x}}\, e^{i\mathbf{q}\cdot\mathbf{z}}\, C_{3pt}^{\mathbb{P};\mathscr{J}_k}(\mathbf{x}, t; \mathbf{z}, \tau)\,, \end{aligned} \tag{3.31}$$

where $C_{3pt}^{\mathbb{P};\mathscr{J}_k}(\mathbf{x}, t; \mathbf{z}, \tau)$ represents the sum of all the Wick contractions for this process, which depend on the quark fields composition of the nucleon and current operators. In particular, with the isotriplet current $\mathscr{J}_- = \mathscr{J}_1 - i\mathscr{J}_2 = \bar{d}\Gamma u$, a proton and a neutron interpolator at the source and at the sink, respectively, we have

$$\begin{aligned} C_{3pt}^{\mathbb{P};\mathscr{J}_-}(\mathbf{p}'_n, t; \mathbf{q}, \tau) &= \sum_{\mathbf{x},\mathbf{z}} e^{-i\mathbf{p}'_n\cdot\mathbf{x}}\, e^{i\mathbf{q}\cdot\mathbf{z}} \,\langle\, \mathbb{P}_{\bar{\gamma}\gamma}\, \mathrm{O}_{n,\gamma}(\mathbf{x}, t)\ \mathscr{J}_-(\mathbf{z}, \tau)\ \bar{\mathrm{O}}_{p,\bar{\gamma}}(\mathbf{0}, 0)\,\rangle \\ &= \sum_{\mathbf{x},\mathbf{z}} e^{-i\mathbf{p}'_n\cdot\mathbf{x}}\, e^{i\mathbf{q}\cdot\mathbf{z}}\, C_{3pt}^{\mathbb{P};\mathscr{J}_-}(x, z, 0)\,. \end{aligned} \tag{3.32}$$

The spin-parity operators $\mathbb{P}$ used here are $\mathbb{P}_{\updownarrow}^{+j}$, defined in eq. (3.19), but for the moment, I write a generic projector $\mathbb{P}$, as the discussion is general. There are two pairs of d-quarks and two pairs of u-quarks, thus the number of Wick contractions is $2! \times 2! = 4$, and the expression is

$$\begin{aligned} C_{3pt}^{\mathbb{P};\mathscr{J}_-}(x, z, 0) &= \langle\, \mathbb{P}_{\bar{\gamma}\gamma}\, \mathrm{O}_{N,\gamma}(x)\ \mathscr{J}_-(z)\ \bar{\mathrm{O}}_{N,\bar{\gamma}}(0)\,\rangle \\ &= \epsilon^{abc}\epsilon^{\bar{a}\bar{b}\bar{c}}\ \tilde{C}^{\alpha\beta}\ \tilde{C}^{\bar{\beta}\bar{\alpha}}\ \mathbb{P}_{\bar{\gamma}\gamma}\, \Gamma_\mu^{\delta\delta'} \left(D_{\gamma\delta}^{cd}(x, z)\ D_{\alpha\bar{\alpha}}^{a\bar{a}}(x, 0)\ -\ D_{\gamma\bar{\alpha}}^{c\bar{a}}(x, 0)\ D_{\alpha\delta}^{ad}(x, z)\,\right)\times \\ &\qquad \times \left(\, U_{\delta'\bar{\gamma}}^{d\bar{c}}(z, 0)\ U_{\beta\bar{\beta}}^{b\bar{b}}(x, 0)\ -\ U_{\delta'\bar{\beta}}^{d\bar{b}}(z, 0)\ U_{\beta\bar{\gamma}}^{b\bar{c}}(x, 0)\right). \end{aligned} \tag{3.33}$$

Fig. 3.4 shows a schematic plot of the proton to neutron three-point functions. It is possible to rewrite eq. (3.32) like

$$C_{3pt}^{\mathbb{P};\mathscr{J}_-}(\mathbf{p}'_n, t; \mathbf{q}, \tau) = \sum_{\mathbf{z}} e^{i\mathbf{q}\cdot\mathbf{z}}\ \mathrm{Tr}\Big\{\Big(\gamma^5\, S_{\bar{d}u}(z, 0)^\dagger\, \gamma^5\Big)\ \Gamma\ U(z, 0)\Big\}\,, \tag{3.34}$$

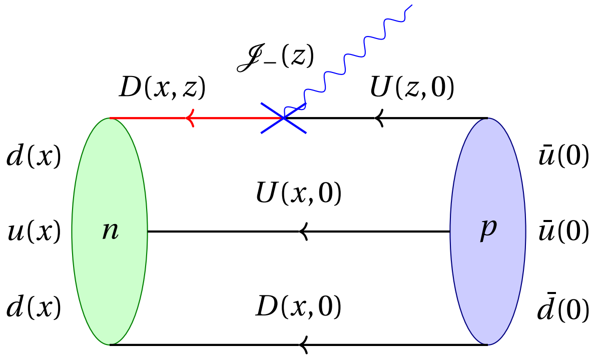

Figure 3.4:
A schematic plot of the proton to neutron three-point functions. The black solid lines are point-to-all propagators, while the red line is the all-to-all. The blue wavy line represents the interaction with the intermediate current $\mathcal{J}_-$ at the location z, marked by the blue crosses.

where $S_{\bar{d}u}(z,0)$ is the proton to neutron sequential propagator and it includes sequentially the propagators $D(x,0)$, $U(x,0)$ and $D(x,z)$, depicted in Fig. 3.4. This propagator is computed with the sequential method, by inverting on the sequential source, as explained in Sec. 2.8. In the App. E, I write the expressions explicitly for both lattice objects and their implementation.

In the case of an isovector current $\mathcal{J}_0 \equiv 2\mathcal{J}_3 = \bar{u}\Gamma u - \bar{d}\Gamma d \equiv \mathcal{J}_u - \mathcal{J}_d$, the proton three-point functions take the expression

$$C_{3pt}^{\mathbb{P};\mathcal{J}_0}(\mathbf{p}'_p, t; \mathbf{q}, \tau) = \sum_{\mathbf{x},\mathbf{z}} e^{-i\mathbf{p}'_p\cdot\mathbf{x}}\, e^{i\mathbf{q}\cdot\mathbf{z}} \,\langle\, \mathbb{P}_{\bar{\gamma}\gamma}\, \mathrm{O}_{p,\gamma}(\mathbf{x}, t)\; \mathcal{J}_0(\mathbf{z}, \tau)\; \bar{\mathrm{O}}_{p,\bar{\gamma}}(\mathbf{0}, 0) \,\rangle \,, \tag{3.35}$$

which corresponds to a proton to proton three-point function. The terms with $\mathcal{J}_u$ and $\mathcal{J}_d$ can be computed separately with the sequential method as in eq. (3.34), such that

$$C_{3pt}^{\mathbb{P};\mathcal{J}_0}(\mathbf{p}'_p, t; \mathbf{q}, \tau) = C_{3pt}^{\mathbb{P};\mathcal{J}_u}(\mathbf{p}'_p, t; \mathbf{q}, \tau) - C_{3pt}^{\mathbb{P};\mathcal{J}_d}(\mathbf{p}'_p, t; \mathbf{q}, \tau) \,. \tag{3.36}$$

In the Sec. E.3 of the App. E, I provide the expressions for the sequential propagators $S_{\bar{u}u}(z,0)$ and $S_{\bar{d}d}(z,0)$, that enter in the computation of eq. (3.36) and in the isospin symmetry limit we have $S_{\bar{d}u}(z,0) = S_{\bar{u}u}(z,0) - S_{\bar{d}d}(z,0)$, so that

$$C_{3pt}^{\mathbb{P};\mathcal{J}_-}(\mathbf{p}', t; \mathbf{q}, \tau) = C_{3pt}^{\mathbb{P};\mathcal{J}_0}(\mathbf{p}', t; \mathbf{q}, \tau) \,. \tag{3.37}$$

Notice that the neutron three-point functions with $\mathcal{J}_0$ are equal and opposite in sign to the proton three-point functions with $\mathcal{J}_0$. Also, the quark content at the sink in the three-point functions on the left-hand side is different than the one on the right-hand side. The spectral decomposition provides a dependence of the nucleon three-point functions on the finite-volume energies, vacuum to nucleon matrix elements like in eq. (3.23) and nucleon matrix elements of the type $\langle n|\mathcal{J}_-|p\rangle$ for eq. (3.32) and $\langle p|\mathcal{J}_0|p\rangle$ for eq. (3.36), which are very important, as I discussed in Chap. 1. This part deserves an appropriate discussion.

3.4 Nucleon matrix elements

For this section, I consider the proton three-point function of eq. (3.35), but the same argument holds for the other nucleon three-point functions. I employ the spectral decomposition by inserting two complete sets of states,

$$\begin{aligned}
C_{3pt}^{\mathbb{P}^j,\mathscr{J}_0}(\mathbf{p}', t; \mathbf{q}, \tau) &= \sum_{\mathbf{x},\mathbf{z}} e^{-i\mathbf{p}'\cdot\mathbf{x}}\, e^{i\mathbf{q}\cdot\mathbf{z}} \,\langle\, \mathbb{P}^j_{\bar{\gamma}\gamma}\, \mathrm{O}_{p,\gamma}(\mathbf{x}, t)\, \mathscr{J}_0(\mathbf{z},\tau)\, \bar{\mathrm{O}}_{p,\bar{\gamma}}(\mathbf{0},0)\,\rangle \\
&= \sum_N \mathbb{P}^j_{\bar{\gamma}\gamma}\, \langle\Omega|\mathrm{O}_{p,\gamma}(\mathbf{p}')\big|N(\mathbf{p}')\big\rangle \big\langle N(\mathbf{p}')\big|\mathscr{J}_0(\mathbf{q})\big|N(\mathbf{p})\big\rangle \big\langle N(\mathbf{p})\big|\bar{\mathrm{O}}_{p,\bar{\gamma}}|\Omega\rangle\, \frac{e^{-E'_N t}\, e^{-(E_N-E'_N)\tau}}{4E'_N E_N} \\
&= \sum_{\sigma,\sigma'} \mathbb{P}^j_{\bar{\gamma}\gamma}\, Z_p^{\mathbf{p}'}\, Z_p^{\mathbf{p}*}\, u_{p,\gamma}(\mathbf{p}',\sigma)\, \big\langle p(\mathbf{p}',\sigma')\big|\mathscr{J}_0(\mathbf{q})\big|p(\mathbf{p},\sigma)\big\rangle\, \bar{u}_{p,\bar{\gamma}}(\mathbf{p},\sigma)\, \frac{e^{-(E_N-E'_N)\tau}\, e^{-E'_N t}}{4E'_N E_N} + \ldots
\end{aligned} \tag{3.38}$$

Notice that for the momentum conservation, the momentum at the source is $\mathbf{p} = \mathbf{p}' - \mathbf{q}$. In the second line, $\big|N(\mathbf{p}',\sigma')\big\rangle$ and $\big|N(\mathbf{p},\sigma)\big\rangle$ represent respectively states that can be created by the proton interpolating operators at the sink and at the source. In the third line, the assumption is that only the protons are created both at the source and at the sink. However, multi-particles states ($N\pi$, $N\pi\pi$, ...) and radial excitation of the proton (N^*, ...) can be created as well, depending on the lattice size and pion mass.

The nucleon matrix elements $\big\langle p(\mathbf{p}',\sigma')\big|\mathscr{J}_0\big|p(\mathbf{p},\sigma)\big\rangle$ can be decomposed according to their Lorentz structure, which depends on the current $\mathscr{J}$:

$$\big\langle p(\mathbf{p}',\sigma')\big|\, \mathscr{J}_0\, \big|p(\mathbf{p},\sigma)\big\rangle = u_p(\mathbf{p}',\sigma')\; FF[\mathscr{J}]\; \bar{u}_p(\mathbf{p},\sigma)\,. \tag{3.39}$$

While the terms u_p and $\bar{u}_p$ are Dirac spinors of the proton, the term $FF[\mathscr{J}]$ represents the Lorentz decomposition of the nucleon matrix elements in terms of form factors, which have a dependence on the momentum transfer $Q^2 = -q^2$. We already discussed similar Lorentz decompositions in Sec. 1.2 of Chap. 1. In the case of a pseudoscalar $\mathscr{P}$ and an axial-vector $\mathscr{A}^\mu$ current, the Lorentz decompositions in Euclidean spacetime are

$$\big\langle p(\mathbf{p}',\sigma')\big|\, \mathscr{P}_0\, \big|p(\mathbf{p},\sigma)\big\rangle = u_p(\mathbf{p}',\sigma')\, \gamma^5 G_P(Q^2)\; \bar{u}_p(\mathbf{p},\sigma)\,, \tag{3.40}$$

$$\big\langle p(\mathbf{p}',\sigma')\big|\, \mathscr{A}_0^\mu\, \big|p(\mathbf{p},\sigma)\big\rangle = u_p(\mathbf{p}',\sigma')\, \left(\gamma^\mu\gamma^5 G_A(Q^2) - i\frac{Q^\mu}{2m_N}\gamma^5 G_{\tilde{P}}(Q^2)\right)\, \bar{u}_p(\mathbf{p},\sigma)\,. \tag{3.41}$$

The functions G_P, G_A and $G_{\tilde{P}}$ that parametrize the nucleon matrix elements, are respectively the pseudoscalar, axial and induced-pseudoscalar nucleon form factors. So, for example, the terms $FF[\mathscr{J}]$ that appear in eq. (3.39) for an axial-vector and pseudoscalar current are

$$FF[\mathscr{P}] = \gamma^5 G_P(Q^2)\,, \tag{3.42}$$

$$FF[\mathscr{A}^\mu] = \gamma^\mu\gamma^5 G_A(Q^2) - i\frac{Q^\mu}{2m_N}\gamma^5 G_{\tilde{P}}(Q^2)\,. \tag{3.43}$$

Using these Lorentz decompositions and the definition of the matrix elements in terms of Dirac spinors and overlap factors, see eq. (3.23), the spectral decomposition of the proton three-point functions in eq. (3.38) is

$$C_{3pt}^{\mathbb{P},\mathscr{J}_0}(\mathbf{p}'_p, t;\mathbf{q},\tau) = \; Z_p^{\mathbf{p}'} Z_p^{\mathbf{p}*} \;\mathrm{Tr}\left\{\mathbb{P}(-i\not{p}' + m_N) FF[\mathscr{J}](-i\not{p} + m_N)\right\} \; \frac{e^{-(E_N - E'_N)\tau} e^{-E'_N t}}{4E'_N E_N} + \ldots \tag{3.44}$$

where again $\mathbf{p} = \mathbf{p}' - \mathbf{q}$ and we use eq. (3.24) on both ends. It is possible to extract these nucleon form factors through a suitable ratio of nucleon three-point functions and two-point functions:

$$R^{\mathbb{P}}_{\mathscr{J}}(\mathbf{p}', t;\mathbf{q},\tau) \equiv \frac{C_{3pt}^{\mathbb{P}^j,\mathscr{J}_0}(\mathbf{p}', t;\mathbf{q},\tau)}{C^N_{2pt}(\mathbf{p}', t)} \sqrt{\frac{C^N_{2pt}(\mathbf{p}',\tau)\; C^N_{2pt}(\mathbf{p}', t)\; C^N_{2pt}(\mathbf{p}, t-\tau)}{C^N_{2pt}(\mathbf{p},\tau)\; C^N_{2pt}(\mathbf{p}, t)\; C^N_{2pt}(\mathbf{p}', t-\tau)}}\,. \tag{3.45}$$

The idea behind these operations is that after the spectral decomposition, the nucleon ground state contribution to the above ratio is time-independent, and the overlap factors cancel out. In particular, in the limit $0 \ll \tau \ll t$, the expression for the ratio in eq. (3.45) reads

$$R^{\mathbb{P}}_{\mathscr{J}}(\mathbf{p}', t;\mathbf{q},\tau) = \sqrt{\frac{E'_N E_N}{(E'_N + m_N)(E_N + m_N)}}\; \frac{1}{4E'_N E_N}\,\mathrm{Tr}\left\{\mathbb{P}(-i\not{p}' + m_N) FF[\mathscr{J}](-i\not{p} + m_N)\right\} + \ldots \tag{3.46}$$

After computing the traces of Dirac matrices which depend on the polarization projectors $\mathbb{P}$ and on the currents through $FF[\mathscr{J}]$ (see e.g. eqs. (3.42)-(3.43)), it is possible to extract the nucleon form factors from a fit to the ground state. In the Appendix, there are results of traces like in eq. (3.46) using the pseudoscalar, vector and axial currents, see eqs. (A.37)-(A.42).

In particular, if we fix the momentum at the sink to zero ($\mathbf{p}' = \mathbf{0}$), so that $E'_N = m_N$, $\mathbf{p} = -\mathbf{q}$, the ratios in eq. (3.46) for some specific choice of current and polarization projector are

$$R^{\mathbb{P}^j}_{\mathscr{P}}(\mathbf{0}, t;\mathbf{q},\tau) = \frac{q^j}{\sqrt{2E_N(E_N + m_N)}}\, G_P(Q^2) + \ldots \tag{3.47}$$

$$R^{\mathbb{P}^j}_{\mathscr{A}^j}(\mathbf{0}, t;\mathbf{q},\tau) = \frac{i}{\sqrt{2E_N(E_N + m_N)}} \left[(E_N + m_N) G_A(Q^2) - \frac{(q^j)^2}{2m_N} G_{\tilde{P}}(Q^2)\right] + \ldots \tag{3.48}$$

$$R^{\mathbb{P}^j}_{\mathscr{A}^j}(\mathbf{0}, t;\mathbf{q}_{\perp j},\tau) = \frac{i(E_N + m_N)}{\sqrt{2E_N(E_N + m_N)}} G_A(Q^2) + \ldots \tag{3.49}$$

$$R^{\mathbb{P}^j}_{\mathscr{A}^4}(\mathbf{0}, t;\mathbf{q},\tau) = \frac{q^j}{\sqrt{2E_N(E_N + m_N)}} \left[G_A(Q^2) + \frac{(m_N - E_N)}{2m_N} G_{\tilde{P}}(Q^2)\right] + \ldots \tag{3.50}$$

In the kinematic case with $\mathbf{q}$ such that $q^j = 0$, where j is the direction of the polarised spin, the ground state contribution to the ratio $R^{\mathbb{P}^j}_{\mathscr{A}^j}(\mathbf{0}, t;\mathbf{q},\tau)$, will be proportional only to $G_A(Q^2)$, apart from some kinematic factors, and this will make its extraction technically easier. This specific ratio is expressed in eq. (3.49) and by $\mathbf{q}_{\perp j}$, I intend that $q^j = 0$.

Analogously, one can fix the momentum at the source to zero ($\mathbf{p} = \mathbf{0}$), vary $\mathbf{p}'$ and obtain similar expressions as eqs. (3.47)-(3.50). However, the three-point functions are more expensive to compute this way with the (sink) sequential method, as one has to solve the sequential propagator for each momentum and polarization (see eq. (2.77)) and in lattice QCD simulations the computation of the propagators is typically the most expensive part (see Sec. 2.7).

Eq. (3.46) is known in the literature by the name of "ratio method", and it is largely applied for nucleon matrix elements with pseudoscalar, axial-vector and vector currents (see [30, 58]) and even with different actions (see [108]). However, the nucleon matrix elements and thus the form factors can also be extracted from a direct fit to the three- and two-point functions ([98]).

3.5 The forward limit: the axial charge g_A

The special case where the momentum carried by the current is zero ($\mathbf{q} = \mathbf{0}$) is the forward limit. For the momentum conservation $\mathbf{p}' = \mathbf{p}$ and the particles can be in the kinematic configuration where they are all at rest ($\mathbf{p}' = \mathbf{p} = \mathbf{q} = \mathbf{0}$). The only non-trivial ratio among eqs. (3.47)-(3.50) is

$$\mathrm{Im}\Big\{R^{\mathbb{P}^j}_{\mathscr{A}^j}(\mathbf{0}, t; \mathbf{0}, \tau)\Big\} \approx G_A(Q^2 = 0) = \tilde{g}_A \,, \tag{3.51}$$

where $\tilde{g}_A$ is the unrenormalised axial charge. In order to obtain the renormalised axial charge, we must multiply it by the axial renormalization constant Z_A and consider the improvement coefficients as explained in [135, 136, 56, 102], but here we neglect the mass terms and compute

$$g_A = Z_A(\beta)\, \tilde{g}_A \,. \tag{3.52}$$

In Fig. 3.5, I show results on a single ensemble (A653, see App. F for details) of the ratio

$$R_0 := Z_A \,\mathrm{Im}\Big\{R^{\mathbb{P}^j}_{\mathscr{A}^j}(\mathbf{0}, t; \mathbf{0}, \tau)\Big\} \tag{3.53}$$

with $Z_A(\beta = 3.34) = 0.7456(10)^{\mathrm{stat}}(57)^{\mathrm{syst}}$, which was computed in [31]. This ratio is presented at different source-sink separations ($7a \leq t \leq 14a$) with local nucleon operators and at three source sink separations ($12a \leq t \leq 14a$) with smeared nucleon operators.

In principle, the ratio $R^{\mathbb{P}^j}_{\mathscr{A}^j}(\mathbf{0}, t; \mathbf{0}, \tau)$ should be time-independent, see eq. (3.51). However, as you can see from Fig. 3.5 the data points with local operators have a clear time dependence and a symmetry with respect to the middle point $t/2$, which is the reason why they are shifted by $-t/2$ along the x-axis. The contamination from excited states is more significant when the current is located closer to the source ($\tau = 0$) or to the sink ($\tau = t$), and for this reason the axial charge g_A is extracted at the middle-point $\tau = t/2$. In the other case, when we use smeared nucleon operators, the ratio is flat, and this suggests that it is dominated by the nucleon ground state already with a source-sink separation of $t = 11a \approx 1.1$ fm. In the first case with local nucleon operators, the larger the source-sink separation, the closer the extracted value of g_A to the

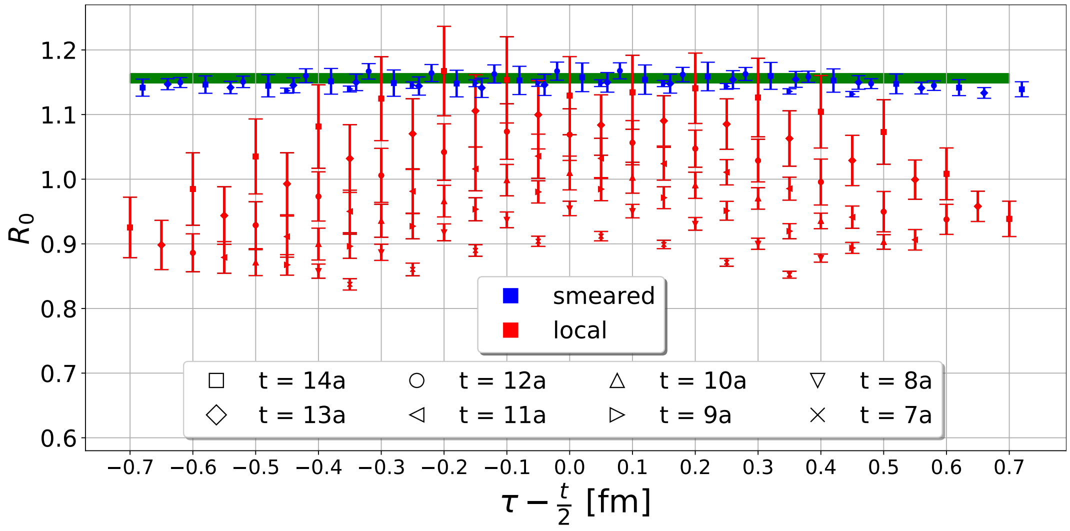

Figure 3.5:
In this figure, I show the ratio R_0 in eq. (3.53) at several source-sink separations $7a \leq t \leq 14a$ ($a \approx 0.1$ fm) with local nucleon operators and three source-sink separations $12a \leq t \leq 14a$ with smeared nucleon operators, see the two legends. The ratios with smeared nucleon operators are slightly shifted horizontally to improve their visibility. The two colours distinguish the two smearing levels, while the different symbols represent different source sink separations. The green band represents the estimate for the axial charge extracted using the smeared nucleon operators.

other case with smeared nucleon operators. Unfortunately, at large source-sink separations, the signal-to-noise ratio gets worse, and it prevents one from extracting the axial charge with less contamination from excited states. One would need more statistics to tackle this problem or a different approach, like for example, the summation method ([111, 57, 28, 91, 62, 1, 94, 45, 69]). We extract g_A by taking the average over the largest three source-sink separations in Fig. 3.5 and we find

$$g_A = 1.156 \pm 0.007\,. \tag{3.54}$$

This value of g_A is at finite-volume, unphysical quark masses and finite lattice spacing and will be used hereafter as a reference for other channels. In order to extrapolate to the continuum limit and physical point, one would need more ensembles with different V, κ_f and β. Only at that point, after a careful extrapolation with a ChPT ansatz, the lattice results for the axial charge can be compared to experimental results. This extrapolation in a, m_π and $m_\pi L$ is explained, for instance, in Chap. 10 of the FLAG review ([22]), where in Fig. 43 a comparison between lattice and experimental results for the axial charge is shown. This quantity is measured more precisely in the neutron beta decay experiments, see Sec. 1.2 in the introduction.

3.6 Nucleon form factors at $Q^2 \neq 0$

At non-zero momentum transfer, the nucleon form factors are extracted from the ratios in eqs. (3.47)-(3.50). Practically, we fix the nucleon momentum at the sink to zero and vary the momentum carried by the current. In Fig. 3.6, I show results of these ratios at different source-sink separations that are constructed with smeared nucleon operators and local currents. The latter are $\mathcal{O}(a)$-improved, i.e., $\mathcal{A}^{\mu}_{(imp)} = \mathcal{A}^{\mu} + c_A \partial^{\mu} \mathcal{P}$, where the $\mathcal{O}(a)$-improvement coefficient $c_A \approx -0.05571$ is obtained with the interpolation formula in eq. (4.1), following [52]. In each plot, the kinematic configuration is the same: $\mathbf{p}' = \mathbf{0}$ and the current momentum is the lowest non-zero lattice unit momentum, i.e., $\mathbf{q} = \hat{e}_j = \frac{2\pi}{L} \hat{n}^j$, where $\hat{n}^j$ is the unit vector along the direction j. Since there is momentum conservation, the nucleon at the source has momentum $\mathbf{p} = -\mathbf{q} = -\hat{e}_j$. There is no evidence of a plateau in each of these plots, but while the data points with $\mathcal{J} = \mathcal{P}, \mathcal{A}^j$ are flattening at large source-sink separations, see the first row and second row in Fig. 3.6, respectively, the situation with a temporal axial current is more dramatic, see the lowermost row of Fig. 3.6. For this channel, there is no evidence of nucleon ground state dominance, and it seems that this channel is more affected by excited state contamination.

The nucleon form factors extracted naively from eqs. (3.47), (3.48) and (3.50), i.e. without taking into account any excited state for the fit, are unreliable. In the literature, lattice groups tried multistate fits to take into account excited states contamination. In particular, one might assume that the same excited states that appear in the nucleon three-point functions are also created by the same nucleon operators in the nucleon two-point functions. In this traditional way, it is possible to either extract the excited state energy from a fit to the nucleon two-point functions and use it for the extraction of the form factors or perform a simultaneous fit to both correlation functions and extract all the unknown parameters.

However, the nucleon form factors that are extracted with this multistate fit in the traditional way, do not satisfy the so-called PCAC and PPD relations, which are discussed in more detail in Sec. 3.8. Such a failure has been observed in all lattice calculations that take the first energy gaps from the nucleon two-point functions and use them for the fit to the three-point functions, see [28, 18, 20, 19, 59, 96]. However, it is clear from Fig. 8 of [27] and Fig. 3 of [99] that the first energy gaps differ. First, in the nucleon two-point functions, the overlap factor that comes with the production of $N\pi$ states - or any general excited state - is modulus squared, i.e. $\propto |Z_{N\pi}|^2$, see eq. (3.22) and if $Z_{N\pi}/Z_N \propto 1/10$, then $|Z_{N\pi}/Z_N|^2 \propto 1/100$. While in the nucleon three-point functions, it is possible that the excited states are produced either at the source or at the sink, and these terms are proportional to $Z_{N\pi}$. Second, in the nucleon three-point functions there is the current matrix element $\langle N' \middle| \mathcal{J} \middle| N \rangle$, see (3.38), which could enhance some other states N', N with the same quantum numbers as the nucleon, for instance the $N\pi$ or $N\pi\pi$ states. Therefore, it is possible that a state that couples strongly to the three-point functions is extremely hard to detect in the two-point functions data.

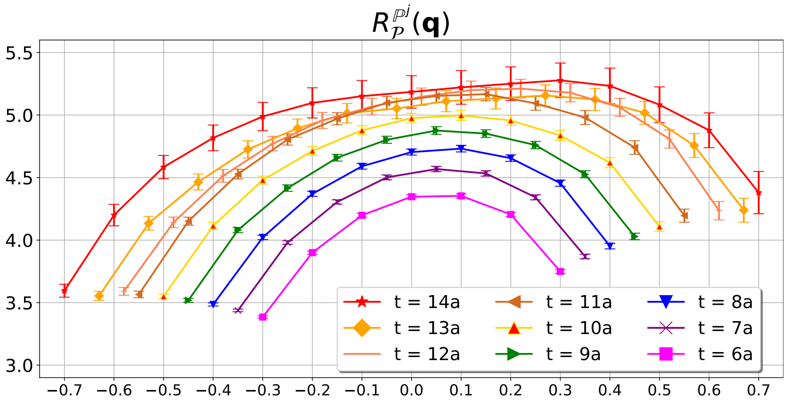

(a) In this plot, I show the ratio defined in eq. (3.47) for the pseudoscalar current $\mathscr{P}$ at different source-sink separations t, constructed from smeared nucleon operators. Even at large source-sink separations, the ratio is not constant, although it flattens.

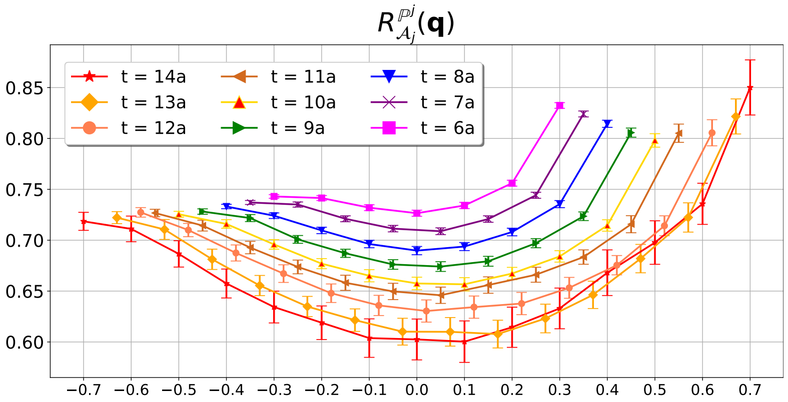

(b) In this plot, the ratio defined in eq. (3.48) for the spatial axial current $\mathscr{A}_j$ is plotted at different source-sink separations t, constructed from smeared nucleon operators. Even at large source-sink separations, the ratio is not constant, although it flattens.

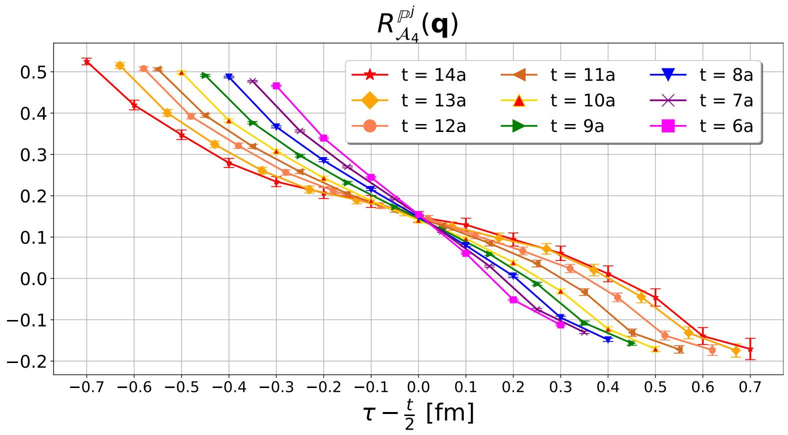

(c) In this plot, the ratio defined in eq. (3.50) with the temporal axial current $\mathscr{A}^4$ is plotted at different source-sink separations t, constructed from smeared nucleon operators. The situation seems to be more dramatic here because the data points are not flattening and it is unclear where the nucleon ground state lies.

Figure 3.6:
In this figure, I present the standard ratios constructed in eqs. (3.47), (3.48), and (3.50) in the kinematic configuration where the nucleon at the sink is at rest ($\mathbf{p}' = \mathbf{0}$), while the current carries the momentum $\mathbf{q} = \hat{e}_j$, so that the nucleon at the source is moving with momentum $\mathbf{p} = -\mathbf{q} = -\hat{e}_j$. In all these channels, the data points are not constant with time. However, while the data points with $\mathscr{J} = \mathscr{P}$ seem to flatten, the channel $\mathscr{A}^4$ does not show any sign of nucleon ground state dominance.

3.7 Parametrization of nucleon form factors

Before discussing the PCAC relation, let me first discuss some possible Q^2 parametrization of the nucleon form factors. After a reliable extraction of the nucleon form factors at different momentum transfer (Q^2) and the extrapolation to the physical point, it is possible to model the behaviour of the form factors with respect to Q^2. In some analyses, the model parametrization is also used at finite volume, see [27].

3.7.1 Dipole model

A standard parametrization that is adopted for the axial form factors is the dipole ansatz:

$$G_A(Q^2) = \frac{g_A}{\left[1-(Q^2/M_A^2)\right]^2}\,, \tag{3.55}$$

which corresponds to an exponentially decreasing spatial charge distribution (in position space) with an axial mass M_A. This parameter is computed by expanding eq. (3.55),

$$G_A(Q^2) = g_A\big(1-2(Q^2/M_A^2)+\ldots\big) \qquad \longrightarrow \qquad M_A^2 = \frac{-2g_A}{G'_A(Q^2=0\,\mathrm{GeV}^2)}\,, \qquad r_A^2 = \frac{12}{M_A^2}\,, \tag{3.56}$$

with $g_A = G_A(Q^2=0)$ and $G'_A(Q^2=0\,\mathrm{GeV}^2) = \frac{dG_A}{dQ^2}(Q^2=0\,\mathrm{GeV}^2)$.

This parametrization is chosen for the cross section of (anti)neutrino-nucleon scattering in the neutrino oscillation experiments ([9, 8, 10, 11, 12]), and they rely on the precise experimental determination of the axial charge. However, apart from recovering the large Q^2 limit analogously to the electromagnetic case (see [60] for the axial channel and [16, 105] for the electromagnetic form factors in perturbative QCD), no one guarantees that this model assumption is correct. The advantage of lattice QCD is that the nucleon form factors are extracted directly from the ratios and do not rely on a model-dependent parametrization.

3.7.2 z-expansion

An attempt at a model-independent parametrization that relies only on the analyticity of the form factors is the z-expansion,

$$G_A(Q^2) = \sum_{n=0}^{N} a_n^A\, z(Q^2)^n\,. \tag{3.57}$$

The form factors are written in powers of a new variable z, that is

$$z(Q^2) = \frac{\sqrt{t_{cut}+Q^2}-\sqrt{t_{cut}-t_0}}{\sqrt{t_{cut}+Q^2}+\sqrt{t_{cut}-t_0}}\,, \tag{3.58}$$

which maps the physical region $-Q^2_{max} \leq Q^2 < 0$ into a region of a unit circle $|z| \leq 1$. In the formula of eq. (3.57), t_0 is a free parameter that can be chosen to optimise the expansion, while t_{cut} depends on the physical system. For the nucleon axial form factors, $t_{cut} = (3m_\pi)^2$ as it takes into account the three pion production threshold. This model-independent parametrization is used to determine the mass parameter and also the form factors from (anti)neutrino-nucleon scattering experiments ([43, 44]) and it is also largely used for the electromagnetic form factors using electron-nucleon scattering data ([93, 72, 104]) and in semileptonic decays ([48]).

3.8 PCAC relation and the PCAC puzzle

A useful check for extracting the nucleon form factors comes from the Partially Conserved Axial Current (PCAC) relation. The QCD action with N_f massless flavours is symmetric under chiral rotations $SU(N_f)_A$[2] of the quark fields $q = (u, d, s, ...)$, i.e.

$$q(x) \quad \xrightarrow{SU(N_f)_A} \quad q'(x) = e^{i\alpha_a \gamma^5 t_a} q(x) \, , \tag{3.59}$$

$$\bar{q}(x) \quad \xrightarrow{SU(N_f)_A} \quad \bar{q}'(x) = \bar{q}(x) e^{i\alpha_a \gamma^5 t_a} \, , \tag{3.60}$$

but the state with the lowest energy, the vacuum, is not. The chiral symmetry is thus spontaneously broken or hidden. Nambu pointed out this hidden symmetry in [129] to explain the lightness of the pions, which arise as (pseudo) Goldstone bosons of the two-flavour QCD. In 1968, Gell-Mann Oakes and Renner showed in [83] that the square of the Nambu-Goldstone bosons mass is proportional to $m_u + m_d$:

$$m_\pi^2 = -2 \frac{(m_u + m_d)}{f_\pi^2} \langle \bar{\psi}\psi \rangle \, , \tag{3.61}$$

where $f_\pi \approx 130$ MeV and $\langle \bar{\psi}\psi \rangle = \langle \bar{u}u + \bar{d}d \rangle$ is the quark condensate, which serves as a pseudo order parameter for this spontaneous chiral symmetry breaking.

Lattice QCD simulations have shown that the quark condensate is different from zero even in the chiral limit, where the quarks are massless, proving that chiral symmetry is spontaneously broken, see for instance [84].

However, the quark mass term in the QCD action breaks the axial symmetry explicitly, and this leads to a non-conservation of the axial current $\mathscr{A}_\mu = \bar{q}\gamma_\mu\gamma_5 q$, which in Minkowski spacetime reads

$$\partial_\mu \mathscr{A}^\mu = 2 i m_\ell \, \mathscr{P} \, , \tag{3.62}$$

where $m_\ell = m_u = m_d$ in the isospin symmetry limit. Therefore, the divergence of the axial current is related to the pseudoscalar current $\mathscr{P} = \bar{q}\gamma_5 q$ and to the light quark mass. In the chiral limit ($m_u, m_d \to 0$), the chiral symmetry is restored, and the axial current is conserved.

---

[2] t_a are the $N_f^2 - 1$ generators of $SU(N_f)$.

If we consider eq. (3.62) applied to nucleon three-point functions, we have a PCAC relation at the level of the correlators like:

$$m_\ell = \frac{\partial_\mu C_{3pt}^{\mathbb{P},\mathscr{A}^\mu}(\mathbf{p}', t; \mathbf{q}, \tau)}{2i C_{3pt}^{\mathbb{P},\mathscr{P}}(\mathbf{p}', t; \mathbf{q}, \tau)} \,. \tag{3.63}$$

If we apply eq. (3.62) to the axial and pseudoscalar nucleon matrix elements and we employ their Lorentz decomposition (cf. eqs. (3.40)-(3.41)), we obtain

$$m_N G_A(Q^2) = m_\ell G_P(Q^2) + \frac{Q^2}{4m_N} G_{\tilde{P}}(Q^2) \,, \tag{3.64}$$

which is a PCAC relation that the form factors must fulfil. On a finite volume, these relations in eqs. (3.63)-(3.64) must be fulfilled up to $\mathscr{O}(a^2)$ discretization errors if we adopted a Wilson-Clover action with $\mathscr{O}(a)$-improvement.

It is time to discuss the so-called PCAC puzzle. It is related to the fact that analyses carried out with the ratio method (see eqs. (3.46)-(3.50)) lead to inconsistent checks for the PCAC relation at the level of the correlators (see eq. (3.63)) and for the form factors (see eq. (3.64)). In particular, the correlators satisfy the PCAC relation, but the form factors extracted from eqs. (3.47)-(3.50) do violate it, when one assumes that the first excited states in the nucleon three-point functions are the same as in the nucleon two-point functions. Indeed, from eq. (3.64) one can construct the ratio

$$r_{\text{PCAC}} = \frac{m_\ell G_P(Q^2) + \frac{Q^2}{4m_N} G_{\tilde{P}}(Q^2)}{m_N G_A(Q^2)} \tag{3.65}$$

and check whether $r_{\text{PCAC}} = 1 + \mathscr{O}(a^2)$, accordingly. It is also possible to check the pion-pole dominance (PPD) hypothesis, according to which the induced-pseudoscalar form factor $G_{\tilde{P}}$ can be written in terms of the axial form factor with the following expression:

$$G_{\tilde{P}}(Q^2) = \frac{4m_N^2 G_A(Q^2)}{m_\pi^2 + Q^2} \qquad \longrightarrow \qquad r_{\text{PPD}} = \frac{G_{\tilde{P}}(Q^2)(m_\pi^2 + Q^2)}{4m_N^2 G_A(Q^2)} \,, \tag{3.66}$$

and the ratio $r_{\text{PPD}} = 1 + \mathscr{O}(a^2)$ if PPD were to hold.

Unfortunately, neither PCAC nor PPD holds with the traditional fit ansatz, even including some excited states in the fit and with all the (known) systematics under control. In [30], our group investigated the perpendicular components of the axial and pseudoscalar currents. The result is that the form factors satisfy the PCAC, but still violate PPD.

Many analyses ([88, 139, 99, 97, 30]) reported this problem of ES contamination in different channels (vector, pseudoscalar and axial).

In particular, in [99], the authors employ a direct fit to the three-point functions using the traditional ansatz with up to three excited states in the fit, and the problem still persists. The excited-state contamination leads to unreliable extraction of the nucleon form factors and therefore of M_A and r_A. This problem has been solved only recently and will be discussed in the next section.

3.9 Contamination from $N\pi^n$ states and ChPT prediction

The nucleon form factors extracted with a traditional ansatz violate the PCAC and PPD relations. Other tools to investigate QCD at low energy are effective field theories that do not rely on an expansion with respect to the strong coupling [142, 63, 54]. In particular, chiral perturbation theory (ChPT) provides very useful information in this context; for example it predicts the above-mentioned PPD hypothesis, see [65, 64, 80, 81, 106, 42].

Some ChPT studies focus on the contamination of particular multi-particle states in two- and three-point functions: the $N\pi$ and $N\pi\pi$ states.

It is relevant to mention that $N\pi$ and $N\pi\pi$ states may have similar energies, which depend on m_π and V, see Fig. 2 in [87]. A proton at rest has definite positive parity, and while $N\pi$ must be in a P-wave with non-zero relative momentum for the nucleon and pion, the particles in $N\pi\pi$ states can be all at rest in an S-wave. Indeed, the total parity P of the $N\pi$ and $N\pi\pi$ states must be equal to the one of the nucleon at rest[3] $\mathrm{P}_N = +1$. Therefore, since parity is a multiplicative quantum number and $\mathrm{P}_\pi = -1$,

$$\mathrm{P}_{N\pi} = (-1)^L\, \mathrm{P}_N \mathrm{P}_\pi = (-1)^{L+1} \qquad \longrightarrow \qquad L = 1, \dots \text{ (P-wave, ...)}\,, \tag{3.67}$$

$$\mathrm{P}_{N\pi\pi} = (-1)^L\, \mathrm{P}_N (\mathrm{P}_\pi)^2 = (-1)^{L} \qquad \longrightarrow \qquad L = 0, \dots \text{ (S-wave, ...)}\,, \tag{3.68}$$

where L is the total angular momentum of the system. Therefore, if we neglect higher-order waves, the contamination to the nucleon with positive parity at rest is due to $N(\mathbf{p})\pi(-\mathbf{p})$ in P-wave states and $N(\mathbf{0})\pi(\mathbf{0})\pi(\mathbf{0})$ in S-wave states.

The contamination of these states in the nucleon two-point functions is rather small also at sufficiently small quark masses and large volumes, and while $N\pi$ states contribute to a few percent of the effective mass ([33]), the impact of $N\pi\pi$ states is estimated to be at the per mille level with a source-sink separation of $t = 1.2$ fm ([35]). Leading order ChPT predictions for the contribution of $N\pi$ states to the axial charge are also computed ([138, 34]), and they result in a 5% – 10% overestimation of the axial charge at a source-sink separation of 1.5 fm. But it is clear from Fig. 3.5 that the curvature is pointing downwards; thus the dominant contamination or the cumulative sum of all the contaminations should be overall negative. In [90], a possible sign for these downwards curvature could be explained by nucleon excitations like the Roper resonance.

The problem of excited state contamination becomes evident for non-zero momentum transfer. Indeed, the nucleon form factors violate eq. (3.64) and eq. (3.66), when they are extracted with a traditional ansatz, i.e. the ratio method. Even the inclusion of multiparticle states in the fit, whose energy is extracted from the nucleon two-point functions, does not help.

With a state-of-the-art analysis based on ChPT, our group extracted form factors that satisfy the PCAC and PPD relations, see [27, 146]. The idea is to compute the contribution of $N\pi$ states

---

[3] In Sec. 3.7, we explain that we fix the momentum of the nucleon at the sink to zero and vary $\mathbf{q}$. Therefore, $N\pi$ or $N\pi\pi$ states, that are produced at the sink, must have total momentum $\mathbf{0}$ and positive parity like the nucleon.

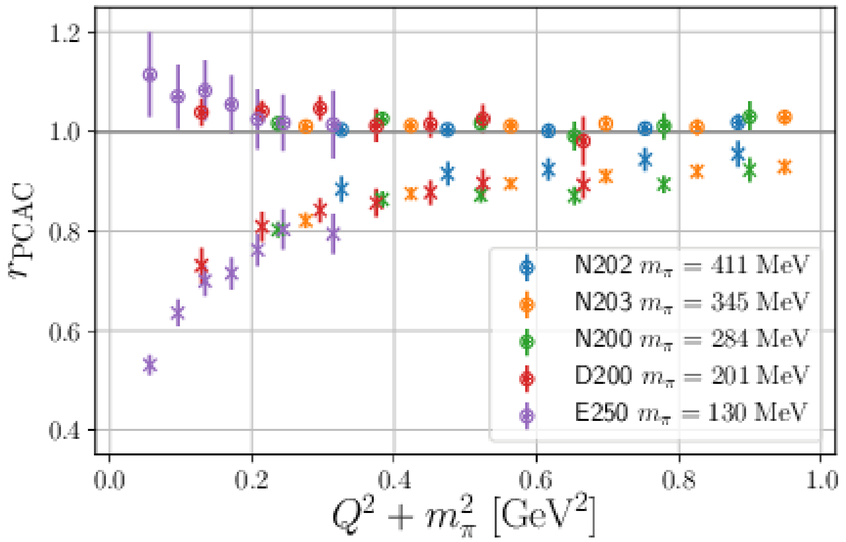

Figure 3.7:
In this plot, the PCAC ratio in eq. (3.65) is shown at finite volumes and with different pion masses but the lattice spacing is set to $a \approx 0.064$ fm. It is clear that while the circles agree within the error with the expected value, the crosses do not, and the smaller $Q^2 + m_\pi^2$ is, the more significant the discrepancy. The form factors for the crossed symbols were computed using the traditional ansatz, while the circles are computed with a novel method based on ChPT that takes into account $N\pi$ states. For further details, see [27].

to the nucleon three-point functions, that are produced either at the source or at the sink and use this new parametrization for the extraction of the form factors.

These corrections are computed at LO-ChPT, and for the axial and pseudoscalar currents, they read respectively

$$\delta^{\mathbb{P}^i,\mathscr{A}^\mu}_{\mathrm{LO-ChPT}}(\mathbf{p}',t;\mathbf{q},\tau) = \frac{Z_{\mathbf{p}'}Z_{\mathbf{p}}}{4E'_N E_N}\left[e^{-E_N t}e^{-E_\pi(t-\tau)}\frac{E'_N}{E_\pi}r^\mu_+(c'p^i+d'q^i)+e^{-E'_N t}e^{-E_\pi\tau}\frac{E_N}{E_\pi}r^\mu_-(cp'^i+dq^i)\right], \tag{3.69}$$

$$\delta^{\mathbb{P}^i,\mathscr{P}}_{\mathrm{LO-ChPT}}(\mathbf{p}',t;\mathbf{q},\tau) = \frac{Z_{\mathbf{p}'}Z_{\mathbf{p}}}{4E'_N E_N}\frac{m_\pi^2}{2m_\ell}\left[e^{-E_N t}e^{-E_\pi(t-\tau)}\frac{E'_N}{E_\pi}(c'p^i+d'q^i)-e^{-E'_N t}e^{-E_\pi\tau}\frac{E_N}{E_\pi}(cp'^i+dq^i)\right] \tag{3.70}$$

with $r_\pm = (E_\pi, \pm\mathbf{q})$, and c, c', d, d' are parameters defined in [27]. In particular, for the specific choice of kinematics that we standardly use ($\mathbf{p}' = \mathbf{0}$), the nucleon-pion states at the sink must have total momentum zero, while at the source, they must have total momentum $\mathbf{p} = -\mathbf{q}$.

As a comparison, I show in Fig. 3.7 the plot that is presented in [27] of the PCAC ratio using the conventional ansatz and the ChPT based parametrization.

ChPT is an effective field theory that is valid at small pseudoscalar meson masses and momenta. In this regime, the degrees of freedom are the pion and nucleon fields, and it shares the global symmetries of QCD, where the dynamic breaking of chiral symmetry is built in.

In [100], the authors address the problem with a different approach and are able to extract form factors that satisfy the PCAC and PPD relation. They extract the energy of the excited state using the current $\mathscr{A}^4 = \bar{q}\gamma^4\gamma^5 q$ in the nucleon three-point function and use the standard multi-particle fit. They identify these excited states with the $N\pi$ states through the dispersion relations, and they also claim that these states are the main responsible for the contamination.

3.10 Contamination of $N\pi$ in non-standard channels

Contamination from $N\pi$ states can be empirically observed in non-standard channels, even at $\mathbf{q} = \mathbf{0}$ (forward limit). Usually, the nucleon momentum at the sink is fixed to zero, but it is possible to project the nucleon operator at the sink to non-zero momentum. As an exploratory study, we consider a moving frame at the sink with the minimum non-vanishing lattice momentum $\mathbf{p}' = \hat{e}_i = \frac{2\pi}{L}\hat{n}_i$, where $\hat{n}_i$ is the unit vector along the direction i as in Sec. 3.6, but $\mathbf{q} = \mathbf{0}$, such that $|\mathbf{p}'| = |\mathbf{p}| \approx 526$ MeV.

Since $\mathbf{p}' = \mathbf{p}$, the standard ratio method defined in eq. (3.45) reduces to

$$R^{\mathbb{P}}_{\mathscr{J}}(\mathbf{p}', t; \mathbf{0}, \tau) \equiv \frac{C_{3pt}^{\mathbb{P}^j, \mathscr{J}_0}(\mathbf{p}', t; \mathbf{0}, \tau)}{C^N_{2pt}(\mathbf{p}', t)} \tag{3.71}$$

and we investigate the following ratios:

$$R_1 := Z_A \ \mathrm{Im}\left\{R^{\mathbb{P}^+_i}_{\mathscr{A}_i}(\mathbf{p}', t; \mathbf{q} = \mathbf{0}, \tau)\right\} \ = \ Z_A \tilde{g}_A + \ldots \tag{3.72}$$

$$R_2 := \left(-Z_A \frac{E}{p^i}\right) \mathrm{Re}\left\{R^{\mathbb{P}^+_i}_{\mathscr{A}_4}(\mathbf{p}', t; \mathbf{q} = \mathbf{0}, \tau)\right\} = Z_A \tilde{g}_A + \ldots \tag{3.73}$$

On the right-hand side, there is the nucleon ground state contribution to the specific ratios, and the ellipses encode all the terms with the same quantum numbers as the nucleon but higher energy. Notice that with this particular momentum configuration and specific spin-parity projectors, it is possible to extract the axial charge from the currents $\mathscr{A}_i$ and $\mathscr{A}_4$, see eqs. (3.72)-(3.73). Since we study the kinematic region with $\mathbf{q} = \mathbf{0}$, the quark mass independent $\mathscr{O}(a)$-improvement term proportional to c_A is vanishing.

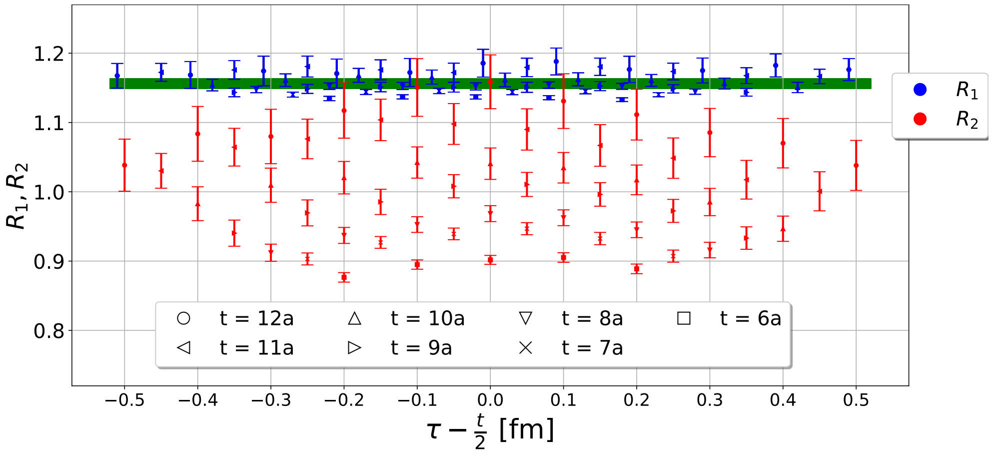

Figure 3.8:
The renormalized ratios R_1 and R_2 are plotted at different source-sink separations t. These ratios should approach the renormalized axial charge with $t \gg \tau \gg 0$, see eqs. (3.72)-(3.73) The two different colours distinguish the two ratios, see the legend on the right, while the symbols represent different source-sink separations. The green band is the value of g_A extracted from the rest frame, see Fig. 3.5.

In Fig. 3.8, we compare the renormalized axial charge extracted from the two ratios R_1 and R_2 by using smeared nucleon operators. To increase the statistics, we average the ratios R_1 and R_2 over all the six different directions: $\mathbf{p}' = \pm\hat{e}_x$, $\pm\hat{e}_y$, $\pm\hat{e}_z$. The resulting g_A from R_1 in Fig. 3.8 is consistent with the determination of g_A through R_0, see Fig. 3.5. However, it is clear from Fig. 3.8 that the axial charge extracted through the ratio R_2 with $\mathscr{A}_4$ is $\sim 10\% - 25\%$ smaller than with $\mathscr{A}_i$ with 0.6 fm $\leq t \leq 1.0$ fm, which is a relevant discrepancy. This was also observed in another study with a different Dirac operator and ensemble, see [107].

Following ref. [27] and eq. (3.69), there is no correction to consider at LO-ChPT for the channel with A_z, while there is a non-zero LO-ChPT correction to $\mathscr{A}_4$ due to $N\pi$ states produced either at the source or at the sink. This correction to the standard three-point function is due to $N(\hat{e}_z)\pi(\mathbf{0})$ and it reads

$$\delta^{\mathbb{P}^i,\mathscr{A}_4}_{\mathrm{LO-ChPT}}(\mathbf{p}', t; \mathbf{0}, \tau) = \frac{\sqrt{Z'}}{2E}\frac{\sqrt{Z}}{2E} cEp^i e^{-(E+\frac{m_\pi}{2})t} \cosh\left(m_\pi\left(\tau - \frac{t}{2}\right)\right) . \tag{3.74}$$

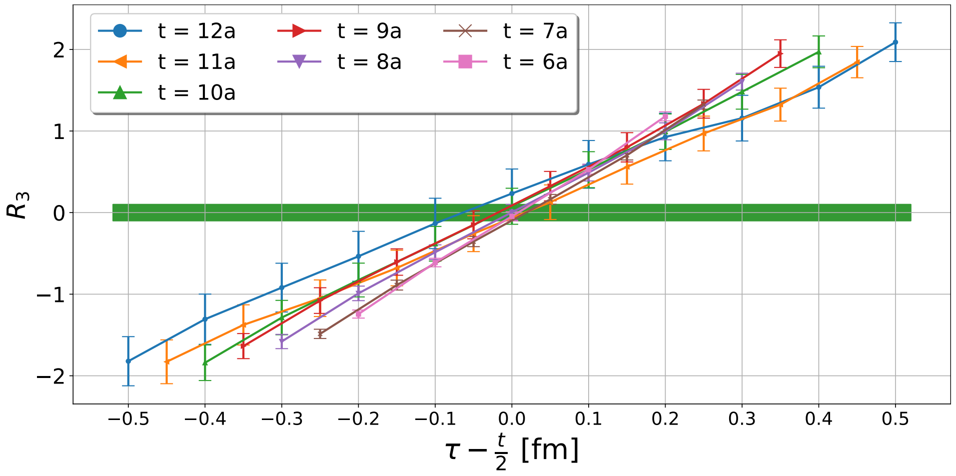

Figure 3.9:
The data points represent the ratio R_3 at different source-sink separations t, while the green band at 0 is the nucleon ground state contribution to this ratio.

As an exploratory study, we consider a pseudoscalar current and a moving frame at the sink with $\mathbf{p}' = \hat{e}_i$ and $\mathbf{q} = \mathbf{0}$. The ratio that we construct is thus

$$R_3 := \left(\frac{E}{p^i}\right) \mathrm{Re}\left\{R^{\mathbb{P}_i^+}_{\mathscr{P}}(\mathbf{p}', t; \mathbf{q} = \mathbf{0}, \tau)\right\} \;=\; 0 + \ldots \tag{3.75}$$

Notice that the nucleon ground state contribution to the ratio R_3 is expected to be zero. In Fig. 3.9, we show a clear non-zero signal for different source-sink separations and that it is antisymmetric with respect to $t/2$. Therefore, this signal is clearly due to excited or/and multi-particle state contamination.

Again, LO-ChPT predicts a non-zero contribution due to $N\pi$ states produced either at the source or at the sink, see eq. (3.70). This correction is coming again from $N(\hat{e}_z)\pi(\mathbf{0})$ and it gives:

$$\delta^{\mathbb{P}^i,\mathscr{P}}_{\mathrm{LO-ChPT}}(\mathbf{p}', t; \mathbf{0}, \tau) = \frac{\sqrt{Z'}}{2E}\,\frac{\sqrt{Z}}{2E}\, c E p'^i e^{-(E+\frac{m_\pi}{2})t} \sinh\left(m_\pi\left(\tau - \frac{t}{2}\right)\right) . \tag{3.76}$$

In the next chapter, I will introduce a new approach to tackle this problem of $N\pi$ states on the lattice by considering nucleon and nucleon-pion operators at the sink. This novel approach allows the computation of new three-point functions and matrix elements, which can be utilised to remove the $N\pi$ contamination directly. I will discuss more this in the next chapter.

CHAPTER

FOUR

MULTIPARTICLE INTERPOLATOR APPROACH

In this chapter, a novel approach will directly address the contamination of $N\pi$ states in the nucleon three-point functions, see [36]. The idea is to consider a nucleon-pion interpolating operator at the sink and a nucleon interpolator at the source with an intermediate current.

In section 1, I will discuss how to construct a nucleon-pion interpolating operator consistently to have the same quantum numbers as the nucleon. In section 2, I show the methods I employ to compute these new three-point functions, and in section 3, I discuss how to relate nucleon-pion two-point functions to the nucleon-to-nucleon-pion three-point correlation functions. In section 4, I derive some important relations for these two- and three-point functions through the Wigner-Eckart's theorem. In the final sections, I discuss how to extract $\langle N\pi|\mathscr{J}|N\rangle$ and $\langle N|\mathscr{J}|N\rangle$ matrix elements.

4.1 Nucleon to Nucleon-pion three-point functions

We have learned that the pion production has to be taken into account on the lattice to extract the form factors more reliably. The reason is that in the nucleon three-point functions $\langle \mathrm{O}_N(\mathbf{p}',t)\ \mathscr{J}(\mathbf{q},\tau)\ \bar{\mathrm{O}}_N(\mathbf{p},0)\rangle$, the $N\pi$ states could be created both at the source and at the sink. In this work, I consider the isovector current $\mathscr{J}_-$ at an intermediate spacetime $z=(\mathbf{z},\tau)$, which is defined as $\mathscr{J}_-(z)=\bar{d}(z)\Gamma u(z)$, and the standard nucleon three-point function in momentum space reads

$$\langle \mathrm{O}_n(\mathbf{p}',t)\ \mathscr{J}_-(\mathbf{q},\tau)\ \bar{\mathrm{O}}_p(\mathbf{p},0)\rangle\ . \tag{4.1}$$

The $N\pi$ states that contaminate this correlation function at the source must have the same isospin quantum numbers as the proton ($I=1/2$, $I_z=+1/2$) and total momentum $\mathbf{p}$, while at the sink, the $N\pi$ states must have the total momentum $\mathbf{p}'$ and the same quantum numbers as the neutron ($I=1/2$, $I_z=-1/2$, $S=1/2$).

The novel approach that I used is to compute the three-point functions

$$\langle \mathrm{O}_{N\pi}(\mathbf{p}', t)\ \mathscr{J}_{-}(\mathbf{q}, \tau)\ \bar{\mathrm{O}}_{N}(\mathbf{p}_N, 0)\rangle\ , \tag{4.2}$$

where I consider the nucleon interpolating operator at the source and a nucleon-pion interpolating operator at the sink so that $\mathrm{O}_{N\pi}(\mathbf{p}', t) = \mathrm{O}_N(\mathbf{p}'_N, t)\ \mathrm{O}_\pi(\mathbf{p}'_\pi, t)$. At the sink, the nucleon and pion operators lie on the same timeslice t, but they generally have different momenta with $\mathbf{p}' = \mathbf{p}'_N + \mathbf{p}'_\pi$. In the computation of standard nucleon three-point functions, the nucleon operator at the sink has a fixed momentum $\mathbf{p}' = \mathbf{0}$. To make a comparison with the standard correlation functions, I project the $N\pi$ interpolating operator at the sink such that $\mathbf{p}' = \mathbf{0}$ (rest frame) and $\mathbf{p}' = \mathbf{q}$ (moving frame). This multiparticle operator at the sink must be constructed to have the same quantum numbers as the neutron, as I have already mentioned above.

The isospin projection is carried out with the standard addition of isospin quantum numbers ($I = 1/2$ corresponds to the nucleons and $I = 1$ to pions), while the projection onto spin[1] $1/2$ is performed using the group theory projection tool, which is summarised in App. C.

The isospin projected nucleon-pion operator $\mathrm{O}_{N\pi}^{I, I_z}$ is

$$\mathrm{O}_{N\pi}^{1/2,\,-1/2} = +\frac{1}{\sqrt{3}}\ \mathrm{O}_n\ \mathrm{O}_{\pi^0} - \sqrt{\frac{2}{3}}\ \mathrm{O}_p\ \mathrm{O}_{\pi^-}\ , \tag{4.3}$$

where O_p and O_n are given in eq. (3.13) respectively with $q = u, d$, while $\mathrm{O}_{\pi^-} = \bar{u}\gamma^5 d$ as in eq. (3.5) and $\mathrm{O}_{\pi^0} = \frac{1}{\sqrt{2}}(\bar{u}\gamma^5 u - \bar{d}\gamma^5 d)$. For more details on the isospin projection, I send the reader to App. B. On the lattice, the corresponding irreducible representation of spin $1/2$ particles (and more) is G_1. Further details on the lattice group theory are in the App. C.

The combination of nucleon and pion with relative unit momenta and total momentum zero (rest frame) that produces a nucleon-pion system with spin $1/2$ aligned upwards along the z direction is

$$\begin{aligned}(\mathrm{O}_{N\pi})^{G_1}_{m_s=\uparrow}(\mathbf{p}' = \mathbf{0}) = &+ \mathrm{O}_{N\downarrow}(-\mathbf{e_x})\ \mathrm{O}_\pi(\mathbf{e_x}) - \mathrm{O}_{N\downarrow}(\mathbf{e_x})\ \mathrm{O}_\pi(-\mathbf{e_x}) + \\ &- i\mathrm{O}_{N\downarrow}(-\mathbf{e_y})\ \mathrm{O}_\pi(\mathbf{e_y}) + i\mathrm{O}_{N\downarrow}(\mathbf{e_y})\ \mathrm{O}_\pi(-\mathbf{e_y}) + \\ &+ \mathrm{O}_{N\uparrow}(-\mathbf{e_z})\ \mathrm{O}_\pi(\mathbf{e_z}) - \mathrm{O}_{N\uparrow}(\mathbf{e_z})\ \mathrm{O}_\pi(-\mathbf{e_z})\ ,\end{aligned} \tag{4.4}$$

$$\begin{aligned}(\mathrm{O}_{N\pi})^{G_1}_{m_s=\downarrow}(\mathbf{p}' = \mathbf{0}) = &+ \mathrm{O}_{N\uparrow}(-\mathbf{e_x})\ \mathrm{O}_\pi(\mathbf{e_x}) - \mathrm{O}_{N\uparrow}(\mathbf{e_x})\ \mathrm{O}_\pi(-\mathbf{e_x}) + \\ &+ i\mathrm{O}_{N\uparrow}(-\mathbf{e_y})\ \mathrm{O}_\pi(\mathbf{e_y}) - i\mathrm{O}_{N\uparrow}(\mathbf{e_y})\ \mathrm{O}_\pi(-\mathbf{e_y}) + \\ &- \mathrm{O}_{N\downarrow}(-\mathbf{e_z})\ \mathrm{O}_\pi(\mathbf{e_z}) + \mathrm{O}_{N\downarrow}(\mathbf{e_z})\ \mathrm{O}_\pi(-\mathbf{e_z})\ .\end{aligned} \tag{4.5}$$

---

[1] When we consider a system with non-zero momentum, we should refer to helicity for the general case. However, we always project the spin along the direction of the momentum, which is equivalent to the spin

In a moving frame like e.g. $\mathbf{p}' = n\hat{e}_z$ with $n \in \mathbb{N}$, it is possible to construct two operators for each helicity component m_s with the same quantum numbers as the nucleon. These are

$$(\mathrm{O}_{N\pi})^{G_1,1}_{m_s=\uparrow}(\mathbf{p}') = \mathrm{O}_{N,m_s=\uparrow}(\mathbf{p}')\,\mathrm{O}_{\pi}(\mathbf{0})\,, \qquad (\mathrm{O}_{N\pi})^{G_1,1}_{m_s=\downarrow}(\mathbf{p}') = -\mathrm{O}_{N,m_s=\downarrow}(\mathbf{p}')\,\mathrm{O}_{\pi}(\mathbf{0})\,, \tag{4.6}$$

$$(\mathrm{O}_{N\pi})^{G_1,2}_{m_s=\uparrow}(\mathbf{p}') = \mathrm{O}_{N,m_s=\uparrow}(\mathbf{0})\,\mathrm{O}_{\pi}(\mathbf{p}')\,, \qquad (\mathrm{O}_{N\pi})^{G_1,2}_{m_s=\downarrow}(\mathbf{p}') = -\mathrm{O}_{N,m_s=\downarrow}(\mathbf{0})\,\mathrm{O}_{\pi}(\mathbf{p}')\,. \tag{4.7}$$

The vectors $\mathbf{e}_i$ correspond to the unit vectors

$$\hat{e}_x = \frac{2\pi}{L}(1,0,0)\,, \qquad \hat{e}_y = \frac{2\pi}{L}(0,1,0)\,, \qquad \hat{e}_z = \frac{2\pi}{L}(0,0,1) \tag{4.8}$$

and the projection of O_N onto $m_s = \uparrow / \downarrow$ is made with the spin-parity projectors defined in eq. (3.18). For example, identifying 3 as the z-direction, the helicity components of the nucleon operators are

$$\mathrm{O}_{N,\uparrow} = \mathbb{P}^{+3}_{\uparrow}\mathrm{O}_N\,, \tag{4.9}$$

$$\mathrm{O}_{N,\downarrow} = \mathbb{P}^{+3}_{\downarrow}\mathrm{O}_N\,. \tag{4.10}$$

In more detail, the nucleon-pion operators $(\mathrm{O}_{N\pi})^{G_1,1}_{m_s=\uparrow/\downarrow}(\mathbf{p}')$ are relevant for the $N\pi$ contamination in the forward-limit ($\mathbf{q} = \mathbf{0}$), see Figs. 3.8,3.9; while the operators $(\mathrm{O}_{N\pi})^{G_1,2}_{m_s=\uparrow/\downarrow}(\mathbf{p}')$ are relevant for the $N\pi$ contamination at non-vanishing momentum transfer. This will be clear after this chapter, but it was already discussed in [27].

Having constructed the nucleon-pion operators, it is clear from eq. (4.3) that the three-point correlation functions to compute are

$$\langle\, \mathrm{O}_n(\mathbf{p}',t)\,\mathscr{J}_-(\mathbf{q},\tau)\,\bar{\mathrm{O}}_p(\mathbf{p},0)\,\rangle\,, \tag{4.11}$$

$$\langle\, \mathrm{O}_p(\mathbf{p}'_N,t)\,\mathrm{O}_{\pi^-}(\mathbf{p}'_\pi,t)\,\mathscr{J}_-(\mathbf{q},\tau)\,\bar{\mathrm{O}}_p(\mathbf{p},0)\,\rangle\,, \tag{4.12}$$

$$\langle\, \mathrm{O}_n(\mathbf{p}'_N,t)\,\mathrm{O}_{\pi^0}(\mathbf{p}'_\pi,t)\,\mathscr{J}_-(\mathbf{q},\tau)\,\bar{\mathrm{O}}_p(\mathbf{p},0)\,\rangle\,, \tag{4.13}$$

and the isospin projection of eq. (4.3) applied to the correlators gives:

$$\begin{aligned}\langle\, \mathrm{O}^{1/2,-1/2}_{N\pi}(\mathbf{p}',t)\,\mathscr{J}_-(\mathbf{q},\tau)\,\bar{\mathrm{O}}_p(\mathbf{p},0)\,\rangle = &+\frac{1}{\sqrt{3}}\langle\, \mathrm{O}_n(\mathbf{p}'_N,t)\,\mathrm{O}_{\pi^0}(\mathbf{p}'_\pi,t)\,\mathscr{J}_-(\mathbf{q},\tau)\,\bar{\mathrm{O}}_p(\mathbf{p},0)\,\rangle + \\ &-\sqrt{\frac{2}{3}}\langle\, \mathrm{O}_p(\mathbf{p}'_N,t)\,\mathrm{O}_{\pi^-}(\mathbf{p}'_\pi,t)\,\mathscr{J}_-(\mathbf{q},\tau)\,\bar{\mathrm{O}}_p(\mathbf{p},0)\,\rangle\,.\end{aligned} \tag{4.14}$$

The next step, discussed in the next section, is to perform the Wick contractions of these interpolating operators.

4.2 Diagrams and their computation

The correlations functions to compute are

$$C_{3pt}^{p\mathscr{J}\to p\pi^-}(\mathbf{p}'_p,\mathbf{p}'_\pi,t;\mathbf{q},\tau) = \langle \mathrm{O}_{p,\gamma}(\mathbf{p}'_N,t)\,\mathrm{O}_{\pi^-}(\mathbf{p}'_\pi,t)\,\mathscr{J}_-(\mathbf{q},\tau)\,\bar{\mathrm{O}}_{p,\bar{\gamma}}(\mathbf{p},0)\rangle\,, \tag{4.15}$$

$$C_{3pt}^{p\mathscr{J}\to n\pi^0}(\mathbf{p}'_n,\mathbf{p}'_\pi,t;\mathbf{q},\tau) = \langle \mathrm{O}_{n,\gamma}(\mathbf{p}'_N,t)\,\mathrm{O}_{\pi^0}(\mathbf{p}'_\pi,t)\,\mathscr{J}_-(\mathbf{q},\tau)\,\bar{\mathrm{O}}_{p,\bar{\gamma}}(\mathbf{p},0)\rangle\,, \tag{4.16}$$

where the momentum projection for the operator $\mathrm{O}_i(\mathbf{p})$ is performed via Fourier transformation. The number of Wick contractions of these processes is much larger than the one for the standard nucleon three-point functions. It increases factorially with the number of pairs of u-quarks and d-quarks. For the process $p+\mathscr{J}_-\to p\pi^-$, there are 2 pairs of u-quarks and 3 pairs of d-quarks. Therefore the number of permutations are $2!\times 3! = 12$.

These contractions can be split into diagrams with 4 different topologies: A, B, C and D, shown in Fig. 4.1.

Thus, the spacetime correlation function for this process can be written like

$$C_{3pt}^{p\mathscr{J}\to p\pi^-}(x,y,z) = C_{3pt,A}^{p\mathscr{J}\to p\pi^-}(x,y,z)+C_{3pt,B}^{p\mathscr{J}\to p\pi^-}(x,y,z)+C_{3pt,C}^{p\mathscr{J}\to p\pi^-}(x,y,z)+C_{3pt,D}^{p\mathscr{J}\to p\pi^-}(x,y,z)\,. \tag{4.17}$$

The expressions of the correlation functions for each diagram are written in App. D. The topologies A, B and C are connected because the correlation functions involve the computation of a single trace. The topology D, which can stand for "Disconnected", is made of two pieces: the nucleon term and the pion-current term.

The expression of the nucleon term corresponds essentially to the same as in the nucleon two-point functions (compare eq. (D.11) to eq. (3.20)), which can be computed on every gauge configuration with a single point-to-all propagator. Instead, the pion-to-current correlation function is made of two all-to-all propagators, and it is computed with the one-end-trick, see Sec. 2.9.

Like the standard nucleon three-point function, the correlation functions for the diagrams with topologies A, B and C can be expressed in terms of sequential propagators. In particular

$$C_{3pt,A}^{p\mathscr{J}\to p\pi^-}(\mathbf{p}'_N,\mathbf{p}'_\pi,t;\mathbf{q},\tau) = \sum_{\mathbf{z}} e^{i\mathbf{q}\cdot\mathbf{z}}\mathrm{Tr}\Big\{\big(\gamma^5\,S_2^\dagger(z,0)\gamma^5\big)\,\Gamma\,S_1(z,0)\Big\}\,, \tag{4.18}$$

where $S_1(z,0)$ is the (meson) sequential propagator and $S_2(z,0)$ is the nucleon sequential propagator because it is equivalent to the one for $p+J_{\bar{d}d}\to p$. You can visualise it in Fig. 4.2 and see the App. E for more details.

The diagrams with topology B are computed in the following way:

$$C_{3pt,B}^{p\mathscr{J}\to p\pi^-}(\mathbf{p}'_N,\mathbf{p}'_\pi,t;\mathbf{q},\tau) = \sum_{\mathbf{z}} e^{i\mathbf{q}\cdot\mathbf{z}}\mathrm{Tr}\Big\{\big(\gamma^5\,S_2^\dagger(z,0)\gamma^5\big)\,\Gamma\,U(z,0)\Big\}\,, \tag{4.19}$$

where $U(z,0)$ is the u-quark propagator from 0 to z in Fig. 4.1 and $S_2(z,0)$ is a sequential propagator, computed using the pion sequential propagator.

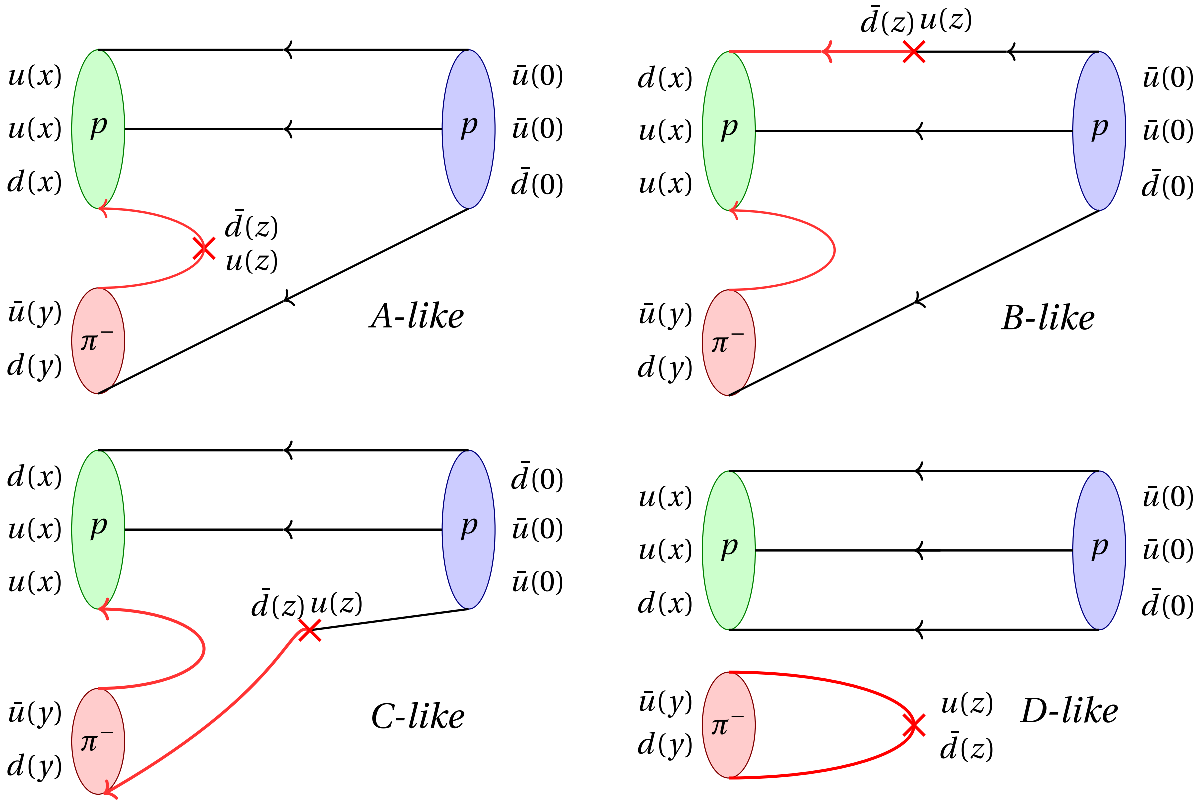

Figure 4.1:
This schematic plot represents the topologies A, B, C and D in the process $p+\mathcal{J}_- \to p+\pi^-$. There are two all-to-all propagators, which are marked with red lines. Notice that all the propagators in the diagrams with topologies A, B, C are sequentially connected, while in the D-like they are disconnected.

The diagrams with topology C are computed this way

$$C_{3pt,C}^{p\mathcal{J}\to p\pi^-}(\mathbf{p}'_N,\mathbf{p}'_\pi,t;\mathbf{q},\tau) = \sum_{\mathbf{z}} e^{i\mathbf{q}\cdot\mathbf{z}}\mathrm{Tr}\Big\{\big(\gamma^5\, S_2^\dagger(z,0)\gamma^5\big)\,\Gamma\, D(z,0)\Big\}\,, \tag{4.20}$$

where $D(z,0)$ is the d-quark propagator from 0 to z in Fig. 4.1 and $S_2(z,0)$ is a sequential propagator, which is computed using $S_{\bar{u}u}^{p\to p}$, that is the nucleon sequential propagator for the process $p+\mathcal{J}_u \to p$. For the other process $p+\mathcal{J}_- \to n\pi^0$, there are in total $2!\times 2!\times 3! = 24$ Wick contractions, which reduce to 16 in the isospin symmetry limit, where the u-quark and the d-quark propagators are equivalent.

These contractions can be split into the diagrams with topologies A, B and C, as shown in Fig. 4.2. For the standard process $p+\mathcal{J}_- \to n$, there are only 4 different Wick contractions. Important information for future reference is that the disconnected diagram ($D-like$) plays

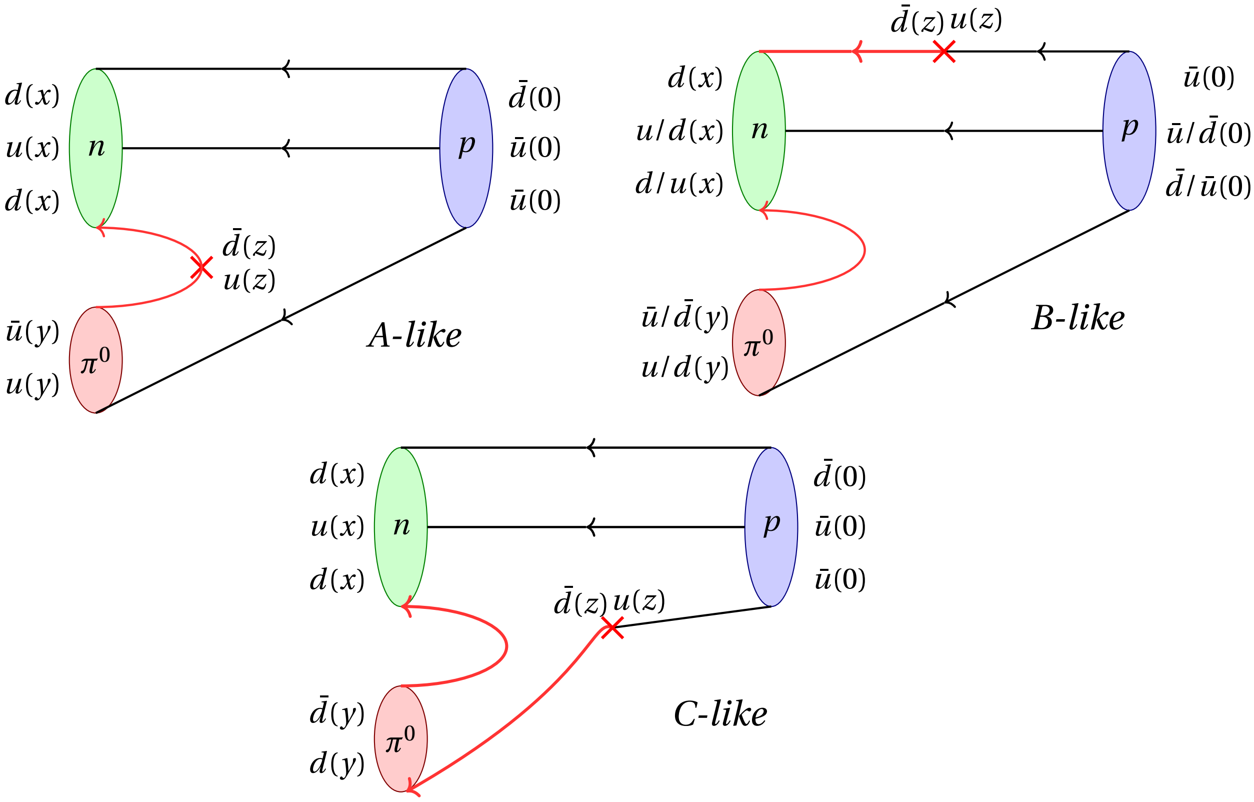

Figure 4.2:
These plots represent the topologies involved in the process $p + \mathscr{J}_{-} \to n + \pi^0$. Like in the other process, there are two all-to-all propagators for each diagram, which are marked with red lines. In this case, there is no disconnected piece, and therefore, they are all computed with the sequential method. Notice that for the diagram B, both u- and d- quark pieces of π^0 contribute.

an important role for the GEVP analysis because it is the term that has the largest signal and that is responsible for the contamination in the standard three-point functions. A closer look at the lower right sketch in Fig. 4.1 makes it clear that in the non-interacting case, it has the time-dependence $e^{-E_N t} e^{-E_\pi (t-\tau)}$, which was predicted by ChPT at leading order, see eqs. (2.44)-(2.45) in [27].

Furthermore, this diagram inherits the signal from the nucleon two-point functions and the meson-to-current two-point functions. Both terms are non-vanishing when the operators carry the same momentum. In the case of the meson-to-current two-point functions $\langle \mathrm{O}_\pi(\mathbf{p}'_\pi) \mathscr{J}_{-}(\mathbf{q}) \rangle$, the leading term in the spectral decomposition is proportional to the pion matrix elements $\langle \pi(\mathbf{p}'_\pi) | \mathscr{J}_{-}(\mathbf{q}) | \Omega \rangle$, which for $\mathscr{J} = \mathscr{A}^\mu$ read

$$\langle \pi(\mathbf{p}'_\pi) | \mathscr{A}^\mu(\mathbf{q}) | \Omega \rangle = i f_\pi q^\mu \delta_{\mathbf{p}'_\pi, \mathbf{q}} \,. \tag{4.21}$$

Notice that for $\mathscr{A}^z$, the matrix element does not vanish only if $q^z \neq 0$, while for $\mathscr{A}^4$ the correlation function does have a non-zero signal as long as $\mathbf{q} = \mathbf{p}'_\pi$, and similarly for $\mathscr{P}(\mathbf{q})$. This explains briefly why the $N\pi$ does not contaminate the standard three-point functions at LO-ChPT with $\mathscr{A}^z$, but are relevant in the $\mathscr{A}^4$ channel.

4.3 Nucleon-pion two-point functions

The nucleon-pion two-point functions are

$$C_{2pt}^{N\pi}(\mathbf{p}', t) = \langle \mathrm{O}_{N\pi}(\mathbf{p}', t)\ \bar{\mathrm{O}}_{N\pi}(\mathbf{p}, 0)\rangle \ , \tag{4.22}$$

where for the momentum conservation $\mathbf{p}' = \mathbf{p}$ and the nucleon-pion operators are defined by

$$\mathrm{O}_{N\pi}(\mathbf{p}', t) = \mathrm{O}_N(\mathbf{p}'_N, t)\mathrm{O}_\pi(\mathbf{p}'_\pi, t) \ , \qquad \bar{\mathrm{O}}_{N\pi}(\mathbf{p}, 0) = \bar{\mathrm{O}}_N(\mathbf{p}_N, 0)\bar{\mathrm{O}}_\pi(\mathbf{p}_\pi, 0) \ , \tag{4.23}$$

with $\mathbf{p}' = \mathbf{p}'_N + \mathbf{p}'_\pi$ and $\mathbf{p} = \mathbf{p}_N + \mathbf{p}_\pi$. The nucleon-pion operators both at the source and at the sink must be projected onto the desired isospin channel and lattice irreducible representation. In the case of the neutron channel, we must project on the proper isospin and spin/helicity, as explained in Sec. 4.1.

Regarding isospin projection, we use eq. 4.3 to obtain the nucleon-pion two-point function with $I = 1/2, I_z = -1/2$, i.e.

$$\begin{aligned} C_{2pt}^{N\pi}(\mathbf{p}'_N, \mathbf{p}'_\pi, t; \mathbf{p}_\pi, \mathbf{p}_N) \ =\ & + \frac{2}{3}\langle \mathrm{O}_p(\mathbf{p}'_N, t)\ \mathrm{O}_{\pi^-}(\mathbf{p}'_\pi, t)\ \mathrm{O}_{\pi^-}(\mathbf{p}_\pi, 0)\ \bar{\mathrm{O}}_p(\mathbf{p}_N, 0)\rangle + \\ & + \frac{1}{3}\langle \mathrm{O}_n(\mathbf{p}'_N, t)\ \mathrm{O}_{\pi^0}(\mathbf{p}'_\pi, t)\ \mathrm{O}_{\pi^0}(\mathbf{p}_\pi, 0)\ \bar{\mathrm{O}}_n(\mathbf{p}_N, 0)\rangle + \\ & - \frac{2\sqrt{2}}{3}\langle \mathrm{O}_n(\mathbf{p}'_N, t)\ \mathrm{O}_{\pi^0}(\mathbf{p}'_\pi, t)\ \mathrm{O}_{\pi^-}(\mathbf{p}_\pi, 0)\ \bar{\mathrm{O}}_p(\mathbf{p}_N, 0)\rangle \ . \end{aligned} \tag{4.24}$$

The nucleon-pion two-point functions are computed using the nucleon to nucleon-pion three-point functions at different source-sink separations. Indeed, the latter are computed by fixing the nucleon-pion operators at the sink t and by varying the interaction time τ of the current.

A further look at the diagrams in Figs. 4.1-4.2 and it makes it clear that in the particular case of a pseudoscalar current ($\Gamma = \gamma^5$)

$$\mathscr{J}_-(\mathbf{z}_0) = \mathscr{P}_-(\mathbf{z}_0) = \bar{d}(\mathbf{z}_0)\gamma^5 u(\mathbf{z}_0) \ = -\bar{\mathrm{O}}_{\pi^-}(z_0) \ , \tag{4.25}$$

with $\mathbf{z}_0 = (\mathbf{z}, \tau = 0)$, so when the intermediate current is at the source, the three-point functions correspond to a nucleon-pion two-point functions evaluated at a source-sink separation t.

In particular,

$$C_{2pt}^{p\pi^- \to p\pi^-}(\mathbf{p}'_N, \mathbf{p}'_\pi, t; \mathbf{p}_\pi, \mathbf{p}_N) = -\langle\ \mathrm{O}_p(\mathbf{p}'_N, t)\ \mathrm{O}_{\pi^-}(\mathbf{p}'_\pi, t)\ \mathscr{P}_-(\mathbf{q}, \tau = 0)\ \bar{\mathrm{O}}_p(\mathbf{p}_N, 0)\ \rangle \ , \tag{4.26}$$

where the minus sign is due to the antisymmetric properties of the quarks, see eq. (4.25). Here I list the various relations that occur between nucleon-pion two-point functions and nucleon to nucleon-pion three-point functions:

$$C_{2pt}^{p\pi^-\to n\pi^0}(\mathbf{p}'_N,\mathbf{p}'_\pi,\mathbf{p}_\pi;t) = -C_{3pt}^{p\mathscr{P}_-\to p\pi^-}(\mathbf{p}'_N,\mathbf{p}'_\pi,\mathbf{q}=\mathbf{p}_\pi;t,\tau=0)\,, \tag{4.27}$$

$$C_{2pt}^{p\pi^-\to n\pi^0}(\mathbf{p}'_N,\mathbf{p}'_\pi,\mathbf{p}_\pi,t) = -C_{3pt}^{p\mathscr{P}_0\to n\pi^0}(\mathbf{p}'_N,\mathbf{p}'_\pi,\mathbf{q}=\mathbf{p}_\pi;t,\tau=0)\,, \tag{4.28}$$

$$C_{2pt}^{n\pi^0\to n\pi^0}(\mathbf{p}'_N,\mathbf{p}'_\pi,\mathbf{p}_\pi,t) = -C_{3pt}^{n\mathscr{P}_0\to n\pi^0}(\mathbf{p}'_N,\mathbf{p}'_\pi,\mathbf{q}=\mathbf{p}_\pi;t,\tau=0)\,, \tag{4.29}$$

$$C_{2pt}^{n\to p\pi^-}(\mathbf{p}'_N,\mathbf{p}'_\pi,t) = -C_{3pt}^{n\mathscr{P}_-\to p}(\mathbf{p}'_N,\mathbf{q}=-\mathbf{p}'_\pi;t,\tau=t)\,, \tag{4.30}$$

$$C_{2pt}^{p\pi^-\to n}(\mathbf{p}'_N,\mathbf{p}'_\pi,t) = -C_{3pt}^{p\mathscr{P}_-\to n}(\mathbf{p}'_N,\mathbf{q}=\mathbf{p}'_\pi;t,\tau=0) = -C_{3pt}^{n\mathscr{P}_-\to p}(\mathbf{p}'_N,\mathbf{q}=\mathbf{p}'_\pi;t,\tau=0)\,. \tag{4.31}$$

Notice that the pion momentum at the sink for the two-point $C_{2pt}^{n\to p\pi^-}$ is the opposite with respect to the nucleon three-point function, and the three-point functions should be evaluated at the sink $\tau = t$. A significant relation that can be proven with the Wigner Eckart theorem is

$$C_{2pt}^{n\to n\pi^0}(\mathbf{p}'_N,\mathbf{p}'_\pi,t) = \frac{1}{\sqrt{2}}\,C_{2pt}^{n\to p\pi^-}(\mathbf{p}'_N,\mathbf{p}'_\pi,t)\,, \tag{4.32}$$

which can be found, for instance, in [46], where the relations are generalized to the baryon octet. Other important relations exist between the matrix elements $\langle N\pi|\mathscr{J}|N\rangle$. These can be proven with the Wigner-Eckart theorem, checked on the lattice, and they are explained in the next section.

4.4 The Wigner-Eckart theorem

The Wigner-Eckart theorem played an important role in this project because it provided helpful checks for the calculations. It states that matrix elements of spherical tensor operators in the basis of angular momentum - or like in this case isospin eigenstates - can be expressed as the product of two factors, one of which is independent of the isospin orientation I_z, and the other a Clebsch–Gordan coefficient.

The Wigner–Eckart theorem is generally stated in the following way. Given a tensor operator $T^{(k)}$ and two isospin eigenstates $|I, I_z\rangle$, $|I', I'_z\rangle$, there exists a constant $\langle I'|\, T^{(k)}\, |I\rangle$, such that for all I_z, I'_z and I_q, the following equation is satisfied:

$$\langle I'\, I'_z|T_q^{(k)}|I\, I_z\rangle = \langle I\, I_z; k\, q|I'\, I'_z\rangle\langle I'\|\, T^{(k)}\|I\rangle\,, \tag{4.33}$$

where

- $T_q^{(k)}$ is the q-th component of the spherical tensor operator $T^{(k)}$ of rank k;

- $|I I_z\rangle$ denotes an eigenstate isospin I^2 and its z component I_z;
- $\langle I\, I_z; k\, q | I'\, I'_z\rangle$ is the Clebsch-Gordan coefficient for coupling I with k to get I';
- $\langle I' \| T^{(k)} \| I\rangle$ is the reduced matrix element, which does not depend on I_z, I'_z, nor on q.

If we identify the particles with isospin $I_N = 1/2$ as nucleons and $I_\pi = 1$ as pions, see App. B, we find a relation between scattering amplitudes S of different processes. In particular, the addition of isospin eigenstates $I_N \oplus I_\pi$ gives

$$|\pi^+ p\rangle = \left|1,+1;\frac{1}{2},+\frac{1}{2}\right\rangle = \left|\frac{3}{2},+\frac{1}{2}\right\rangle , \tag{4.34}$$

$$|\pi^+ n\rangle = \left|1,+1;\frac{1}{2},-\frac{1}{2}\right\rangle = \frac{1}{\sqrt{3}}\left|\frac{3}{2},+\frac{1}{2}\right\rangle + \sqrt{\frac{2}{3}}\left|\frac{1}{2},+\frac{1}{2}\right\rangle , \tag{4.35}$$

$$|\pi^0 p\rangle = \left|1,0;\frac{1}{2},+\frac{1}{2}\right\rangle = \sqrt{\frac{2}{3}}\left|\frac{3}{2},+\frac{1}{2}\right\rangle - \frac{1}{\sqrt{3}}\left|\frac{1}{2},+\frac{1}{2}\right\rangle , \tag{4.36}$$

$$|\pi^0 n\rangle = \left|1,0;\frac{1}{2},-\frac{1}{2}\right\rangle = \sqrt{\frac{2}{3}}\left|\frac{3}{2},-\frac{1}{2}\right\rangle + \frac{1}{\sqrt{3}}\left|\frac{1}{2},-\frac{1}{2}\right\rangle , \tag{4.37}$$

$$|\pi^- p\rangle = \left|1,-1;\frac{1}{2},+\frac{1}{2}\right\rangle = \frac{1}{\sqrt{3}}\left|\frac{3}{2},-\frac{1}{2}\right\rangle - \sqrt{\frac{2}{3}}\left|\frac{1}{2},-\frac{1}{2}\right\rangle , \tag{4.38}$$

$$|\pi^- n\rangle = \left|1,-1;\frac{1}{2},-\frac{1}{2}\right\rangle = \left|\frac{3}{2},-\frac{1}{2}\right\rangle . \tag{4.39}$$

Notice first, that from eqs. (4.37)-(4.38) we recover eq. (4.3) for nucleon-pion states, that is

$$\left|\frac{1}{2},-\frac{1}{2}\right\rangle = +\frac{1}{\sqrt{3}}|\pi^0 n\rangle - \sqrt{\frac{2}{3}}|\pi^- p\rangle . \tag{4.40}$$

Consider now the scattering operator S between incoming and outgoing states. Since it commutes with the isospin rotations I_i, it follows that the diagonal matrix elements $\langle I, I_z | S | I, I_z\rangle$ are independent of I_z, while the non-diagonal elements vanish. Therefore, it makes sense to define the reduced scattering amplitude S^I of a given isospin I by the equation

$$\langle I, I'_z | S | I, I_z\rangle = \delta_{I'_z I_z}\, S^I , \tag{4.41}$$

which is a special case of the Wigner-Eckart theorem mentioned above.

The eq. (4.41) has important applications as it relates the scattering amplitudes of various pion-nucleon scattering processes:

$$S_{p\pi^+\to p\pi^+} = S_{n\pi^-\to n\pi^-} = S^{3/2}\,, \tag{4.42}$$

$$S_{n\pi^+\to n\pi^+} = S_{p\pi^-\to p\pi^-} = \frac{1}{3}\,S^{3/2} + \frac{2}{3}\,S^{1/2}\,, \tag{4.43}$$

$$S_{p\pi^0\to p\pi^0} = S_{n\pi^0\to n\pi^0} = \frac{2}{3}\,S^{3/2} + \frac{1}{3}\,S^{1/2}\,, \tag{4.44}$$

$$S_{n\pi^+\leftrightarrow p\pi^0} = S_{n\pi^0\leftrightarrow p\pi^-} = \frac{\sqrt{2}}{3}\,S^{3/2} - \frac{\sqrt{2}}{3}\,S^{1/2}\,. \tag{4.45}$$

By taking the absolute squares of the amplitudes, we obtain relations between cross sections σ that are verified by experiments, for example

$$2\sigma_{p\pi^0\to p\pi^0} = \sigma_{p\pi^+\to p\pi^+} + \sigma_{p\pi^-\to p\pi^-}\,. \tag{4.46}$$

Another important relation that can be derived from the expressions mentioned above is

$$S_{n\pi^0\to n\pi^0} \;=\; S_{p\pi^-\to p\pi^-} + \frac{1}{\sqrt{2}} S_{p\pi^-\to n\pi^0}\,, \tag{4.47}$$

which we checked on the lattice and it is satisfied also between two-point correlation functions:

$$C_{2pt}^{n\pi^0\to n\pi^0}(t) \;=\; C_{2pt}^{p\pi^-\to p\pi^-}(t) + \frac{1}{\sqrt{2}} C_{2pt}^{p\pi^-\to n\pi^0}(t) \tag{4.48}$$

and three-point functions, like for example

$$C_{3pt}^{n\mathcal{J}_{\pi^0}\to n\pi^0}(t) \;=\; C_{3pt}^{p\mathcal{J}_{\pi^-}\to p\pi^-}(t) + \frac{1}{\sqrt{2}} C_{2pt}^{p\mathcal{J}_{\pi^-}\to n\pi^0}(t)\,, \tag{4.49}$$

where $\mathcal{J}_{\pi^0} = \frac{1}{\sqrt{2}}(\bar{u}\Gamma u - \bar{d}\Gamma d) = \frac{1}{\sqrt{2}}\mathcal{J}_3$. These isospin relations in eqs. (4.48), (4.49) were checked for the first time in this work on a single ensemble.

4.5 GEVP analysis of two-point functions

In Chap. 3, we discussed how to extract nucleon eigenenergies E_N, vacuum to physical states matrix elements of nucleon operators $\langle\Omega|\mathrm{O}_N|N\rangle$ from the nucleon two-point functions and nucleon matrix elements of intermediate currents $\langle N|\mathcal{J}|N\rangle$ through a suitable ratio of three- and two-point functions.

With the nucleon-to-nucleon-pion three-point and nucleon-pion two-point functions, we aim to extract $E_{N\pi}$, $\langle\Omega|\mathrm{O}_N|N\pi\rangle$, $\langle\Omega|\mathrm{O}_{N\pi}|N\rangle$, $\langle\Omega|\mathrm{O}_{N\pi}|N\pi\rangle$ and finally $\langle N\pi|\mathcal{J}|N\rangle$, with $\mathcal{J} \in \{\mathcal{P},\mathcal{A}^\mu\}$.

If we project the nucleon-pion interpolators to have the same quantum numbers as the nucleon $|N\rangle$, the spectral decomposition of the nucleon-pion two-point functions in eq. (4.22) gives

$$\begin{aligned}C^{N\pi}_{2pt}(t) &= \langle \mathrm{O}_{N\pi}(\mathbf{p},t)\,\bar{\mathrm{O}}_{N\pi}(\mathbf{p},0)\rangle \\ &= \frac{e^{-E_N t}}{2E_N}\langle\Omega|\mathrm{O}_{N\pi}(\mathbf{p})|N\rangle\,\langle N|\bar{\mathrm{O}}_{N\pi}(\mathbf{p})|\Omega\rangle + \frac{e^{-E_{N\pi\pi}t}}{2E_{N\pi\pi}}\langle\Omega|\mathrm{O}_{N\pi}(\mathbf{p})|N\pi\pi\rangle\,\langle N\pi\pi|\bar{\mathrm{O}}_{N\pi}(\mathbf{p})|\Omega\rangle + \\ &+ \frac{e^{-E_{N\pi}t}}{2E_{N\pi}}\langle\Omega|\mathrm{O}_{N\pi}(\mathbf{p})|N\pi\rangle\,\langle N\pi|\bar{\mathrm{O}}_{N\pi}(\mathbf{p})|\Omega\rangle + \frac{e^{-E_{N^*}t}}{2E^*_N}\left\langle\Omega\middle|\mathrm{O}_{N\pi}(\mathbf{p})\middle|N^*\right\rangle\left\langle N^*\middle|\bar{\mathrm{O}}_{N\pi}(\mathbf{p})\middle|\Omega\right\rangle + \ldots\end{aligned}$$

and we would expect that at large t, it is still the nucleon to dominate the correlation functions, as it has the lowest energy E_N. Therefore, extracting the $N\pi$ states from these correlation functions seems difficult, but there is a strategy to overcome this issue.

At a conference in 1981, K. Wilson proposed the variational method [145], a technique that can be adopted to compute energy levels in lattice gauge theory. The idea had a lot of applications, and it was immediately used to determine the glueball spectrum [39, 123] and the static quark potential [55]. Today, this method is still used and applied to the hadron spectrum as well. In particular, in [110], Lüscher and Wolff show how to use it to determine also excited states, like in our case $|N\pi\rangle$. The idea is to construct a large basis $\mathbb{B}$ of interpolating operators that couple to our states of interest, that is

$$\mathbb{B} = \{\mathrm{O}_1, \mathrm{O}_2, \ldots, \mathrm{O}_m\}\,, \tag{4.50}$$

where O_k represents a generic interpolating operator that couples to the nucleon. With this basis, one can construct a matrix of correlation functions like

$$\mathscr{C}_{2pt}(\mathbf{p},t)_{ij} = \langle \mathrm{O}_i(\mathbf{p},t)\,\bar{\mathrm{O}}_j(\mathbf{p},0)\rangle = \sum_{n=1} e^{-E_n t}\,\langle\Omega|\,\mathrm{O}_i(\mathbf{p},t)\,|n\rangle\,\langle n|\,\bar{\mathrm{O}}_j(\mathbf{p},0)\,|\Omega\rangle\;, \tag{4.51}$$

with $i, j = 1, 2, \ldots, m$ and $n = 1, ..., \infty$ represent the tower of states with the same quantum numbers as O_i and $\bar{\mathrm{O}}_j$. The matrix representation of eq. (4.51) on the l.h.s. is

$$\mathscr{C}_{2pt}(\mathbf{p},t) = \begin{pmatrix} \langle\,\mathrm{O}_1(\mathbf{p},t)\,\bar{\mathrm{O}}_1(\mathbf{p},0)\,\rangle & \langle\,\mathrm{O}_1(\mathbf{p},t)\,\bar{\mathrm{O}}_2(\mathbf{p},0)\,\rangle & \cdots & \langle\,\mathrm{O}_1(\mathbf{p},t)\,\bar{\mathrm{O}}_m(\mathbf{p},0)\,\rangle \\ \langle\,\mathrm{O}_2(\mathbf{p},t)\,\bar{\mathrm{O}}_1(\mathbf{p},0)\,\rangle & \langle\,\mathrm{O}_2(\mathbf{p},t)\,\bar{\mathrm{O}}_2(\mathbf{p},0)\,\rangle & \cdots & \langle\,\mathrm{O}_2(\mathbf{p},t)\,\bar{\mathrm{O}}_m(\mathbf{p},0)\,\rangle \\ \cdots & \cdots & \cdots & \cdots \\ \langle\,\mathrm{O}_m(\mathbf{p},t)\,\bar{\mathrm{O}}_1(\mathbf{p},0)\,\rangle & \langle\,\mathrm{O}_m(\mathbf{p},t)\,\bar{\mathrm{O}}_2(\mathbf{p},0)\,\rangle & \cdots & \langle\,\mathrm{O}_m(\mathbf{p},t)\,\bar{\mathrm{O}}_m(\mathbf{p},0)\,\rangle \end{pmatrix}. \tag{4.52}$$

We truncate the sum on the r.h.s. in eq. (4.51) at $n = m$, so that

$$\mathscr{C}_{2pt}(\mathbf{p},t)_{ij} = \sum_{n=1}^{m} \mathbb{Z}_{in}\mathbb{Z}^{\mathsf{T}}_{nj}\,e^{-E_n t}\,\left[1 + \mathscr{O}(e^{-(E_m-E_n)t})\right]\,, \tag{4.53}$$

where for shorthand notation we define

$$\mathbb{Z}_{in} = \frac{1}{\sqrt{2E_n V}} \langle \psi_i | n \rangle \ , \qquad \mathbb{Z}^{\mathsf{T}}_{nj} = \frac{1}{\sqrt{2E_n V}} \langle n | \psi_j \rangle \ , \qquad |\psi_j\rangle = \bar{\mathrm{O}}_j \, |\Omega\rangle \tag{4.54}$$

and it is clear from eq. (4.53) that $\mathbb{Z}_{in} \approx e^{+E_n t} \sum_{j=1}^{m} \mathscr{C}_{2pt}(\mathbf{p}, t)_{ij} \ \mathbb{Z}^{-1}_{jn}$. With this definition, we can solve the system

$$\mathscr{C}_{2pt}(\mathbf{p}, t) V(\mathbf{p}, t, t_0) = \Lambda(\mathbf{p}, t, t_0) \ \mathscr{C}_{2pt}(\mathbf{p}, t_0)_{ij} V(\mathbf{p}, t, t_0) \ , \qquad t > t_0 \ , \tag{4.55}$$

which is called Generalized EigenValue Problem (GEVP hereafter) for the matrix $\mathscr{C}_{2pt}(\mathbf{p}, t)$. The objects $V(\mathbf{p}, t, t_0) = \big(v_1(\mathbf{p}, t, t_0), \ldots, v_m(\mathbf{p}, t, t_0)\big)$ and $\Lambda(\mathbf{p}, t, t_0) = \big(\lambda_1(\mathbf{p}, t, t_0), \ldots, \lambda_m(\mathbf{p}, t, t_0)\big)$ are respectively the matrix of generalized eigenvectors v_n and eigenvalues λ_n, at a reference time t_0 and in the frame p. The usefulness of this strategy is that after solving eq. (4.55), we can extract the n-th eigenenergy from the n-th eigenvalue, i.e.

$$\lambda_n(\mathbf{p}, t, t_0) \approx d_n(t_0) e^{-E_n(t - t_0)} \ . \tag{4.56}$$

The eigenvectors are orthogonal with respect to $C_{2pt}(\mathbf{p}, t_0)$ at each t, which means that

$$\Big(v^{\alpha}(\mathbf{p}, t), \ \mathscr{C}_{2pt}(\mathbf{p}, t_0) v^{\beta}(\mathbf{p}, t)\Big) \propto \delta^{\alpha\beta} \ , \tag{4.57}$$

where we define the inner product of a matrix A with the eigenvectors as

$$\Big(v^{\alpha}(\mathbf{p}_\alpha, t_\alpha), \ A v^{\beta}(\mathbf{p}_\beta, t_\beta)\Big) := \sum_{i,j} v^{\alpha}_i(\mathbf{p}_\alpha, t_\alpha, t_0) \ A^{ij} \, v^{\beta}_j(\mathbf{p}_\beta, t_\beta, t_0) \ , \tag{4.58}$$

and we normalise them such that they are orthonormal with respect to $\mathscr{C}_{2pt}(\mathbf{p}, t_0)$, i.e.

$$\Big(v^{\alpha}(\mathbf{p}, t), \ \mathscr{C}_{2pt}(\mathbf{p}, t_0) v^{\beta}(\mathbf{p}, t)\Big) = \delta^{\alpha\beta} \ . \tag{4.59}$$

This strategy is beneficial for determining the energy spectrum of particles, but the basis of interpolating operators $\mathbb{B}$ should be chosen carefully and as large as possible. One way to extend the number of interpolating operators so that they are all consistent with the quantum numbers, is to employ smearing techniques at different levels, i.e. different smearing radii r_n (see eq. (2.93)). This way, one can start from a single interpolating operator O_1, and by using different smearing radii it is possible to form a second one $\mathrm{O}_2 = \Phi_{r_2}\mathrm{O}_1$, a third one $\mathrm{O}_3 = \Phi_{r_3}\mathrm{O}_1$, et cetera We solve the GEVP using the following rank-2 bases: $B_1 = \{\mathrm{O}_N, \Phi\mathrm{O}_N\}$, $B_2 = \{\mathrm{O}_N, \mathrm{O}_{N\pi}\}$, $B_3 = \{\Phi\mathrm{O}_N, \mathrm{O}_{N\pi}\}$, $B_4 = \{\Phi\mathrm{O}_N, \Phi\mathrm{O}_{N\pi}\}$, and in Fig. 4.3, we present the GEVP results with the basis B_4 in the rest frame ($\mathbf{p} = \mathbf{0}$) and one moving frame ($\mathbf{p} = \hat{e}_i$). Recall from eqs. (4.6)-(4.7) that there are two nucleon-pion operators with the same quantum numbers and non-zero total momentum $\mathbf{p}$. One operator is such that the pion is at rest; see eq. (4.6), and the other one is where the nucleon is at rest, see eq. (4.7). In the next and final chapter, I will discuss how these GEVP results can be adopted to construct improved operators. Finally, I will give results on the extraction of GEVP-improved matrix elements.

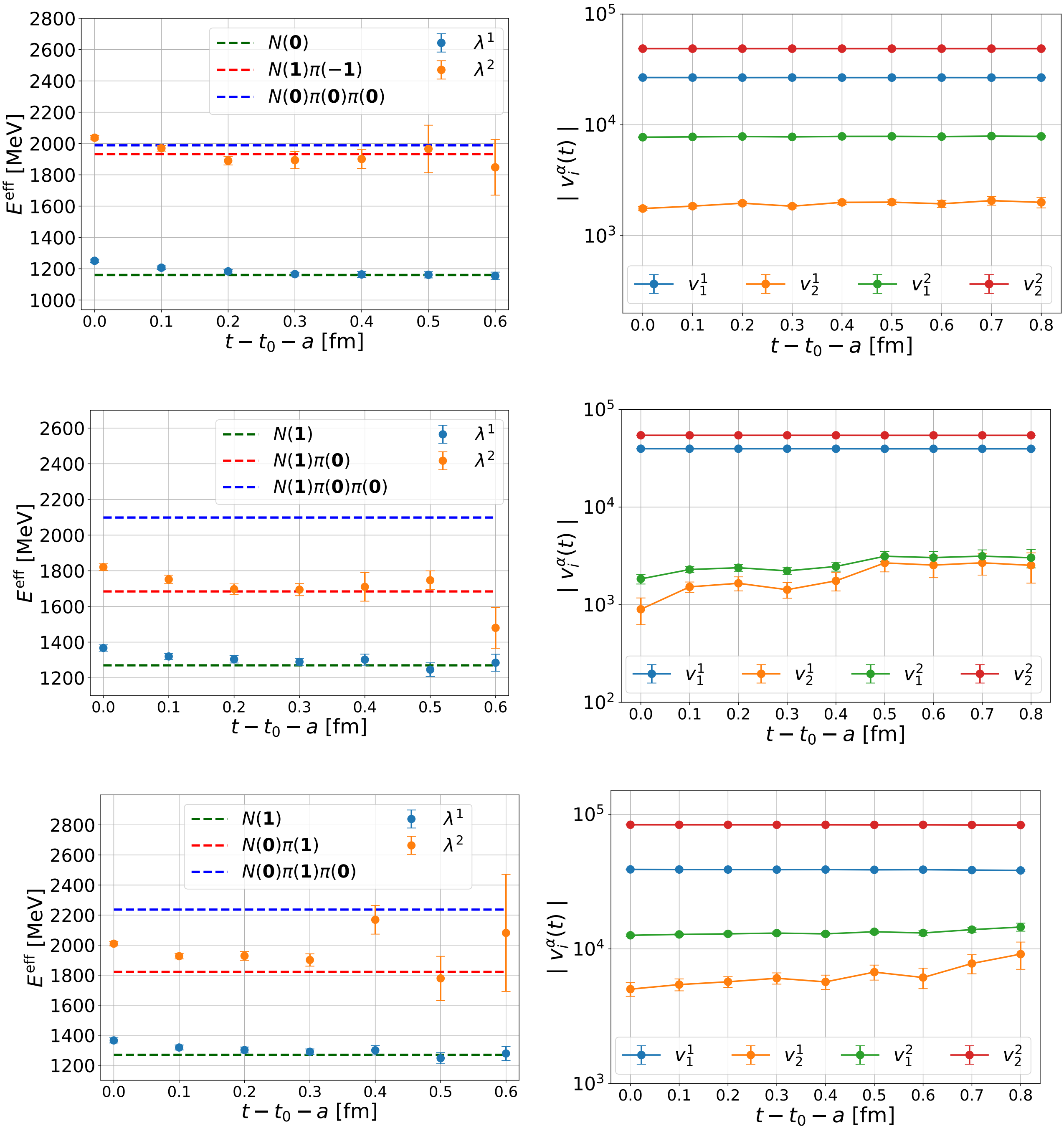

Figure 4.3:
In this figure, we present the GEVP solutions of eq. (4.55) with $t_0 = 0.2$ fm, and with the basis $\mathbb{B}_4 = \{\Phi O_N, \Phi O_{N\pi}\}$. We use the shorthand notation $\lambda^\alpha \equiv \lambda^\alpha(\mathbf{p} = \mathbf{0}, t, t_0 = 0.2 \text{ fm})$ and $v_i^\alpha \equiv v_i^\alpha(\mathbf{p} = \mathbf{0}, t, t_0 = 0.2 \text{ fm})$. On the left plots, we display the effective energies of the eigenvalues λ^1 and λ^2, that are computed with eq. (4.56), and we compare them to the energy of the nucleon at rest and the non-interacting energies of $N\pi$ S-wave and $N\pi\pi$ P-wave. On the right plots, each component of the eigenvectors is plotted in function of t. The plots in the uppermost row are the GEVP solutions with $\mathbf{p} = \mathbf{0}$ and the ones in the middle row are with the nucleon-pion operators in eq. (4.6) and total momentum $\mathbf{p} = \hat{e}_i$, while the lowermost plots are with the operators in eq. (4.7) and total momentum $\mathbf{p} = \hat{e}_i$.

CHAPTER
FIVE

RESULTS

In this chapter, we apply the GEVP-projection method discussed in Sec. 4.5 to construct operators that have better overlap with the physical state of interest. In particular, we show that the same eigenvectors can be adopted for the three-point functions such that it is possible to construct a GEVP-improved version of the standard ratio constructed in eq. (3.45).

5.1 Summary of the variational method employed

In principle, there is a tower of excited states with the same quantum numbers as the nucleon, namely $N\pi$, $N^*(1440)$, $N\pi\pi$, ..., which can be created by the nucleon operator O_N. However, let us suppose that the nucleon operator O_N creates only two states: the ground state and the first excited state, which for convenience, we call $|N\rangle$ and $|N\pi\rangle$. This translates into

$$\mathrm{O}_N\,|\Omega\rangle = c_1\,|N\rangle + c_2\,|N\pi\rangle\; + \ldots \tag{5.1}$$

where the ellipses represent higher excited states that we neglect here. Ideally, we would like to have that O_N creates only $|N\rangle$, but we can construct an operator that has a very good overlap with the first excited state and diagonalise the system in eq. (5.1). This operator is $\mathrm{O}_{N\pi}$. We construct a matrix of two-point functions that for this simplistic case it reads

$$\mathscr{C}_{2pt}(t) = \begin{pmatrix} \langle\, \mathrm{O}_N(t)\; \bar{\mathrm{O}}_N(0)\,\rangle & \langle\, \mathrm{O}_N(t)\; \bar{\mathrm{O}}_{N\pi}(0)\,\rangle \\ \langle\, \mathrm{O}_{N\pi}(t)\; \bar{\mathrm{O}}_N(0)\,\rangle & \langle\, \mathrm{O}_{N\pi}(t)\; \bar{\mathrm{O}}_{N\pi}(0)\,\rangle \end{pmatrix}\,. \tag{5.2}$$

Using this matrix, we solve the GEVP in eq. (4.55) and we extract the eigenvectors $v^N(t)$ and $v^{N\pi}(t)$, which are needed to construct operators O'_N and $\mathrm{O}'_{N\pi}$ that have better overlap with the physical states $|N\rangle$ and $|N\pi\rangle$, i.e.

$$\mathrm{O}'_N\,|\Omega\rangle = c'_N\,|N\rangle\; + \ldots \tag{5.3}$$

$$\mathrm{O}'_{N\pi}\,|\Omega\rangle = c'_{N\pi}\,|N\pi\rangle\; + \ldots. \tag{5.4}$$

With these GEVP-improved operators, we can construct ratios of three-point correlation functions and two-point correlation functions, with the aim to extract GEVP-improved matrix elements. This will be discussed in the following sections in more detail, where I will also present results for the GEVP-improved matrix elements.

5.2 GEVP improvement for matrix elements

It has been discussed in e.g. [38, 51] that solving the GEVP is helpful for extracting matrix elements more effectively.

We can use the GEVP results discussed in Sec. 4.5 and, in particular, the orthonormality properties of the eigenvectors, see eq. (4.59), to construct operators O_i that have better overlap with a desired state. The GEVP-improved two-point functions that have better overlap with the state α are constructed in the following way:

$$\mathscr{C}_{2pt}(\mathbf{p},t)^{\alpha} := \left(v^{\alpha}(\mathbf{p},t,t_0),\, \mathscr{C}_{2pt}(\mathbf{p},t)\, v^{\alpha}(\mathbf{p},t,t_0)\right) \,, \tag{5.5}$$

while the three-point correlation functions projected at the sink on α and at the source on β are

$$\mathscr{C}_{3pt}^{\mathbb{P}^j,\mathscr{J}}(\mathbf{p}',t;\mathbf{q},\tau)^{\alpha\beta} := \Big(v^{\alpha}(\mathbf{p},t,t_0),\, \mathscr{C}_{3pt}^{\mathbb{P}^j,\mathscr{J}}(\mathbf{p}',t;\mathbf{q},\tau)\, v^{\beta}(\mathbf{p},t,t_0)\Big) \,. \tag{5.6}$$

In eq. (5.5), $\mathscr{C}_{2pt}$ is the matrix of two-point functions defined in eq. (4.51) and $\mathscr{C}_{3pt}$ is the matrix of three-point functions that reads

$$\mathscr{C}_{3pt}^{\mathbb{P}^j,\mathscr{J}}(\mathbf{p}',t;\mathbf{q},\tau)_{ij} = \mathbb{P}^j \left\langle \mathrm{O}_i(\mathbf{p}',t)\; \mathscr{J}(\mathbf{q},\tau)\; \bar{\mathrm{O}}_j(\mathbf{p},0)\right\rangle \,. \tag{5.7}$$

Using these improved correlation functions, it is possible to compute GEVP-improved matrix elements of the current $\mathscr{J}$ between two states α and β, i.e. $\langle \alpha(\mathbf{p}')|\, \mathscr{J}(\mathbf{q})\, |\beta(\mathbf{p})\rangle$.

In the symmetric case where $\alpha = \beta = N$, this suitable ratio takes an expression similar to eq. (3.45), with the difference that we use projected correlation functions. Therefore, the GEVP ratio reads

$$\frac{\mathscr{C}_{3pt}^{\mathscr{J}}(\mathbf{p}',t;\mathbf{q},\tau)^{NN}}{\mathscr{C}_{2pt}(\mathbf{p}',t)^{N}} \sqrt{\frac{\mathscr{C}_{2pt}(\mathbf{p}',\tau)^{N}\mathscr{C}_{2pt}(\mathbf{p}',t)^{N}\mathscr{C}_{2pt}(\mathbf{p},t-\tau)^{N}}{\mathscr{C}_{2pt}(\mathbf{p},\tau)^{N}\mathscr{C}_{2pt}(\mathbf{p},t)^{N}\mathscr{C}_{2pt}(\mathbf{p}',t-\tau)^{N}}} \longrightarrow \langle N(\mathbf{p}')|\, \mathscr{J}(\mathbf{q})\, |N(\mathbf{p})\rangle \,. \tag{5.8}$$

This GEVP-projected ratio actually provides a linear combination of nucleon form factors as discussed in Sec. 3.4, which stems from the Lorentz decomposition of the nucleon matrix elements. In [130], the authors construct a set of single-particle nucleon interpolating operators with different levels of smearing and extract the axial charge g_A from a suitable ratio GEVP-improved correlation functions. They compare the results with the standard ratios of nucleon three-point functions discussed in Sec. 3.7.

In this project, we include the nucleon-pion operators in the GEVP analysis, as there is evidence that the $N\pi$ states are the major source of contamination to the extraction of the matrix elements $\langle N|\mathscr{P}|N\rangle$ and $\langle N|\mathscr{A}_\mu|N\rangle$, at least at non-zero momentum transfer.

For the projection of the interpolating operators, a careful choice of t_1 and t_2, which appear in the construction, must be made for the eigenvectors, see eqs. (5.5)-(5.6). However, in our case, the eigenvectors we extract are reasonably constant with t.

This choice of t_1 and t_2 is made such that the effective energies of the eigenvalues have a plateau on the desired state (N, $N\pi$).

5.3 Nucleon matrix elements with $\mathbf{q} = \mathbf{0}$

In the special case where $\mathbf{q} = \mathbf{0}$, the GEVP-improved ratio in eq. (5.8) takes the expression

$$\left\langle N(\mathbf{p}')\right|\, \mathscr{J}(\mathbf{0})\, \left|N(\mathbf{p}')\right\rangle = \frac{\mathscr{C}^{\mathscr{J}}_{3pt}(\mathbf{p}', t; \mathbf{0}, \tau)^{NN}}{\mathscr{C}_{2pt}(\mathbf{p}', t)^{N}} \,. \tag{5.9}$$

In particular, the GEVP-improved versions of the standard ratios in eqs. (3.72), (3.73) and (3.75) are

$$R_1^{(\mathrm{GEVP})} := \frac{\mathscr{C}^{\mathscr{A}_j}_{3pt}(\hat{e}_j, t; \mathbf{0}, \tau)^{NN}}{\mathscr{C}_{2pt}(\hat{e}_j, t)^{N}} = \frac{(v^N(\hat{e}_j, t_2),\, \mathscr{C}^{\mathbb{P}_j, \mathscr{A}_j}_{3pt}(\hat{e}_j, t; \mathbf{0}, \tau)\, v^N(\hat{e}_j, t_1))}{(v^N(\hat{e}_j, t_2),\, \mathscr{C}_{2pt}(\hat{e}_j, t)\, v^N(\hat{e}_j, t_1))} \,, \tag{5.10}$$

$$R_2^{(\mathrm{GEVP})} := \frac{\mathscr{C}^{\mathscr{A}_4}_{3pt}(\hat{e}_j, t; \mathbf{0}, \tau)^{NN}}{\mathscr{C}_{2pt}(\hat{e}_j, t)^{N}} = \frac{(v^N(\hat{e}_j, t_2),\, \mathscr{C}^{\mathbb{P}_j, \mathscr{A}_4}_{3pt}(\hat{e}_j, t; \mathbf{0}, \tau)\, v^N(\hat{e}_j, t_1))}{(v^N(\hat{e}_j, t_2),\, \mathscr{C}_{2pt}(\hat{e}_j, t)\, v^N(\hat{e}_j, t_1))} \,, \tag{5.11}$$

$$R_3^{(\mathrm{GEVP})} := \frac{\mathscr{C}^{\mathscr{P}}_{3pt}(\hat{e}_j, t; \mathbf{0}, \tau)^{NN}}{\mathscr{C}_{2pt}(\hat{e}_j, t)^{N}} = \frac{(v^N(\hat{e}_j, t_2),\, \mathscr{C}^{\mathbb{P}_j, \mathscr{P}}_{3pt}(\hat{e}_j, t; \mathbf{0}, \tau)\, v^N(\hat{e}_j, t_1))}{(v^N(\hat{e}_j, t_2),\, \mathscr{C}_{2pt}(\hat{e}_j, t)\, v^N(\hat{e}_j, t_1))} \,, \tag{5.12}$$

where I write explicitly the dependence on t_1 and t_2 for more clarity, and the inner product of eigenvectors and matrix of correlation functions is defined in eq. (4.58).

Notice that we do not compute the three-point functions with nucleon-pion operators both at source and sink, i.e. we neglect the term

$$C_{3pt}^{N\pi\to N\pi}(\mathbf{p}', t; \mathbf{q}, \tau) \;=\; \left\langle \mathrm{O}_{N\pi}(\mathbf{p}', t)\; \mathscr{J}(\mathbf{q}, \tau)\; \mathrm{O}_{N\pi}(\mathbf{p}, 0)\right\rangle \,. \tag{5.13}$$

This approximation is motivated by ChPT, according to which the dominant contribution is due to $N\pi$ states produced either at the source or at the sink, see refs. [27, 100].

The GEVP eigenvectors $v_N(\hat{e}_j, t)$ are the ones where the nucleon-pion system has total momentum $\hat{e}_j$ and it is in the momentum configuration $N(\hat{e}_j)\pi(\mathbf{0})$, i.e. we solve the GEVP with the nucleon-pion operators in eqs. (4.6). In Fig. 5.1, we present the comparison plots between the GEVP-improved ratios R_1, R_2 and R_3 in eqs. (5.10), (5.11), (5.12) and the standard ratio in eqs. (3.72), (3.73), (3.75), respectively.

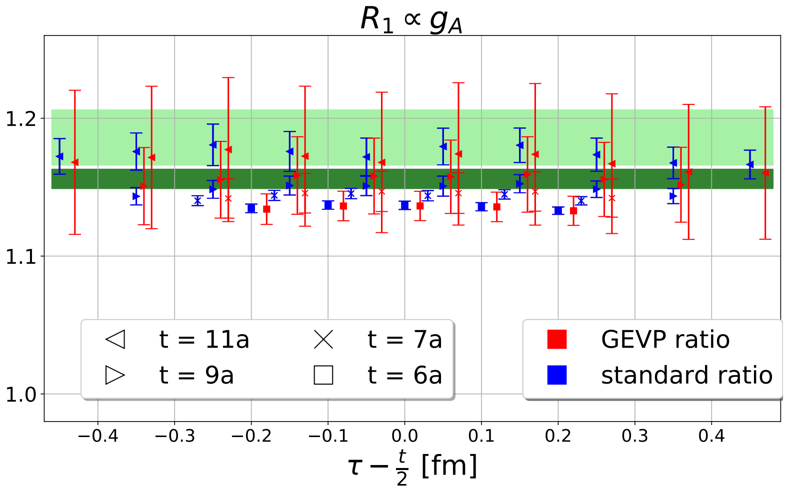

(a) In this plot, we compare the axial charge extracted through the current $\mathscr{A}_j$ with the standard ratio and the GEVP method. No significant effect is observed in this channel, which is consistent with the ChPT prediction. Indeed the axial charge extracted from a rest frame gives $g_A = 1.156 \pm 0.007$, see Fig. 3.5.

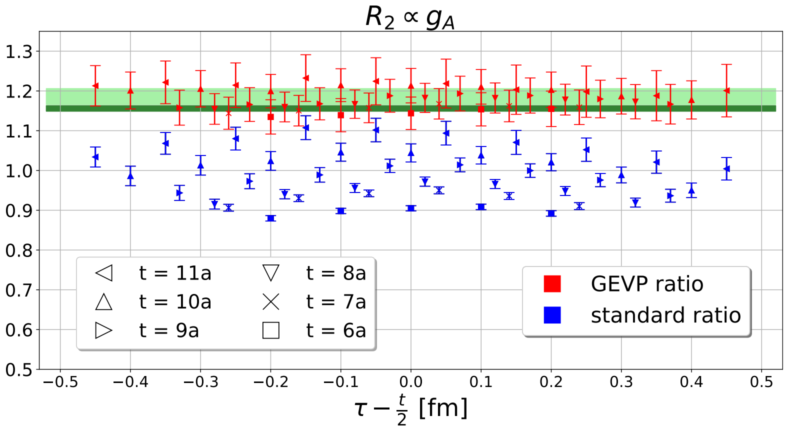

(b) In this plot, we compare the extraction of g_A through the current $\mathscr{A}_4$ between the standard ratio and the GEVP method. The light and dark green bands are the extractions of g_A through $\mathscr{A}_j$ with $\mathbf{p}' = \hat{e}_j$ and $\mathbf{p}' = \mathbf{0}$, respectively. With the GEVP method, the data points lay on the green bands, as expected.

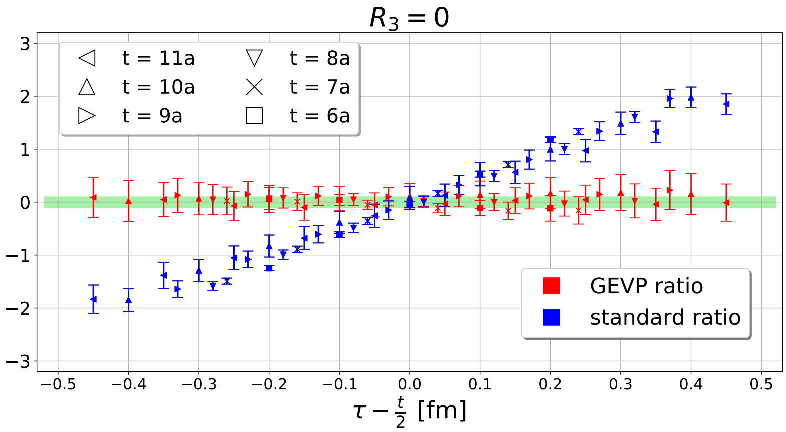

(c) In this plot, we present the ratio R_3 also shown in Fig. 3.9. The (nucleon) ground state contribution to this ratio is zero, but the standard ratio provides a non-vanishing signal. Instead, the GEVP method removes the unwanted contamination due to the $N\pi$ states.

Figure 5.1:
Comparisons of the standard ratios in eqs. (3.72), (3.73), (3.75) with the GEVP ratios in eqs. (5.10)-(5.12). For each of these plots, we use the same generalized eigenvectors, evaluated at $t_0 = 2a$ and $t_2 = t_1 = 2a$. The green bands in each of these plots represent the expected results, either obtained from uncontaminated channels like in (b), or calculated analytically, like in (c). Some ratios are slightly shifted horizontally to improve their visibility, and the data points at source and sink are omitted.

5.4 Nucleon matrix elements with $\mathbf{q} \neq \mathbf{0}$

We apply the GEVP-projection method also at $Q^2 \neq 0$, which is phenomenologically more interesting. We construct the unrenormalised GEVP-projected ratio defined in eq. (5.8), that should represent an improved version of the standard ratios in eq. (3.45).

$$R^{\mathbb{P}}_{\mathscr{J}}(\mathbf{p}', t; \mathbf{q}, \tau)^{(\text{GEVP})} \equiv \frac{\mathscr{C}^{\mathbb{P}^j, \mathscr{J}_-}_{3pt}(\mathbf{p}', t; \mathbf{q}, \tau)^{NN}}{\mathscr{C}_{2pt}(\mathbf{p}', t)^N} \sqrt{\frac{\mathscr{C}_{2pt}(\mathbf{p}', \tau)^N \, \mathscr{C}_{2pt}(\mathbf{p}', t)^N \, \mathscr{C}_{2pt}(\mathbf{p}, t-\tau)^N}{\mathscr{C}_{2pt}(\mathbf{p}, \tau)^N \, \mathscr{C}_{2pt}(\mathbf{p}, t)^N \, \mathscr{C}_{2pt}(\mathbf{p}', t-\tau)^N}}\,. \tag{5.14}$$

In particular, we investigate the same channels[1] that are presented in eqs. (3.47)-(3.50) with $\mathbf{p}' = \mathbf{0}$, $\mathbf{q} = -\mathbf{p} = \hat{e}_j$ by using the GEVP-improved operators

$$R^{\mathbb{P}^j}_{\mathscr{P}}(\mathbf{0}, t; \hat{e}_j, \tau)^{(\text{GEVP})} = \frac{e_j}{\sqrt{2E_N(E_N + m_N)}}\; G_P(\tilde{Q}^2) + \dots \tag{5.15}$$

$$R^{\mathbb{P}^j}_{\mathscr{A}_j}(\mathbf{0}, t; \hat{e}_j, \tau)^{(\text{GEVP})} = \frac{i}{\sqrt{2E_N(E_N + m_N)}} \left[(E_N + m_N) G_A(\tilde{Q}^2) - \frac{(e_j)^2}{2m_N} G_{\tilde{P}}(\tilde{Q}^2) \right] + \dots \tag{5.16}$$

$$R^{\mathbb{P}^j}_{\mathscr{A}_j}(\mathbf{0}, t; \hat{e}_{k\neq j}, \tau)^{(\text{GEVP})} = \frac{i(E_N + m_N)}{\sqrt{2E_N(E_N + m_N)}} G_A(\tilde{Q}^2) + \dots \tag{5.17}$$

$$R^{\mathbb{P}^j}_{\mathscr{A}_4}(\mathbf{0}, t; \hat{e}_j, \tau)^{(\text{GEVP})} = \frac{e_j}{\sqrt{2E_N(E_N + m_N)}} \left[G_A(\tilde{Q}^2) + \frac{(m_N - E_N)}{2m_N} G_{\tilde{P}}(\tilde{Q}^2) \right] + \dots \tag{5.18}$$

where e_j is the value of the unit vector $\hat{e}_j$ along the direction j, i.e. $e_j = \frac{2\pi}{L}$. Notice that in the construction of the third ratio, we consider a spatial current $\mathscr{A}_j$ and a polarization projector $\mathbb{P}^j$ as in the second ratio, but the current does not carry momentum in the same direction (j). For our kinematic choice, the momentum transfer is $\tilde{Q}^2 = (E_N - m_N)^2 + |\hat{e}_z|^2 \approx 0.290$ GeV^2, so that $\tilde{Q}^2 + m_\pi^2 = 0.473$ GeV^2. At this energy scale, the PCAC violation is not larger than 15%, see Fig. 9 in [27] and the lattice artefacts for our ensemble can also be relevant.

As discussed in Sec. 3.4, we extract the axial form factor $G_A(\tilde{Q}^2)$ from the ratio in eq. (5.17). For this channel, the three-point correlation functions are not affected by the GEVP projection, as expected from ChPT. The reason is that the dominant signal in the nucleon to nucleon-pion three-point functions comes from the disconnected diagrams with the $D-like$ topology, see lower left sketch in Fig. 4.1, and this diagram inherits the signal from the nucleon two-point functions and meson-to-current two-point functions. The latter contains the matrix element $\langle \Omega | \mathscr{A}_j(q) \left| \pi(q) \right\rangle = i f_\pi q_j$, which clearly vanishes for the ratio in eq. (5.17), where $q_j = 0$. More details on this are at the end of Sec. 4.2. In Fig. 5.2, we plot the ratio in eq. (3.49) at different source-sink separations, and we extract the axial form factor $G_A(\tilde{Q}^2)$ at large source-sink separations, where a plateau is observed.

---

[1] We do not employ $\mathscr{O}$(a)-improvement in this analysis, but it will be performed in the future.

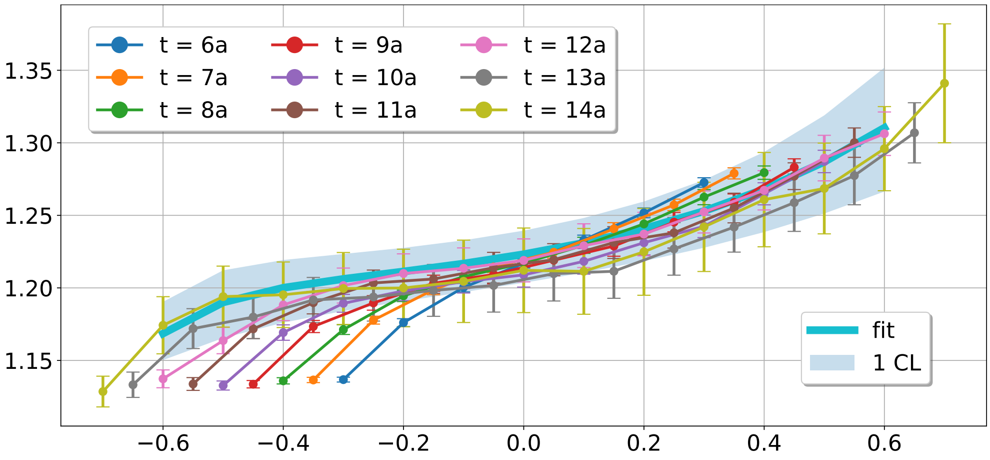

Figure 5.2:
In this figure, I show the traditional ratio in eq. (3.49), which is equivalent to the ratio in eq. (5.17) at several source-sink separations 0.6 fm ≤ t ≤ 1.4 fm, computed with smeared nucleon interpolators. It is clear that at large source-sink separations a plateau region forms, and we extract the axial form factor G_A, which is reported in eq. (5.20). The light blue line and the shaded band represent the fit with 1 confidence level.

We take into account the exponential corrections at source and sink by using the fit formula

$$-iR^{\mathbb{P}^j}_{\mathscr{A}_j}(\mathbf{0},t;\hat{e}_{k\neq j},\tau) = \frac{(E_N+m_N)}{\sqrt{2E_N(E_N+m_N)}}G_A(\tilde{Q}^2)+\alpha_{src}e^{-\delta E_{src}t}+\alpha_{sink}e^{-\delta E_{sink}(t-\tau)} \tag{5.19}$$

and we find that the unrenormalised[2] axial form factor $G_A(\tilde{Q}^2 \approx 0.290\ \text{GeV}^2)$ is

$$G_A(\tilde{Q}^2) = 1.218 \pm 0.020\ , \tag{5.20}$$

where the error is determined with the bootstrapping method. The fit is performed using the largest source-sink separations $t = 1.2$ fm, 1.3 fm, 1.4 fm and this result for G_A is used for the extraction of $G_{\tilde{P}}$ from the other ratios. In Fig. 5.3, we show the comparison plots between the traditional and contaminated ratios in eqs. (3.48), (3.50), (3.50) and the respective GEVP-improved ratios in eqs. (5.15), (5.16) and (5.18). The green band in each of these plots represent the nucleon ground state result, i.e., the form factors extracted from a fit that satisfy the PCAC and PPD relation are inserted in the respective analytical formula for the ratio in eqs. (5.15)-(5.18).

It is clear that the GEVP method improves significantly the ratios in all the channels, especially at the source ($\tau = 0$) with momentum $\mathbf{p} = -\mathbf{q} = -\hat{e}_z$, as the GEVP-improved data points lie closer to the nucleon ground state. However, there is some trace of contamination left at the sink ($\tau = t$), where the momentum is $\mathbf{p}' = \mathbf{0}$.

---

[2] We may renormalise the form factor by multiplying it by $Z_A = 0.7456(10)^{\text{stat}}(57)^{\text{syst}}$, introduced in Sec. 3.5.

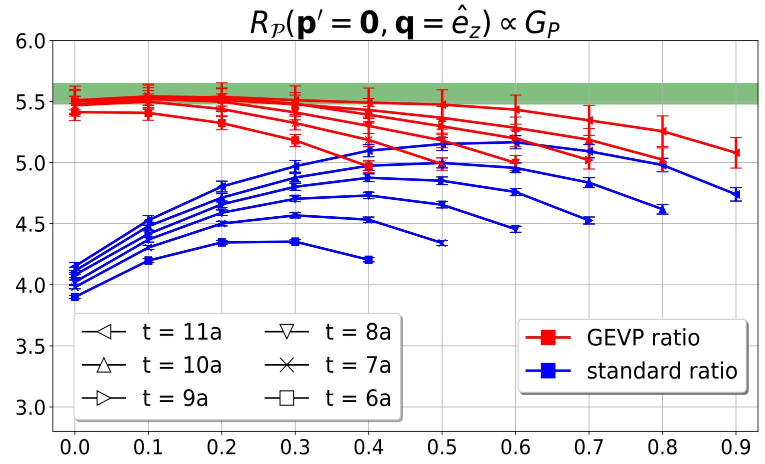

(a) In this plot, we compare the results of the ratio with a pseudoscalar current $\mathscr{P}$ by using the standard operators (blue data points) and the GEVP-projected operators (red data points), respectively eq. (3.47) and eq. (5.15). At different source-sink separations t, it is clear that the GEVP-method removes most of the contamination at the source, where the momentum is $\mathbf{p} = -\hat{e}_z$, while there are some traces of contamination left at the sink, where $\mathbf{p}' = \mathbf{0}$.

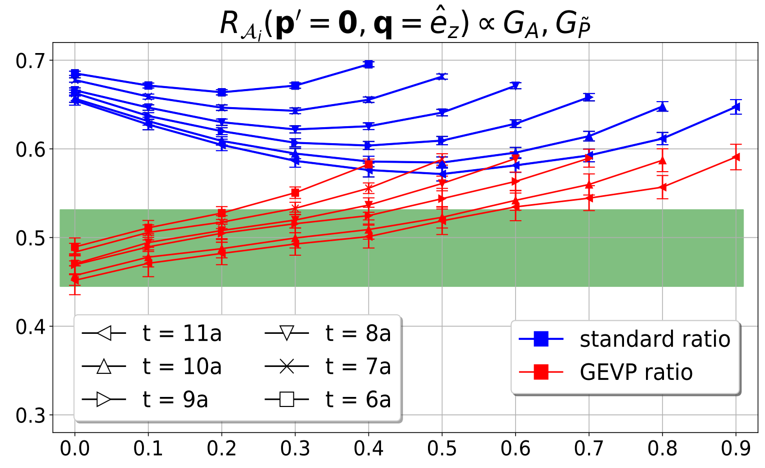

(b) In this plot, we compare the results of the ratio with a spatial axial current $\mathscr{A}_j$ by using the standard operators (blue data points) and the GEVP-projected operators (red data points), respectively eq. (3.48) and eq. (5.16). At different source-sink separations t, it is clear that the GEVP method removes also here most of the contamination at the source, while there is some traces of contamination left at the sink.

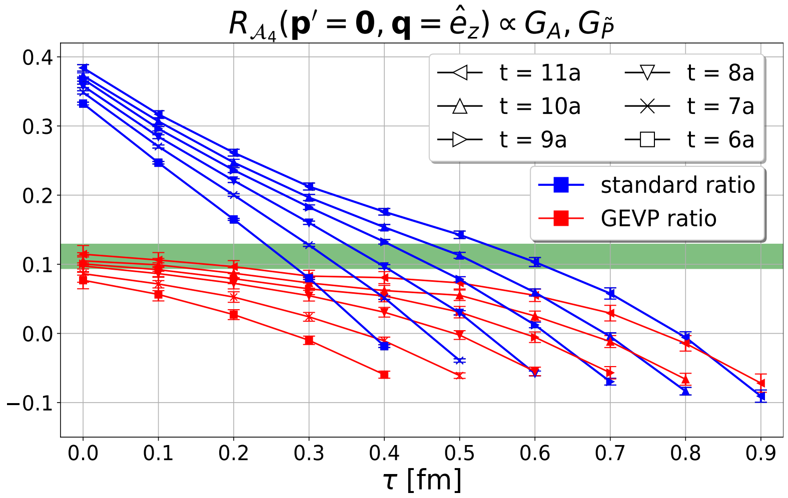

(c) In this plot, we compare the results of the ratio with a temporal axial current $\mathscr{A}_4$ by using the standard operators (blue data points) and the GEVP-projected operators (red data points), respectively eq. (3.50) and eq. (5.16). At different source-sink separations t, it is clear that the GEVP method removes also here most of the contamination at the source, while there are some traces of contamination left at the sink.

Figure 5.3:
Comparisons of the results for the standard ratios in eqs. (3.47), (3.48), (3.50) with the GEVP-improved ratios in eqs. (5.15), (5.16), (5.18), respectively. The kinematic is such that the nucleon at the sink has momentum zero ($\mathbf{p}' = \mathbf{0}$) and $\mathbf{q} = \hat{e}_z$, so that $\mathbf{p} = -\hat{e}_z$. For each of these plots, we use the same generalized eigenvectors, evaluated at $t_0 = 2a$ and $t_2 = t_1 = 2a$. The green bands in each of these plots represent the nucleon ground state expected results, which are extracted as discussed in the main text. Some ratios are slightly shifted horizontally to improve their visibility, and the data points at source and sink are omitted.

As expected, we observe that the remaining contamination at the sink decreases with the source-sink separation. Furthermore, the analytical expectation for the double ratio

$$\frac{R^{\mathbb{P}^j}_{\mathscr{A}_j}(\mathbf{0}, t; \mathbf{q} = \hat{e}_j, \tau)}{R^{\mathbb{P}^j}_{\mathscr{A}_4}(\mathbf{0}, t; \mathbf{q} = \hat{e}_j, \tau)} = \frac{E_N + m_N}{e_j} \approx 4.69 \tag{5.21}$$

is violated with the standard ratios, but the GEVP-improved ratios reproduce this value quite precisely at the source. I will now discuss how we extracted all the form factors reliably and used these results to plot the green band in the plots.

The nucleon axial form factor G_A is obtained through the fit in eq. (5.19), and it is given in eq. (5.20). We compare three different fit methods in order to extract the other form factors $G_P(Q^2)$, $G_{\tilde{P}}(Q^2)$ from the remaining ratios so that they satisfy the PCAC and PPD relations, i.e.

$$\textbf{PPD:} \quad G_{\tilde{P}}(Q^2) = \frac{4m_N^2 G_A(Q^2)}{m_\pi^2 + Q^2} \quad \longrightarrow \quad r_{\text{PPD}} = \frac{\left(m_\pi^2 + Q^2\right) G_{\tilde{P}}(Q^2)}{4m_N^2 G_A(Q^2)}\,, \tag{5.22}$$

$$\textbf{PCAC:} \quad G_A(Q^2) = \frac{m_\ell}{m_N} G_P(Q^2) + \frac{Q^2}{4m_N^2} G_{\tilde{P}}(Q^2) \quad \longrightarrow \quad r_{\text{PCAC}} = \frac{m_\ell G_P(Q^2) + \frac{Q^2}{4m_N} G_{\tilde{P}}(Q^2)}{m_N G_A(Q^2)}\,. \tag{5.23}$$

These methods are:

1. **Los Alamos approach [100]:** We extract G_P from the traditional (contaminated) ratio in eq. (3.47) by including some exponential corrections at source and sink, similarly to eq. (5.19). In more detail, the fit formula for the extraction of G_P is

$$R^{\mathbb{P}^j}_{\mathscr{P}}(\mathbf{0}, t; \hat{e}_j, \tau) = \frac{e_j\, G_P(\tilde{Q}^2)}{\sqrt{2E_N(E_N + m_N)}} + \alpha^{\mathscr{P}}_{src} e^{-\delta E_{src} t} + \alpha^{\mathscr{P}}_{sink} e^{-\delta E_{sink}(t-\tau)}\,. \tag{5.24}$$

We then use our results for G_A in eq. (5.20) to perform a simultaneous fit to the ratios in eqs. (3.48), (3.50) to extract $G_{\tilde{P}}$. For the simultaneous fit, we use the following fit ansatz:

$$-iR^{\mathbb{P}^j}_{\mathscr{A}_j}(\mathbf{0}, t; \hat{e}_j, \tau) \;= \frac{(E_N + m_N) G_A(\tilde{Q}^2) - \frac{e_j^2}{2m_N} G_{\tilde{P}}(\tilde{Q}^2)}{\sqrt{2E_N(E_N + m_N)}} + \alpha^{\mathscr{A}_j}_{src} e^{-\delta E_{src} t} + \alpha^{\mathscr{A}_j}_{sink} e^{-\delta E_{sink}(t-\tau)}\,, \tag{5.25}$$

$$R^{\mathbb{P}^j}_{\mathscr{A}_4}(\mathbf{0}, t; \hat{e}_j, \tau) \;= e_j \frac{G_A(\tilde{Q}^2) + \frac{(m_N - E_N)}{2m_N} G_{\tilde{P}}(\tilde{Q}^2)}{\sqrt{2E_N(E_N + m_N)}} + \alpha^{\mathscr{A}_4}_{src} e^{-\delta E_{src} t} + \alpha^{\mathscr{A}_4}_{sink} e^{-\delta E_{sink}(t-\tau)}\,. \tag{5.26}$$

Notice that we fix the excited state energy gap δE_{src} and δE_{sink} to be the same in both channels because $N\pi$ states are expected to be the dominant contamination in both channels. However, the appearing prefactors $\alpha^{\mathscr{J}}_{src}$ and $\alpha^{\mathscr{J}}_{sink}$ could be different. This extraction method is very similar to what has been performed in [100], where the energy gap is extracted solely from $\mathscr{A}_4$ and used for the other channels. The best fit results are obtained from a simultaneous fit to all three channels and are

$$G_P(\tilde{Q}^2) = 25.836 \pm 0.771\,, \qquad G_{\tilde{P}}(\tilde{Q}^2) = 14.417 \pm 0.508\,, \tag{5.27}$$

which satisfy the PCAC and PPD ratios:

$$r_{\text{PCAC}}(\tilde{Q}^2) = 1.005 \pm 0.016\,, \qquad r_{\text{PPD}}(\tilde{Q}^2) = 1.008 \pm 0.016\,. \tag{5.28}$$

2. **RQCD approach [27]:** We work with the traditional (contaminated) ratios, and we use the ChPT-based ansatz explained in [27], where the energy gaps are known to be the $N\pi$ non-interacting energies. The fit formulas that are used to take into account just the $N\pi$ contamination are calculated at LO-ChPT and are derived from eqs. (2.44), (2.45) in [27]. These fit ansätze are very similar to eqs. (5.24)-(5.26), with the difference that δE_{src} and δE_{sink} are not fit parameters, but they are determined at LO-ChPT. The independent fit to the ratios in eqs. (3.47), (3.48) with $t = 14a$ gives the following results:

$$G_P(\tilde{Q}^2) = 26.913 \pm 0.715\,, \qquad G_{\tilde{P}}(\tilde{Q}^2) = 15.068 \pm 0.506\,, \tag{5.29}$$

$$r_{\text{PCAC}}(\tilde{Q}^2) = 1.049 \pm 0.017\,, \qquad r_{\text{PPD}}(\tilde{Q}^2) = 1.053 \pm 0.031\,. \tag{5.30}$$

3. **GEVP approach [36]:** Finally, we extract the form factors from the GEVP-projected ratios, which is the novelty of this project. The time-dependence of the ratios in Fig. 5.3 suggests that most of the contamination at the source with momentum $\mathbf{p} = \hat{e}_z$ is removed. However, there is some trace of contamination left at the sink that is fitted with an exponential form. Therefore, we use the following fit ansatz for the projected ratios:

$$R^{\mathbb{P}^j}_{\mathscr{P}}(\mathbf{0}, t; \hat{e}_j, \tau)^{(\text{GEVP})} = \frac{e_j\, G_P(\tilde{Q}^2)}{\sqrt{2E_N(E_N + m_N)}} + \alpha^{\mathscr{P}}_{sink} e^{-\delta E_{sink}(t-\tau)}\,, \tag{5.31}$$

$$R^{\mathbb{P}^j}_{\mathscr{A}^j}(\mathbf{0}, t; \hat{e}_j, \tau)^{(\text{GEVP})} = \frac{(E_N + m_N) G_A(\tilde{Q}^2) - \frac{(e_j)^2}{2m_N} G_{\tilde{P}}(\tilde{Q}^2)}{\sqrt{2E_N(E_N + m_N)}} + \alpha^{\mathscr{A}^j}_{sink} e^{-\delta E_{sink}(t-\tau)}\,, \tag{5.32}$$

$$R^{\mathbb{P}^j}_{\mathscr{A}^4}(\mathbf{0}, t; \hat{e}_j, \tau)^{(\text{GEVP})} = e_j \frac{G_A(\tilde{Q}^2) + \frac{(m_N - E_N)}{2m_N} G_{\tilde{P}}(\tilde{Q}^2)}{\sqrt{2E_N(E_N + m_N)}} + \alpha^{\mathscr{A}^4}_{sink} e^{-\delta E_{sink}(t-\tau)}\,. \tag{5.33}$$

The fit results to eqs. (5.31), (5.33) for the form factors with $t = 10a$ are

$$G_P(\tilde{Q}^2) = 26.662 \pm 0.404\,, \qquad G_{\tilde{P}}(\tilde{Q}^2) = 14.332 \pm 1.340\,, \tag{5.34}$$

$$r_{\text{PCAC}}(\tilde{Q}^2) = 1.013 \pm 0.061\,, \qquad r_{\text{PPD}}(\tilde{Q}^2) = 1.002 \pm 0.093\,. \tag{5.35}$$

The GEVP ratios are not averaged over all equivalent directions. This would increase the statistics and lead to better fit results, especially for $G_{\tilde{P}}$. However, unlike the contaminated ratios, the fit results with the GEVP ratios are all consistent with each other even with a naive fit, confirming the ChPT-inspired approaches.

CHAPTER

SIX

SUMMARY AND OUTLOOK

In this project, we have investigated new three-point correlation functions for the first time, consisting of a 3-quark operator (nucleon) at the source, a 5-quark operator (nucleon-pion) at the sink and a current $\mathscr{J}$. These correlation functions enable the computation of finite-volume transition matrix elements $\langle N\pi|\mathscr{J}|N\rangle$, which enter as a contamination in the traditional correlation functions that consist of a 3-quark operator (nucleon) both at the source and at the sink, and a current $\mathscr{J}$. The motivation for this project is two-fold: first we want to remove this unwanted excited-state contamination from the (nucleon) ground state, and second we want to compute numerically $\langle N\pi|\mathscr{J}|N\rangle$ for the first time as it is phenomenologically very relevant for experimental particle physics and in particular for neutrino-nuclei scattering.

We find that this method provides results compatible with effective field theory predictions. Results that were inconsistent in the forward limit with the traditional method due to the $N\pi$ contamination, see Sec. 5.3, are now compatible with the nucleon ground state expectation. In particular, the axial charge extracted from the channel with a temporal axial current $\mathscr{A}_4$ provides results that are compatible with those extracted from the axial current $\mathscr{A}_j$ within the errors, see Fig. 5.1b. The GEVP-improved ratios at different source-sink separations with a pseudoscalar current $\mathscr{P}$ are consistent with zero within the errors, see Fig. 5.1c.

At $Q^2 \neq 0$ GeV^2, we also find a significant improvement in the ratios. We have investigated three-point correlation functions with zero momentum at the sink $\mathbf{p}' = \mathbf{0}$ and momentum transfer $\mathbf{q} = -\mathbf{p} = \hat{e}_z$, where $\hat{e}_z$ is the lattice unit momentum along the direction z. We observe from Fig. 5.3 that in all the channels, the GEVP-projection successfully removes the contamination where the nucleon is not at rest. The results suggest a new fit formula to extract the nucleon form factors G_P and $G_{\tilde{P}}$. In contrast, the axial form factor G_A is extracted in the traditional way from a channel that suffers less from contamination. The nucleon form factors satisfy the PCAC and PPD relation and are consistent within the errors with methods based on a multiparticle fit (Los Alamos approach) or ChPT-based ansatz (RQCD approach).

In particular, with this method, we understand that the contamination due to $N\pi$ states in the standard nucleon three-point functions is enhanced when the disconnected diagram is non-vanishing. For this term to contribute, the meson matrix element $\langle\Omega|\mathscr{J}(\mathbf{q})\left|\pi(\mathbf{p}_\pi)\right\rangle$ must not vanish. Therefore, in the forward limit ($\mathbf{q} = \mathbf{0}$), only $\langle\Omega|\mathscr{A}_4(\mathbf{0})\,|\pi(\mathbf{0})\rangle\,, \langle\Omega|\mathscr{P}(\mathbf{0})\,|\pi(\mathbf{0})\rangle \neq 0$, while at non-vanishing momentum transfer we have that $\langle\Omega|\mathscr{A}_4(\mathbf{q})\left|\pi(\mathbf{q})\right\rangle$, $\langle\Omega|\mathscr{P}(\mathbf{q})\left|\pi(\mathbf{q})\right\rangle \neq 0$ and $\langle\Omega|\mathscr{A}_j(\mathbf{q})\left|\pi(\mathbf{q})\right\rangle \neq 0$ only if $q_j \neq 0$.

In this dissertation, I have not presented results for $\langle N\pi|\mathscr{J}|N\rangle$ matrix elements, but they will be investigated in the future. In particular, the door is open for extrapolating these finite-volume matrix elements to the physical limit, which are relevant to phenomenologically interesting transition amplitudes.

These results for the GEVP-improved matrix elements computed on a single ensemble are very promising. We plan to extend the work to other ensembles and take the continuum limit.

Appendices

APPENDIX

ONE

USEFUL IDENTITIES

A.1 Gamma matrices and their algebra

A.1.1 Minkowski spacetime

In the Weyl (chiral) representation, a possible form of the gamma matrices in Minkowski spacetime is

$$\gamma^0 = \begin{pmatrix} 0 & I_2 \\ I_2 & 0 \end{pmatrix} , \qquad \gamma^k = \begin{pmatrix} 0 & \sigma_k \\ -\sigma_k & 0 \end{pmatrix} , \qquad \gamma^5 = \begin{pmatrix} -I_2 & 0 \\ 0 & I_2 \end{pmatrix} , \tag{A.1}$$

where I_n represents the $n \times n$ identity matrix and they are expressed in terms of the Pauli matrices σ_k, which are defined like:

$$\sigma_1 = \begin{pmatrix} 0 & 1 \\ 1 & 0 \end{pmatrix} , \qquad \sigma_2 = \begin{pmatrix} 0 & -i \\ i & 0 \end{pmatrix} , \qquad \sigma_3 = \begin{pmatrix} 1 & 0 \\ 0 & -1 \end{pmatrix} . \tag{A.2}$$

Here we also recall the properties of the gamma matrices and the relation between γ_5 and the other γ_μ:

$$\{\gamma^\mu, \gamma^\nu\} := \gamma^\mu \gamma^\nu + \gamma^\nu \gamma^\mu = 2 g^{\mu\nu} I_4 , \qquad \{\gamma^\mu, \gamma^5\} = 0 , \tag{A.3}$$

$$\gamma^5 = i \gamma^0 \gamma^1 \gamma^2 \gamma^3 = \frac{i}{4!} \epsilon_{\mu\nu\alpha\beta} \, \gamma^\mu \gamma^\nu \gamma^\alpha \gamma^\beta , \tag{A.4}$$

which hold $\forall \; \mu, \nu \in \{0, 1, 2, 3\}$. In the previous formula, $g^{\mu\nu}$ represents the metric tensor, which in the Minkowski metric has the signature $\{+, -, -, -\}$ and $\epsilon_{\mu\nu\rho\sigma}$ is the Levi-Civita tensor, with $\epsilon_{0123} = +1$. With this convention for the metric, the covariant gamma matrices are defined by

$$\gamma_\mu = g_{\mu\nu} \gamma^\nu = \{\gamma^0, -\gamma^1, -\gamma^2, -\gamma^3\} . \tag{A.5}$$

Other important identities which come in handy when computing traces of products of gamma matrices are the trace identities. These are:

1. trace of any product of an odd number of γ^μ is 0 ; (A.6)
2. $\mathrm{tr}\left[\gamma^\mu\gamma^\nu\right] = 4g^{\mu\nu}$; (A.7)
3. $\mathrm{tr}\left[\gamma^\mu\gamma^\nu\gamma^\rho\gamma^\sigma\right] = 4(g^{\mu\nu}g^{\rho\sigma} - g^{\mu\rho}g^{\nu\sigma} + g^{\mu\sigma}g^{\nu\rho})$; (A.8)
4. $\mathrm{tr}\left[\gamma^5\right] = \mathrm{tr}\left[\gamma^\mu\gamma^\nu\gamma^5\right] = 0$; (A.9)
5. $\mathrm{tr}\left[\gamma^\mu\gamma^\nu\gamma^\rho\gamma^\sigma\gamma^5\right] = -4i\epsilon^{\mu\nu\rho\sigma}$; (A.10)
6. $\mathrm{tr}\left[\gamma^{\mu_1}\dots\gamma^{\mu_N}\right] = \mathrm{tr}\left[\gamma^{\mu_N}\dots\gamma^{\mu_1}\right]$. (A.11)

In this basis, the charge conjugation operator C, which is defined to satisfy the representation-independent relation $C\gamma_\mu C^{-1} = -(\gamma_\mu)^\intercal$, reads and satisfies

$$C = i\gamma^2\gamma^0 = \begin{pmatrix} i\sigma_2 & 0 \\ 0 & -i\sigma_2 \end{pmatrix}, \qquad (C)^\intercal = C^\dagger = C^{-1} = -C\,. \tag{A.12}$$

A.1.2 Euclidean spacetime

The Euclidean spacetime metric is obtained after applying the Wick rotation in eq. (2.17). Therefore, if we reverse it, the Euclidean four-vectors are related to the Minkowski by the following:

$$x_E^4 = ix^0\,, \qquad x_E^j = x^j = -x_j\,, \tag{A.13}$$

where in the following, the Euclidean objects have a superscript label "E" to distinguish them from the others in Minkowski spacetime.

The convention for the Euclidean γ matrices is the DeGrand-Rossi basis, which is adopted by the software packages CHROMA, GRID and GPT. The γ matrices read

$$\gamma^1 = \begin{pmatrix} 0 & i\sigma_1 \\ -i\sigma_1 & 0 \end{pmatrix}, \quad \gamma^2 = \begin{pmatrix} 0 & -i\sigma_2 \\ i\sigma_2 & 0 \end{pmatrix}, \tag{A.14}$$

$$\gamma^3 = \begin{pmatrix} 0 & i\sigma_3 \\ -i\sigma_3 & 0 \end{pmatrix}, \quad \gamma^4 = \begin{pmatrix} 0 & I_2 \\ I_2 & 0 \end{pmatrix}, \quad \gamma^5 = \begin{pmatrix} I_2 & 0 \\ 0 & -I_2 \end{pmatrix} = \gamma^1\gamma^2\gamma^3\gamma^4\,. \tag{A.15}$$

With this choice, the trace identities in eqs. (A.6)-(A.11) become:

1. trace of any product of an odd number of γ^μ is 0 ; (A.16)
2. $\mathrm{tr}\left[\gamma^\mu\gamma^\nu\right] = 4\delta^{\mu\nu}$; (A.17)
3. $\mathrm{tr}\left[\gamma^\mu\gamma^\nu\gamma^\rho\gamma^\sigma\right] = 4(\delta^{\mu\nu}g^{\rho\sigma} - \delta^{\mu\rho}\delta^{\nu\sigma} + \delta^{\mu\sigma}\delta^{\nu\rho})$; (A.18)
4. $\mathrm{tr}\left[\gamma^5\right] = \mathrm{tr}\left[\gamma^\mu\gamma^\nu\gamma^5\right] = 0$; (A.19)
5. $\mathrm{tr}\left[\gamma^\mu\gamma^\nu\gamma^\rho\gamma^\sigma\gamma^5\right] = +4\epsilon^{\mu\nu\rho\sigma}$; (A.20)
6. $\mathrm{tr}\left[\gamma^{\mu_1}\dots\gamma^{\mu_N}\right] = \mathrm{tr}\left[\gamma^{\mu_N}\dots\gamma^{\mu_1}\right]$; (A.21)

with $\epsilon^{1234} = +1$. The charge conjugation operator C reads and satisfies again

$$C = \gamma^2\gamma^4 = \begin{pmatrix} -i\sigma_2 & 0 \\ 0 & i\sigma_2 \end{pmatrix} , \qquad (C)^\intercal = C^\dagger = C^{-1} = -C . \tag{A.22}$$

Another property that will be useful in e.g. App. C is the following:

$$(C\gamma_5)^\intercal = -C\gamma_5 . \tag{A.23}$$

A.2 Useful trace identities

I leave here the results in Minkowski spacetime of traces like

$$\mathrm{Tr}\left\{\mathbb{P}(\not{p} + m)\right\} , \tag{A.24}$$

$$\mathrm{Tr}\left\{\mathbb{P}(\not{p}' + m)\Gamma(\not{p} + m)\right\} , \tag{A.25}$$

with $\Gamma \in \{\mathbb{1}, \gamma^5, \gamma^\mu, \gamma^\mu\gamma^5\}$, $\mathbb{P} \in \{\mathbb{P}^+, \mathbb{P}^{+j}\}$ and

$$\mathbb{P}^\pm = \frac{1}{2}(\mathbb{1} \pm \gamma^0) , \qquad \mathbb{P}^{+j} = \mathbb{P}^+\gamma^j\gamma^5 , \qquad p' = (E', \mathbf{p}') , \qquad p = (E, \mathbf{p}) , \tag{A.26}$$

which appear in the spectral decomposition of nucleon two- and three-point functions. Notice that I omit the subscript "N" on purpose. Here is the list of traces:

$$\mathrm{Tr}\{\mathbb{P}^{+}(\not{p}+m)\} = 2(E+m)\,, \tag{A.27}$$

$$\mathrm{Tr}\{\mathbb{P}^{+}(\not{p}'+m)\,\gamma^{5}(\not{p}+m)\} = 0\,, \tag{A.28}$$

$$\mathrm{Tr}\{\mathbb{P}^{+}(\not{p}'+m)\,\gamma^{\mu}\,\gamma^{5}(\not{p}+m)\} = 2i\epsilon^{0\rho\mu\nu}\,p'_{\rho}p_{\nu}\,, \tag{A.29}$$

$$\mathrm{Tr}\{\mathbb{P}^{+}(\not{p}'+m)\gamma^{\mu}(\not{p}+m)\} = 2\Big[p'^{\mu}(E+m)+p^{\mu}(E'+m)-g^{0\mu}(p'\cdot p-m^{2})\Big]\,, \tag{A.30}$$

$$\mathrm{Tr}\Big\{\mathbb{P}^{+j}(\not{p}'+m)\,\gamma^{5}(\not{p}+m)\Big\} = 2\Big[p^{j}(E+m)-p'^{j}(E'+m)\Big]\,, \tag{A.31}$$

$$\mathrm{Tr}\Big\{\mathbb{P}^{+j}(\not{p}'+m)\,\gamma^{\mu}(\not{p}+m)\Big\} = 2i\Big[\epsilon^{j\rho\mu\nu}p'_{\rho}p_{\nu}-\epsilon^{0j\rho\mu}(p'_{\rho}-p_{\rho})m\Big]\,, \tag{A.32}$$

$$\begin{aligned}\mathrm{Tr}\Big\{\mathbb{P}^{+j}(\not{p}'+m)\,\gamma^{\mu}\gamma^{5}(\not{p}+m)\Big\} = 2\Big[&-g^{j\mu}\big(p'\cdot p+m^{2}+m(E'+E)\big)+\\ &+p'^{\mu}p^{j}+p'^{j}p^{\mu}+mg^{0\mu}(p'^{j}+p^{j})\Big]\,.\end{aligned} \tag{A.33}$$

The Euclidean lattice version of these traces is obtained by using eqs. (A.16)-(A.21), considering that

$$\mathbb{P}^{\pm} = \frac{1}{2}(\mathbb{1}\pm\gamma^{4})\,, \qquad \mathbb{P}^{+j} = \mathbb{P}^{+}i\gamma^{5}\gamma^{j}\,, \qquad p' = (iE',\mathbf{p}')\,, \qquad p = (iE,\mathbf{p}) \tag{A.34}$$

and that the sum over the spins of Dirac spinors $u(\mathbf{p},\sigma)$ becomes

$$\sum_{\sigma} u(\mathbf{p},\sigma)\,\bar{u}(\mathbf{p},\sigma) = -i\not{p}+m\,. \tag{A.35}$$

Therefore,

$$\mathrm{Tr}\{\mathbb{P}^{+}(-i\not{p}+m)\} = 2(E+m)\,, \tag{A.36}$$

$$\mathrm{Tr}\{\mathbb{P}^{+}(-i\not{p}'+m)\,\gamma^{5}(-i\not{p}+m)\} = 0\,, \tag{A.37}$$

$$\mathrm{Tr}\{\mathbb{P}^{+}(-i\not{p}'+m)\,\gamma^{\mu}\,\gamma^{5}(-i\not{p}+m)\} = 2\epsilon^{4\rho\mu\nu}\,p'_{\rho}p_{\nu}\,, \tag{A.38}$$

$$\mathrm{Tr}\{\mathbb{P}^{+}(-i\not{p}'+m)\gamma^{\mu}(-i\not{p}+m)\} = 2\Big[\delta^{4\mu}(m^{2}+p'\cdot p)-i\Big(p'^{\mu}(E+m)+p^{\mu}(E'+m)\Big)\Big]\,, \tag{A.39}$$

$$\mathrm{Tr}\Big\{\mathbb{P}^{+j}(-i\not{p}'+m)\,\gamma^{5}(-i\not{p}+m)\Big\} = 2\Big[p'^{j}(E+m)-p^{j}(E'+m)\Big]\,, \tag{A.40}$$

$$\mathrm{Tr}\Big\{\mathbb{P}^{+j}(-i\not{p}'+m)\,\gamma^{\mu}(-i\not{p}+m)\Big\} = -2\Big[m\epsilon^{4j\rho\mu}(p'_{\rho}-p_{\rho})+i\epsilon^{j\rho\mu\nu}p'_{\rho}p_{\nu}\Big]\,, \tag{A.41}$$

$$\begin{aligned}\mathrm{Tr}\Big\{\mathbb{P}^{+j}(-i\not{p}'+m)\,\gamma^{\mu}\gamma^{5}(-i\not{p}+m)\Big\} = 2\Big[&i\delta^{j\mu}\big(-p'\cdot p+m^{2}+m(E'+E)\big)+\\ &+ip'^{\mu}p^{j}+ip'^{j}p^{\mu}-m\delta^{4\mu}(p'^{j}+p^{j})\Big]\,.\end{aligned} \tag{A.42}$$

These relations are useful for computing the traces that appear in eq. (3.46).

A.3 Spacetime translation operator

In this section, I define the translation and time evolution operators in Minkowski and Euclidean space metrics. Here I use the notation with a hat on top of the operators.

A.3.1 Minkowski spacetime

The time evolution operator $\hat{\mathrm{U}}(\tau)$ is defined such that it acts on a generic interpolating operator $\mathrm{O}(0) \equiv \mathrm{O}$ in the following way:

$$\mathrm{O} \quad \longrightarrow \quad \mathrm{O}(\tau) = \hat{\mathrm{U}}(\tau)^\dagger \, \mathrm{O} \, \hat{\mathrm{U}}(\tau) = e^{i\hat{H}\tau} \, \mathrm{O} \, e^{-i\hat{H}\tau} \,, \qquad \hat{\mathrm{U}}(\tau) = e^{-i\hat{H}\tau} \,, \tag{A.43}$$

while the space translation operator $\hat{\mathrm{T}}(\mathbf{x})$ is

$$\mathrm{O} \quad \longrightarrow \quad \mathrm{O}(\mathbf{x}) = \hat{\mathrm{T}}(\mathbf{x})^\dagger \, \mathrm{O} \, \hat{\mathrm{T}}(\mathbf{x}) = e^{-i\hat{\mathbf{p}}\cdot\mathbf{x}} \, \mathrm{O} \, e^{i\hat{\mathbf{p}}\cdot\mathbf{x}} \,, \qquad \hat{\mathrm{T}}(\mathbf{x}) = e^{i\hat{\mathbf{p}}\cdot\mathbf{x}} \,. \tag{A.44}$$

A.3.2 Euclidean spacetime

We apply the Wick rotation $\tau = -i\,t$ to the Minkowski spacetime operators, and we obtain:

$$\mathrm{O} \quad \longrightarrow \quad \mathrm{O}(t) = \hat{\mathrm{U}}_E(t)^\dagger \, \mathrm{O} \, \hat{\mathrm{U}}_E(t), = e^{+\hat{H}_E t} \, \mathrm{O} \, e^{-\hat{H}_E t} \,, \qquad \hat{\mathrm{U}}_E(t) = e^{-\hat{H}_E t} \,, \tag{A.45}$$

while the space translation operator $\hat{\mathrm{T}}(\mathbf{x})$ is unchanged,

$$\mathrm{O} \quad \longrightarrow \quad \mathrm{O}(\mathbf{x}) = \hat{\mathrm{T}}_E(\mathbf{x})^\dagger \, \mathrm{O} \, \hat{\mathrm{T}}_E(\mathbf{x}) = e^{-i\hat{\mathbf{p}}\cdot\mathbf{x}} \, \mathrm{O} \, e^{i\hat{\mathbf{p}}\cdot\mathbf{x}} \,, \qquad \hat{\mathrm{T}}_E(\mathbf{x}) = e^{i\hat{\mathbf{p}}\cdot\mathbf{x}} \,. \tag{A.46}$$

A.4 Fourier Transform and spectral decomposition

A.4.1 Two-point functions

We apply the Fourier Transform to project the interpolators on a momentum $\mathbf{p}$. Consider a generic two-point function from a point $x_0 = (\mathbf{x}_0, t_0)$ to $x = (\mathbf{x}, t)$, that is

$$C_{2pt}(\mathbf{p}, t, t_0) = \sum_{\mathbf{x}} e^{-i\mathbf{p}\cdot(\mathbf{x}-\mathbf{x}_0)} \langle \mathrm{O}(\mathbf{x}, t) \, \bar{\mathrm{O}}(\mathbf{x}_0, t_0) \rangle \,, \tag{A.47}$$

where I omit the symbol $\langle \cdot \rangle_G$ for the gauge ensemble average and the volume factor. Applying the spectral decomposition and using eqs. (A.45)-(A.46), we obtain

$$\begin{aligned} C_{2pt}(\mathbf{p}, t, t_0) &= \sum_{\mathbf{x}} \sum_{n} e^{-i\mathbf{p}\cdot(\mathbf{x}-\mathbf{x}_0)} \frac{e^{-E_n t}}{2E_n} e^{i\mathbf{p}\cdot\mathbf{x}} \langle \Omega | \mathrm{O} | n \rangle \langle n | \bar{\mathrm{O}} | \Omega \rangle \, e^{+E_n t_0} e^{-i\mathbf{p}\cdot\mathbf{x}_0} \\ &= \sum_{n} \frac{e^{-E_n(t-t_0)}}{2E_n} \langle \Omega | \mathrm{O} | n \rangle \langle n | \bar{\mathrm{O}} | \Omega \rangle \,, \end{aligned} \tag{A.48}$$

where E_n is the energy of the state n with total momentum $\mathbf{p}$, that has the same quantum numbers as the operators O and $\bar{\mathrm{O}}$.

A.4.2 Three-point functions

Consider now a generic three-point function with the same interpolating operators at the source and at the sink as in eq. (A.47) and an additional current $\mathscr{J}$ at $z = (\mathbf{z}, \tau)$, which reads

$$C_{3pt}(\mathbf{p}', \mathbf{q}, t, \tau, t_0) = \sum_{\mathbf{x},\mathbf{z}} e^{-i\mathbf{p}'\cdot(\mathbf{x}-\mathbf{x}_0)} e^{i\mathbf{q}\cdot(\mathbf{z}-\mathbf{x}_0)} \langle \mathrm{O}(\mathbf{x}, t)\ \mathscr{J}(\mathbf{z}, \tau)\ \bar{\mathrm{O}}(\mathbf{x}_0, t_0)\rangle\ . \tag{A.49}$$

Applying the spectral decomposition and omitting t_0 in the brackets of C_{3pt} for aesthetics, we obtain

$$\begin{aligned}
C_{3pt}(\mathbf{p}', \mathbf{q}, t, \tau) &= \sum_{\mathbf{x},\mathbf{z}} e^{-i\mathbf{p}'\cdot(\mathbf{x}-\mathbf{x}_0)} e^{i\mathbf{q}\cdot(\mathbf{z}-\mathbf{x}_0)} \langle \mathrm{O}(\mathbf{x}, t)\ \mathscr{J}(\mathbf{z}, \tau)\ \bar{\mathrm{O}}(\mathbf{x}_0, t_0)\rangle \\
&= \sum_{\mathbf{x},\mathbf{z}} \sum_{n',n} \frac{e^{-i\mathbf{p}'\cdot(\mathbf{x}-\mathbf{x}_0)}}{2E_n'} \frac{e^{i\mathbf{q}\cdot(\mathbf{z}-\mathbf{x}_0)}}{2E_n} \langle \Omega | \mathrm{O}(\mathbf{x}, t) \left| n' \right\rangle \left\langle n' \right| \mathscr{J}(\mathbf{z}, \tau) | n \rangle \langle n | \bar{\mathrm{O}}(\mathbf{x}_0, t_0) | \Omega \rangle \\
&= \sum_{\mathbf{x},\mathbf{z}} \sum_{n',n} \frac{e^{-E_n'(t-\tau)}}{2E_n'} \frac{e^{-E_n(\tau-t_0)}}{2E_n} \langle \Omega | \mathrm{O} \left| n' \right\rangle \left\langle n' \right| \mathscr{J} | n \rangle \langle n | \bar{\mathrm{O}} | \Omega \rangle\, e^{-i(\mathbf{p}'-\mathbf{q}-\mathbf{p})\cdot(\mathbf{z}-\mathbf{x}_0)} \\
&= \sum_{n',n} \frac{e^{-E_n'(t-\tau)}}{2E_n'} \frac{e^{-E_n(\tau-t_0)}}{2E_n} \langle \Omega | \mathrm{O} \left| n' \right\rangle \left\langle n' \right| \mathscr{J} | n \rangle \langle n | \bar{\mathrm{O}} | \Omega \rangle\ .
\end{aligned} \tag{A.50}$$

In the second line, I use the shorthand notation E_n' and E_n to identify the energy of the state n' and n, respectively. The spatial phase factors cancel out for the momentum conservation condition $\mathbf{p}' - \mathbf{q} - \mathbf{p} = 0$, i.e. $\mathbf{q} = \mathbf{p}' - \mathbf{p}$.

APPENDIX

TWO

ISOSPIN PROJECTION

Analogously to the case of the regular spin in quantum mechanics, we define the ladder isospin operators I_+, I_- and I_3, such that they satisfy the commutation relations

$$[I_+, I_-] = 2I_3\ , \qquad [I_3, I_\pm] = \pm I_\pm\ . \tag{B.1}$$

The action of these operators on the light quark states $|u\rangle$, $|\bar{u}\rangle$, $|d\rangle$ and $\left|\bar{d}\right\rangle$ is

$$\begin{aligned}
&I_+ |u\rangle = 0\ , && I_- |u\rangle = |d\rangle\ , && I_3 |u\rangle = +\frac{1}{2} |u\rangle\ , \\
&I_+ |d\rangle = |u\rangle\ , && I_- |d\rangle = 0\ , && I_3 |d\rangle = -\frac{1}{2} |d\rangle\ , \\
&I_+ \left|\bar{d}\right\rangle = 0\ , && I_- \left|\bar{d}\right\rangle = -|\bar{u}\rangle\ , && I_3 \left|\bar{d}\right\rangle = +\frac{1}{2} \left|\bar{d}\right\rangle\ , \\
&I_+ |\bar{u}\rangle = -\left|\bar{d}\right\rangle\ , && I_- |\bar{u}\rangle = 0\ , && I_3 |\bar{u}\rangle = -\frac{1}{2} |\bar{u}\rangle\ .
\end{aligned} \tag{B.2}$$

The Casimir operator of the isospin group $SU(2)$ is

$$I^2 = \frac{1}{2}(I_+ I_- + I_- I_+) + I_3^2 \tag{B.3}$$

and each isospin state $|I, I_3\rangle$ is classified by its eigenvalue with respect to the operators I and I_3:

$$I^2 |I, I_3\rangle = I(I+1) |I, I_3\rangle\ , \qquad I_3 |I, I_3\rangle = I_3 |I, I_3\rangle\ . \tag{B.4}$$

The above-mentioned quark states are isospin states and they form the isodoublets (u, d), $(\bar{d}, \bar{u})$, where

$$|u\rangle = \left|\frac{1}{2}, \frac{1}{2}\right\rangle\ , \quad |d\rangle = \left|\frac{1}{2}, -\frac{1}{2}\right\rangle\ , \quad |\bar{u}\rangle = -\left|\frac{1}{2}, -\frac{1}{2}\right\rangle\ , \quad \left|\bar{d}\right\rangle = \left|\frac{1}{2}, \frac{1}{2}\right\rangle\ . \tag{B.5}$$

In the following, we use the quantum mechanics formula of (iso)spin addition

$$|I,I_z\rangle = \sum_{I_{1z},\, I_{2z}} |I_1,I_{1z};I_2,I_{2z}\rangle \langle I_1,I_{1z};I_2,I_{2z}|I,I_z|I_1,I_{1z};I_2,I_{2z}|I,I_z\rangle \tag{B.6}$$

to write an isospin state $|I,I_z\rangle$ in terms of the addition $I_1 \oplus I_2$. In eq. (B.6), the matrix elements $\langle I_1,I_{1z};I_2,I_{2z}|I,I_z|I_1,I_{1z};I_2,I_{2z}|I,I_z\rangle$ are Clebsch-Gordan coefficients.

Pion: $I = 1$

The pions π are mesons with u- and d-quarks constituents. They form an isotriplet of states $|I=1,I_z=-1\rangle$, $|I=1,I_z=0\rangle$ and $|I=1,I_z=+1\rangle$, which, in analogy with the spin addition, can be seen as the isospin addition of their constituents (the quarks), $I_1 = \frac{1}{2} \oplus I_2 = \frac{1}{2}$.

We start with the isospin state $|1,+1\rangle = -\left|\bar{d}u\right\rangle$ and the others are obtained by applying the ladder operator I_-:

$$I_-\,|1,+1\rangle = \sqrt{2}\,|1,0\rangle\ , \qquad I_-(-\left|\bar{d},u\right\rangle) = |\bar{u},u\rangle - \left|\bar{d},d\right\rangle\ , \tag{B.7}$$

$$|1,0\rangle = \frac{1}{\sqrt{2}}(|\bar{u},u\rangle - \left|\bar{d},d\right\rangle)\ . \tag{B.8}$$

We apply again the operator I_- to the state $|1,0\rangle$ to get $|1,-1\rangle$,

$$I_-\,|1,0\rangle = \sqrt{2}\,|1,-1\rangle\ , \qquad I_-\frac{1}{\sqrt{2}}(|\bar{u},u\rangle - \left|\bar{d},d\right\rangle) = \sqrt{2}\,|\bar{u},d\rangle\ , \tag{B.9}$$

$$|1,-1\rangle = |\bar{u},d\rangle\ . \tag{B.10}$$

The pions π are mesons with isospin $I = 1$ and they form the isospin triplet (π^+,π^0,π^-), where

$$\left|\pi^+\right\rangle = -\left|\bar{d},u\right\rangle\ , \qquad \left|\pi^0\right\rangle = \frac{1}{\sqrt{2}}(|\bar{u},u\rangle - \left|\bar{d},d\right\rangle)\,, \qquad |\pi^-\rangle = |\bar{u},d\rangle\ . \tag{B.11}$$

The construction of these states is similar to the spin-1 case in quantum mechanics. However, the overall minus sign for $\left|\pi^+\right\rangle$ and the relative minus sign for $\left|\pi^0\right\rangle$ is due to the definition of eq. (B.2).

Nucleon: $I = 1/2$

The nucleon states $|N\rangle$, baryons with $I = 1/2$ and $I_z = \pm 1/2$, are constructed from the light quarks

$$\left|p\right\rangle = |d,u,u\rangle = \left|\frac{1}{2},+\frac{1}{2}\right\rangle\ , \qquad \left|p\right\rangle = |d,u,d\rangle = \left|\frac{1}{2},-\frac{1}{2}\right\rangle\ . \tag{B.12}$$

The isospin $1/2$ is also obtained from the addition $I_1 = 1 \oplus I_2 = \frac{1}{2}$. In particular

$$\begin{aligned} \left|\frac{1}{2},+\frac{1}{2}\right\rangle &= -\frac{1}{\sqrt{3}}\left|\frac{1}{2},+\frac{1}{2}\right\rangle|1,0\rangle + \sqrt{\frac{2}{3}}\left|\frac{1}{2},-\frac{1}{2}\right\rangle|1,1\rangle\ , \\ \left|\frac{1}{2},-\frac{1}{2}\right\rangle &= +\frac{1}{\sqrt{3}}\left|\frac{1}{2},-\frac{1}{2}\right\rangle|1,0\rangle - \sqrt{\frac{2}{3}}\left|\frac{1}{2},+\frac{1}{2}\right\rangle|1,-1\rangle\ . \end{aligned} \tag{B.13}$$

Translating these relations in terms of physical states (pions and nucleons),we obtain

$$\begin{aligned}\left|\frac{1}{2},+\frac{1}{2}\right\rangle &= -\frac{1}{\sqrt{3}}\left|p\right\rangle\left|\pi^0\right\rangle + \sqrt{\frac{2}{3}}\ \left|n\right\rangle\left|\pi^+\right\rangle\ , \\ \left|\frac{1}{2},-\frac{1}{2}\right\rangle &= +\frac{1}{\sqrt{3}}\left|n\right\rangle\left|\pi^0\right\rangle - \sqrt{\frac{2}{3}}\ \left|p\right\rangle\left|\pi^-\right\rangle\ . \end{aligned} \tag{B.14}$$

These results are used to project the nucleon-pion interpolating operator $\mathrm{O}_{N\pi}^{I,I_z}$ on the isospin I, I_z:

$$\mathrm{O}_{N\pi}^{1/2,\ +1/2} = -\frac{1}{\sqrt{3}}\ \mathrm{O}_p\ \mathrm{O}_{\pi^0} + \sqrt{\frac{2}{3}}\ \mathrm{O}_n\ \mathrm{O}_{\pi^+}\ , \tag{B.15}$$

$$\mathrm{O}_{N\pi}^{1/2,\ -1/2} = +\frac{1}{\sqrt{3}}\ \mathrm{O}_n\ \mathrm{O}_{\pi^0} - \sqrt{\frac{2}{3}}\ \mathrm{O}_p\ \mathrm{O}_{\pi^-}\ . \tag{B.16}$$

Analogously, the interpolating operators with isospin $3/2$ are also obtained from the addition $I_1 = 1 \oplus I_2 = \frac{1}{2}$:

$$\mathrm{O}_{N\pi}^{3/2,\ +3/2} = \mathrm{O}_p\ \mathrm{O}_{\pi^+}\ , \tag{B.17}$$

$$\mathrm{O}_{N\pi}^{3/2,\ +1/2} = \frac{2}{\sqrt{3}}\ \mathrm{O}_p\ \mathrm{O}_{\pi^0} + \frac{1}{\sqrt{3}}\ \mathrm{O}_n\ \mathrm{O}_{\pi^+}\ , \tag{B.18}$$

$$\mathrm{O}_{N\pi}^{3/2,\ -1/2} = \frac{2}{\sqrt{3}}\ \mathrm{O}_n\ \mathrm{O}_{\pi^0} + \frac{1}{\sqrt{3}}\ \mathrm{O}_p\ \mathrm{O}_{\pi^-}\ , \tag{B.19}$$

$$\mathrm{O}_{N\pi}^{3/2,\ -3/2} = \mathrm{O}_n\ \mathrm{O}_{\pi^-}\ . \tag{B.20}$$

The physical states corresponding to $I = 3/2$ are the Δ, which are decouplet baryons:

$$\Delta^{++} = \left|\frac{3}{2},+\frac{3}{2}\right\rangle, \qquad \Delta^{+} = \left|\frac{3}{2},+\frac{1}{2}\right\rangle\ , \qquad \Delta^{0} = \left|\frac{3}{2},-\frac{1}{2}\right\rangle\ , \qquad \Delta^{-} = \left|\frac{3}{2},-\frac{3}{2}\right\rangle\ . \tag{B.21}$$

APPENDIX

THREE

GROUP THEORY REMARKS

In the continuum, the theory of particles with spin 1 and 1/2 is related to the representation theory of $SO(3)$ and its double cover group $SU(2)$. On a hypercubic lattice, the spin is realised by the reduction of $SO(3)$ and $SU(2)$ with respect to the octahedral group O_h or its double cover ${}^2O_h$, respectively. The symmetry group of particles with integer spin (bosons) is O_h, while ${}^2O_h$ is for particles with half-integer spin (fermions). The crystallographic point group O_h is composed of 24 elements, split into five conjugacy classes $I, 3C_2, 8C_3, 6C_4, 6C_2'$. The notation is standard in crystallography: nC_m means a class of n elements of order m, i.e. each is an mth root of the identity. In Tab. I of [85], there are all the elements of the cubic group, parameterized by a rotation axis $\mathbf{n}^{(i)}$ and a rotation angle ω_i. Following loosely [124, 70], the number of Irreducible Representations (IRs hereafter) is equal to the number of conjugacy classes for finite groups. The five IRs of O_h are called A_1, A_2, E, T_1, and T_2, with dimensions 1, 1, 2, 3, 3, respectively. The irreducible representation A_1 describes spinless particles like the pions, and it will be mentioned in the following. Regarding the group ${}^2O_h$, it is constructed from O_h by adding a negative identity J for $\pm 2\pi$ rotations. This results in 48 elements, which are divided in eight conjugacy classes: I, J, $6C_4$, $8C_3$, $8C_6$, $6C_8$, $6C_8'$ and $12C_4'$. The IRs for this group are eight and in particular, they are A_1, A_2, E, T_1, and T_2 as for O_h, but additionally, there are G_1, G_2 and H. Thus, there are in total eight conjugacy classes I, J, $6C_4$, $8C_3$, $8C_6$, $6C_8$, $6C_8'$ and $12C_4'$. For example, a matrix representation of G_1 is obtained from Pauli σ matrices:

$$D(\mathbf{n},\omega)_{G_1} = e^{-i\mathbf{n}\cdot\frac{\sigma}{2}\omega} = I\cos\frac{\omega}{2} - i\sigma\cdot\mathbf{n}\,\sin\frac{\omega}{2}\,. \tag{C.1}$$

One may recognize this formula from quantum mechanics because it is used to transform spin 1/2 particles under rotations along the axis $\mathbf{n}$ by an angle ω. The matrix of eq. (C.1) is also known as the Wigner D-matrix for spin 1/2 and the irreducible representation G_1 is therefore relevant for describing e.g. electrons and nucleons.

Only total angular momenta $j = 0, 1/2, 1, 3/2$ correspond to single IRs, while $j \geq 2$ are described by two or more different IRs. In Tab. C.1, it is displayed the reduction of $SU(2)$ to ${}^2O_h$,

j	$\Gamma(\dim_\Gamma)$
0	$A_1(1)$
1/2	$G_1(2)$
1	$T_1(3)$
3/2	$H(4)$
2	$E(2) \oplus T_2(3)$
5/2	$G_2(2) \oplus H(4)$
3	$A_2(1) \oplus T_1(3) \oplus T_2(3)$
7/2	$G_1(2) \oplus G_2(2) \oplus H(4)$

Table C.1: Reduction of $SU(2)$ to ${}^2O_h$, up to $j = 7/2$

up to $j = 7/2$. The projection of an operator O onto a specific row r of a lattice irreducible representation Γ is

$$\mathrm{O}_{r,\Gamma} = \sum_{S_i \in G} T^{\Gamma}_{rr}(S_i)\Big(T(S_i)\,\mathrm{O}\,T^{-1}(S_i)\Big)\,, \tag{C.2}$$

where the sum is over all the elements S_i in the group G and the term in brackets represents the transformation of the original interpolating operator O under the element S_i. While the irreducible representation Γ is equivalent to the spin s of the particle in the continuum, its row r corresponds m_s component. In the case of rotations R and inversions I, the transformation properties of a single-hadron operator $\mathrm{O}_{s,m_s}(\mathbf{p})$ with momentum $\mathbf{p}$, spin s and m_s component are

$$\mathrm{O}_{s,m_s}(\mathbf{p}) \xrightarrow{R} R\,\mathrm{O}_{s,m_s}(\mathbf{p})\,R^{-1} = \sum_{m_s'} D^{s}_{m_s m_s'}(R^{-1})\,\mathrm{O}_{s,m_s'}(R\,\mathbf{p})\,, \tag{C.3}$$

$$\mathrm{O}_{s,m_s}(\mathbf{p}) \xrightarrow{I} I\,\mathrm{O}_{s,m_s}(\mathbf{p})\,I = (-1)^P\,\mathrm{O}_{s,m_s'}(-\mathbf{p})\,, \tag{C.4}$$

where $D^{s}_{m_s m_s'}(R^{-1})$ is the Wigner D-matrix ([143]) of spin s and rotation matrix R. In the case of a two-hadron interpolating operator $\mathrm{O} = \mathrm{O}_1\mathrm{O}_2$ like the nucleon-pion operator $\mathrm{O}_{N\pi}(\mathbf{p}_N;\mathbf{p}_\pi) = \mathrm{O}_N(\mathbf{p}_N)\mathrm{O}_\pi(\mathbf{p}_\pi)$, if we want to project it on the row r of the irreducible representation Γ with a total momentum $\mathbf{p}_{\text{tot}} = \mathbf{0}$, the group theory projection method reads

$$\mathrm{O}_{r,\Gamma}(\mathbf{p}_{\text{tot}} = \mathbf{0}) = \sum_{S_i \in G} T^{\Gamma}_{rr}(S_i)\Big(T(S_i)\,\mathrm{O}_1(\mathbf{p})\,T^{-1}(S_i)\Big)\Big(T(S_i)\,\mathrm{O}_2(-\mathbf{p})\,T^{-1}(S_i)\Big)\,. \tag{C.5}$$

Taking into example the projection of a nucleon-pion interpolating operator $\mathrm{O}_{N\pi} = \mathrm{O}_N\mathrm{O}_\pi$ on $m_s = \pm 1/2$ and $s = 1/2$ ($\Gamma = G_1$), the projection method of eq. (C.5) gives

$$(\mathrm{O}_{N\pi})^{G_1}_{m_s}(\mathbf{p}_{\text{tot}} = \mathbf{0}) = \sum_{S_i \in {}^2O_h} T^{G_1}_{m_s m_s}(S_i)\Big(T(S_i)\,\mathrm{O}_N\,T^{-1}(S_i)\Big)\Big(T(S_i)\,\mathrm{O}_\pi\,T^{-1}(S_i)\Big)\,. \tag{C.6}$$

In eq. (C.6) the sum is over the 48 elements that belong to the group ${}^2O_h$; each of them has a rotation axis $\mathbf{n}^{(i)}$ and a rotation angle ω_i (see Tab. II in [85]).

In particular, I recall that the transformation properties under rotations R and inversions I of the nucleon interpolating operator:

$$T(R)\ \mathrm{O}_{N,m_s}(\mathbf{p})\ T(R)^{-1} = \sum_{m_s'} D^{1/2}_{m_s m_s'}(R^{-1})\ \mathrm{O}_{N,m_s'}(R\,\mathbf{p})\,, \tag{C.7}$$

$$T(I)\ \mathrm{O}_{N,m_s}(\mathbf{p})\ T(I) = \mathrm{O}_{N,m_s}(-\mathbf{p}) \tag{C.8}$$

and the ones for the pion, which is a spinless pseudoscalar particle:

$$T(R)\ \mathrm{O}_{\pi}(\mathbf{p})\ T(R)^{-1} = \mathrm{O}_{\pi}(R\,\mathbf{p})\,, \tag{C.9}$$

$$T(I)\ \mathrm{O}_{\pi}(\mathbf{p})\ T(I) = -\mathrm{O}_{\pi}(-\mathbf{p})\,. \tag{C.10}$$

If we consider only unit momenta[1] for the nucleon and the pion, the projection in eq. (C.6) gives

$$\begin{aligned}(\mathrm{O}_{N\pi})^{G_1}_{m_s=\uparrow}(\mathbf{p}_{\mathrm{tot}}=\mathbf{0}) = &+\mathrm{O}_{N\downarrow}(-\mathbf{e_x})\ \mathrm{O}_{\pi}(\mathbf{e_x}) - \mathrm{O}_{N\downarrow}(\mathbf{e_x})\ \mathrm{O}_{\pi}(-\mathbf{e_x}) +\\ &- i\mathrm{O}_{N\downarrow}(-\mathbf{e_y})\ \mathrm{O}_{\pi}(\mathbf{e_y}) + i\mathrm{O}_{N\downarrow}(\mathbf{e_y})\ \mathrm{O}_{\pi}(-\mathbf{e_y}) +\\ &+\mathrm{O}_{N\uparrow}(-\mathbf{e_z})\ \mathrm{O}_{\pi}(\mathbf{e_z}) - \mathrm{O}_{N\uparrow}(\mathbf{e_z})\ \mathrm{O}_{\pi}(-\mathbf{e_z})\,,\end{aligned} \tag{C.11}$$

$$\begin{aligned}(\mathrm{O}_{N\pi})^{G_1}_{m_s=\downarrow}(\mathbf{p}_{\mathrm{tot}}=\mathbf{0}) = &+\mathrm{O}_{N\uparrow}(-\mathbf{e_x})\ \mathrm{O}_{\pi}(\mathbf{e_x}) - \mathrm{O}_{N\uparrow}(\mathbf{e_x})\ \mathrm{O}_{\pi}(-\mathbf{e_x}) +\\ &+ i\mathrm{O}_{N\uparrow}(-\mathbf{e_y})\ \mathrm{O}_{\pi}(\mathbf{e_y}) - i\mathrm{O}_{N\uparrow}(\mathbf{e_y})\ \mathrm{O}_{\pi}(-\mathbf{e_y}) +\\ &-\mathrm{O}_{N\downarrow}(-\mathbf{e_z})\ \mathrm{O}_{\pi}(\mathbf{e_z}) + \mathrm{O}_{N\downarrow}(\mathbf{e_z})\ \mathrm{O}_{\pi}(-\mathbf{e_z})\,.\end{aligned} \tag{C.12}$$

In a moving frame, the symmetries of the lattice with isotropic spatial extension L are further reduced to specific subgroups of O_h and ${}^2O_h$, whose elements S_i obey the relation

$$S_i\ \mathbf{d} = \mathbf{d}\,, \tag{C.13}$$

where $\mathbf{d}$ is the boost direction, which is related to the total momentum of the single- or multi-hadron operator $\mathbf{p}_{\mathrm{tot}}$ by:

$$\mathbf{p}_{\mathrm{tot}} = \frac{2\pi}{L}\,\mathbf{d}\,. \tag{C.14}$$

The groups of elements that satisfy eq. (C.13) are called little groups.

In Tab. C.2, there are the respective little groups of ${}^2O_h$ for each specific $\mathbf{d}$. In Tab. III of [85], there are also the little groups of O_h and rotations that satisfy[2] $S_i\ \mathbf{d} = -\mathbf{d}$.

---

[1] The notation is the following: $\mathbf{e_x} = \frac{2\pi}{L}(1,0,0)$, $\mathbf{e_y} = \frac{2\pi}{L}(0,1,0)$ and $\mathbf{e_z} = \frac{2\pi}{L}(0,0,1)$, like in the main text.

[2] For equal masses, the system is symmetric under $\mathbf{d} \to -\mathbf{d}$ and the little groups consist of elements that satisfy $S_i\ \mathbf{d} = \pm\mathbf{d}$.

Group	$\mathbf{d}$	Little Group	$R_i\ \mathbf{d} = \mathbf{d}$
^2O_h	(0, 0, 1)	$^2C_{4v}$	$\{R_i \mid i = 1, 4, 7, 10, 13, 16, 19, 48\}$
	(1, 1, 0)	$^2C_{2v}$	$\{R_i \mid i = 1, 38, 44, 48\}$
	(1, 1, 1)	$^2C_{3v}$	$\{R_i \mid i = 1, 20, 24, 28, 32, 48\}$

Table C.2: Rotations R_i that obey the condition $R_i\ \mathbf{d} = \mathbf{d}$

Let us consider a generic moving frame $\mathbf{d}$ and the nucleon-pion system with total momentum $\mathbf{p}_{\text{tot}} = \frac{2\pi}{L}\mathbf{d}$. We perform the momentum projection via the Fourier transform:

$$(\mathrm{O}_{N\pi})_{m_s}(\mathbf{p}_{\text{tot}}) = \sum_{\mathbf{x},\mathbf{y}} e^{-i\mathbf{p}_{\text{tot}}\cdot\mathbf{x}} e^{-i\mathbf{p}_\pi(\mathbf{y}-\mathbf{x})} \mathrm{O}_{N,m_s}(\mathbf{x},t)\mathrm{O}_\pi(\mathbf{y},t)\ . \tag{C.15}$$

The reason why we employ this Fourier transform is because it simplifies the calculations as we can apply the relation of eq. (C.13) when we transform the operator under rotations or inversions. Indeed, calling $\mathscr{L}$ the little group,

$$(\mathrm{O}_{N\pi})^{G_1}_{m_s}(\mathbf{p}_{\text{tot}} = \mathbf{0}) = \sum_{R_i\in\mathscr{L}} T^{G_1}_{m_s m_s}(R_i)\Big(\sum_{m_s'} D^s_{m_s m_s'}(R_i)\ \mathrm{O}_{N,m_s'}(\mathbf{p}_N')\Big)\mathrm{O}_\pi(\mathbf{p}_\pi')\ , \tag{C.16}$$

with $\mathbf{p}_N' = \mathbf{p}_{\text{tot}} - R_i\ \mathbf{p}_\pi$ and $\mathbf{p}_\pi' = R_i\ \mathbf{p}_\pi$. For example, in the case of $\mathbf{d} = (0,0,1) = \mathbf{e_z}$, the little group is $^2C_{4v}$, which is composed of eight elements (see Tab. C.2). The projection onto the lattice irreducible representation reads

$$(\mathrm{O}_{N\pi})^{G_1}_{m_s}(\hat{e}_z) = \sum_{R_i\in{}^2C_{4v}} T^{G_1}_{m_s m_s}(R_i)\Big(\sum_{m_s'} D^s_{m_s m_s'}(R_i^{-1})\ \mathrm{O}_{N,m_s'}(\mathbf{p}_N')\Big)\mathrm{O}_\pi(\mathbf{p}_\pi')\ , \tag{C.17}$$

which gives the two possibilities

$$(\mathrm{O}_{N\pi})^{G_1,1}_{m_s}(\hat{e}_z) = 4\ \mathrm{O}_{N,m_s}(\mathbf{e_z})\ \mathrm{O}_\pi(\mathbf{e_0})\ , \tag{C.18}$$

$$(\mathrm{O}_{N\pi})^{G_1,2}_{m_s}(\hat{e}_z) = 4\ \mathrm{O}_{N,m_s}(\mathbf{e_0})\ \mathrm{O}_\pi(\mathbf{e_z})\ . \tag{C.19}$$

APPENDIX

FOUR

WICK CONTRACTIONS

In this Appendix, I review the Wick contractions of quarks and their application to standard nucleon three-point functions and to nucleon to nucleon-pion three-point functions. The calculations are cross checked using the Mathematica package presented in [66] and we localise the interpolating operator at the source position $0 = (\mathbf{0}, 0)$ for more clarity.

Using the nucleon interpolating operators

$$\mathrm{O}_{N,\gamma}(x) = \epsilon^{abc} \left(d^a_\alpha(x)\, \tilde{C}_{\alpha\beta}\, u^b_\beta(x) \right) q^c_\gamma(x) \,, \tag{D.1}$$

$$\bar{\mathrm{O}}_{N,\bar{\gamma}}(0) = \epsilon^{\bar{a}\bar{b}\bar{c}}\, \bar{q}^{\bar{c}}_{\bar{\gamma}}(0) \left(\bar{u}^{\bar{b}}_{\bar{\beta}}(0)\, \tilde{C}_{\bar{\beta}\bar{\alpha}}\, \bar{d}^{\bar{a}}_{\bar{\alpha}}(0) \right) , \tag{D.2}$$

where $q = u, d$ determines the isospin component $N = p, n$ and the intermediate current at a space-time position $z = (\mathbf{z}, \tau)$

$$\mathscr{J}_q \;=\; \bar{q}^d_{\bar{\epsilon}}(z)\, \Gamma^{\bar{\delta}\delta}\, q^d_\epsilon(z) \,, \qquad\qquad \text{with} \qquad q = u, d \,, \tag{D.3}$$

the proton three-point functions are

$$C^{p+\mathscr{J}_q \to p}_{3pt}(x, z, 0) = \mathbb{P}^k_{\bar{\gamma}\gamma} \,\langle\, \mathrm{O}_{p,\gamma}(x)\, \mathscr{J}_q(z)\, \bar{\mathrm{O}}_{p,\bar{\gamma}}(0) \,\rangle \,, \tag{D.4}$$

where $\mathbb{P}^k$ is the spin-parity projector. In particular, by employing the proton operators of eqs. (D.1), (D.2) and using the Wick's theorem, we obtain

$$\begin{aligned} C^{p+\mathscr{J}_d \to p}_{3pt}(x, z, 0) = \;& \epsilon^{abc}\, \epsilon^{\bar{a}\bar{b}\bar{c}}\, \mathbb{P}^k_{\bar{\gamma}\gamma}\, \Gamma_{\bar{\delta}\delta}\, \tilde{C}_{\alpha\beta}\, \tilde{C}_{\bar{\beta}\bar{\alpha}} \left[D^{d\bar{a}}_{\delta\bar{\alpha}}(x,0) D^{ad}_{\alpha\bar{\delta}}(x,0) - D^{dd}_{\delta\bar{\epsilon}}(z,z) D^{a\bar{a}}_{\alpha\bar{\alpha}}(x,0) \right] \times \\ & \times \left[U^{c\bar{c}}_{\gamma\bar{\gamma}}(x,0) U^{b\bar{b}}_{\beta\bar{\beta}}(x,0) - U^{c\bar{b}}_{\gamma\bar{\beta}}(x,0) U^{b\bar{c}}_{\beta\bar{\gamma}}(x,0) \right] . \end{aligned} \tag{D.5}$$

$$\begin{aligned}
C_{3pt}^{p+\mathscr{J}_u\to p}(x,z,0) = \; & \epsilon^{abc}\,\epsilon^{\bar a\bar b\bar c}\,\mathbb{P}^k_{\bar\gamma\gamma}\,\Gamma^{\bar\delta\delta}\,\tilde C_{\alpha\beta}\,\tilde C_{\bar\beta\bar\alpha}\,D^{a\bar a}_{\alpha\bar\alpha}(x,0)\times \\
& \times\Big\{-U^{dd}_{\delta\bar\delta}(z,z)\Big[U^{c\bar c}_{\gamma\bar\gamma}(x,0)U^{b\bar b}_{\beta\bar\beta}(x,0)-U^{c\bar b}_{\gamma\bar\beta}(x,0)U^{b\bar c}_{\beta\bar\gamma}(x,0)\Big]+ \\
& +U^{d\bar c}_{\delta\bar\gamma}(z,0)\Big[U^{cd}_{\gamma\bar\delta}(x,z)U^{b\bar b}_{\beta\bar\beta}(x,0)-U^{c\bar b}_{\gamma\bar\beta}(x,0)U^{bd}_{\beta\bar\delta}(x,z)\Big]+ \\
& -U^{d\bar b}_{\delta\bar\beta}(z,0)\Big[U^{cd}_{\gamma\bar\delta}(x,z)U^{b\bar c}_{\beta\bar\gamma}(x,0)-U^{c\bar c}_{\gamma\bar\gamma}(x,0)U^{bd}_{\beta\bar\delta}(x,0)\Big]\Big\}\,.
\end{aligned} \tag{D.6}$$

In $C_{3pt}^{p+\mathscr{J}_d\to p}$, there are 2 pairs of u-quarks and 2 pairs of d-quarks to consider and the possible Wick contractions correspond to the permutations of pairs: 2! × 2!, as it results from eq. (D.5). In $C_{3pt}^{p+\mathscr{J}_u\to p}$, there are instead 3 pairs of u-quarks and 1 pair of d-quarks, so that the possible Wick contractions are: 3! × 1!. The standard results obtained in eqs. (D.5), (D.6) are checked against a Mathematica library that performs such calculations (see [66]).

However, in the isospin symmetry limit, where $U^{ab}_{\alpha\beta}(z,y)=D^{ab}_{\alpha\beta}(z,y)$, the disconnected contribution in eqs. (D.6)-(D.5), which are proportional to $D^{ee}_{\epsilon\bar\epsilon}(z,z)$ are equal and opposite, so that for an intermediate current $\mathscr{J}_{u-d}(z)=\bar u^d_{\bar\delta}(z)\Gamma^{\bar\delta\delta}\;u^d_\delta(z))-\bar d^d_{\bar\delta}(z)\Gamma^{\bar\delta\delta}\;d^d_\delta(z))$, the three-point function reads

$$\begin{aligned}
C_{3pt}^{p+\mathscr{J}_{u-d}\to p}(x,z,0) = \; & \epsilon^{abc}\,\epsilon^{\bar a\bar b\bar c}\,\mathbb{P}^k_{\bar\gamma\gamma}\,\Gamma_{\bar\delta\delta}\,\tilde C_{\alpha\beta}\,\tilde C_{\bar\beta\bar\alpha}\times \\
& \times\Big\{D^{a\bar a}_{\alpha\bar\alpha}(x,0)\Big[+U^{d\bar c}_{\delta\bar\gamma}(z,0)\Big(U^{cd}_{\gamma\bar\delta}(x,z)U^{b\bar b}_{\beta\bar\beta}(x,0)-U^{c\bar b}_{\gamma\bar\beta}(x,0)U^{bd}_{\beta\bar\delta}(x,z)\Big)+ \\
& -U^{d\bar b}_{\delta\bar\beta}(z,0)\Big(U^{cd}_{\gamma\bar\delta}(x,z)U^{b\bar c}_{\beta\bar\gamma}(x,0)\Big)\Big] \\
& +D^{d\bar a}_{\delta\bar\alpha}(x,0)D^{ad}_{\alpha\bar\delta}(x,0)U^{c\bar b}_{\gamma\bar\beta}(x,0)U^{b\bar c}_{\beta\bar\gamma}(x,0)\Big\}\,,
\end{aligned}$$

where I have also used the antisymmetric properties of the color tensors and of the charge conjugation matrix (see eq. (A.23)). A comparison with the three-point function $C_{3pt}^{p+\mathscr{J}_-\to p}(x,z,0)$ in eq. (3.33), makes it evident that in the isospin symmetric limit and with this choice of nucleon interpolators, $C_{3pt}^{p+\mathscr{J}_-\to p}(x,z,0)=C_{3pt}^{p+\mathscr{J}_-\to p}(x,z,0)$, where $\mathscr{J}_-(z)=\bar d^d_{\bar\delta}(z)\;\Gamma^{\bar\delta\delta}\;u^d_\delta(z)$. This result is also confirmed by the Wigner-Eckart theorem.
Here I list the results of the new processes that I have studied:

$$\begin{aligned}
C_{3pt}^{p+\mathscr{J}_-\to p\pi^-}(x,y,z) &= \mathbb{P}^k_{\bar\gamma\gamma}\,\langle\, \mathrm{O}_{p,\gamma}(x)\;\mathrm{O}_{\pi^-}(y)\;\mathscr{J}_-(z)\;\bar{\mathrm{O}}_{p,\bar\gamma}(0)\,\rangle \\
&= C_{3pt,\,A}^{p+\mathscr{J}_-\to p\pi^-}+C_{3pt,\,B}^{p+\mathscr{J}_-\to p\pi^-}+C_{3pt,\,C}^{p+\mathscr{J}_-\to p\pi^-}+C_{3pt,\,D}^{p+\mathscr{J}_-\to p\pi^-}\;,
\end{aligned} \tag{D.7}$$

$$\begin{aligned}
C_{3pt,\,A}^{p+\mathscr{J}_-\to p\pi^-} = \; & \epsilon^{abc}\,\epsilon^{\bar a\bar b\bar c}\,\mathbb{P}^k_{\bar\gamma\gamma}\,\Gamma_{\bar\delta\delta}\,\tilde C_{\alpha\beta}\,\tilde C_{\bar\beta\bar\alpha}\,\gamma^5_{\epsilon\epsilon'}\,D^{e\bar a}_{\epsilon\bar\alpha}(y,0)\;D^{ad}_{\alpha\delta}(x,z)\times \\
& \times\Big[U^{de}_{\delta\bar\epsilon}(z,y)\Big(U^{c\bar c}_{\gamma\bar\gamma}(x,0)\;U^{b\bar b}_{\beta\bar\beta}(x,0)-U^{c\bar b}_{\gamma\bar\beta}(x,0)\;U^{b\bar c}_{\beta\bar\gamma}(x,0)\Big)\Big]\,.
\end{aligned} \tag{D.8}$$

$$\begin{aligned} C^{p+\mathscr{J}_-\to p\pi^-}_{3pt,\,B} =\ & \epsilon^{abc}\epsilon^{\bar a\bar b\bar c}\ \tilde C^{\alpha\beta}\ \tilde C^{\bar\beta\bar\alpha}\ P_{\bar\gamma\gamma}\,\Gamma_{\bar\delta\delta}\,\gamma^5_{\bar\epsilon\epsilon}\ D^{e\bar a}_{\epsilon\bar\alpha}(y,0)\ D^{ad}_{\alpha\bar\delta}(x,z)\times \\ & \times\Big[-U^{d\bar c}_{\delta\bar\gamma}(z,0)\Big(\ U^{ce}_{\gamma\bar\epsilon}(x,y)\ U^{b\bar b}_{\beta\bar\beta}(x,0)-U^{c\bar b}_{\gamma\bar\beta}(x,0)\ U^{be}_{\beta\bar\epsilon}(x,y)\ \Big)+ \\ & +U^{d\bar b}_{\delta\bar\beta}(z,0)\Big(\ U^{ce}_{\gamma\bar\epsilon}(x,y)\ U^{b\bar c}_{\beta\bar\gamma}(x,0)-U^{c\bar c}_{\gamma\bar\gamma}(x,0)\ U^{be}_{\beta\bar\epsilon}(x,y)\ \Big)\Big]\ . \end{aligned} \tag{D.9}$$

$$\begin{aligned} C^{p+\mathscr{J}_-\to p\pi^-}_{3pt,\,C} =\ & \epsilon^{abc}\epsilon^{\bar a\bar b\bar c}\ \tilde C^{\alpha\beta}\ \tilde C^{\bar\beta\bar\alpha}\ P_{\bar\gamma\gamma}\,\Gamma_{\delta\delta'}\,\gamma^5_{\bar\epsilon\epsilon}\ D^{ed}_{\epsilon\bar\delta}(y,z)\ D^{a\bar a}_{\alpha\bar\alpha}(x,0) \\ & \Big[+U^{d\bar c}_{\delta\bar\gamma}(z,0)\Big(\ U^{ce}_{\gamma\bar\epsilon}(x,y)\ U^{b\bar b}_{\beta\bar\beta}(x,0)-\ U^{be}_{\beta\bar\epsilon}(x,y)\ U^{c\bar b}_{\gamma\bar\beta}(x,0)\Big) \\ & -U^{d\bar b}_{\delta\bar\beta}(z,0)\Big(\ U^{ce}_{\gamma\bar\epsilon}(x,y)\ U^{b\bar c}_{\beta\bar\gamma}(x,0)\ -\ U^{be}_{\beta\bar\epsilon}(x,y)\ U^{c\bar c}_{\gamma\bar\gamma}(x,0)\ \Big)\Big]\ . \end{aligned} \tag{D.10}$$

$$\begin{aligned} C^{p+\mathscr{J}_-\to p\pi^-}_{3pt,\,D} =\ & \epsilon^{abc}\ \epsilon^{\bar a\bar b\bar c}\ \tilde C^{\alpha\beta}\ \tilde C^{\bar\beta\bar\alpha}\ \mathbb{P}^k_{\bar\gamma\gamma}\,\Gamma_{\bar\delta\delta}\,\gamma^5_{\bar\epsilon\epsilon}\ D^{ed}_{\epsilon\bar\delta}(y,z)\ D^{a\bar a}_{\alpha\bar\alpha}(x,0)\times \\ & \times\ U^{de}_{\delta\bar\epsilon}(z,y)\Big(\ U^{c\bar c}_{\gamma\bar\gamma}(x,0)\ U^{b\bar b}_{\beta\bar\beta}(x,0)-U^{c\bar b}_{\gamma\bar\beta}(x,0)\ U^{b\bar c}_{\beta\bar\gamma}(x,0)\ \Big)\ . \end{aligned} \tag{D.11}$$

$$\begin{aligned} C^{p+\mathscr{J}_-\to n\pi^0}_{3pt}(x,y,z) &= \mathbb{P}^k_{\bar\gamma\gamma}\ \langle\ \mathrm{O}_{n,\gamma}(x)\ \mathrm{O}_{\pi^0}(y)\ \mathscr{J}^-(z)\ \bar{\mathrm{O}}_{p,\bar\gamma}(0)\ \rangle \\ &= \frac{1}{\sqrt2}\Big(C^{p+\mathscr{J}^-\to n\pi^0}_{3pt,\,A}+C^{p+\mathscr{J}^-\to n\pi^0}_{3pt,\,B}+C^{p+\mathscr{J}^-\to n\pi^0}_{3pt,\,C}\Big)\ . \end{aligned} \tag{D.12}$$

$$\begin{aligned} C^{p+\mathscr{J}_-\to n\pi^0}_{3pt,\,A} =\ & \epsilon^{abc}\ \epsilon^{\bar a\bar b\bar c}\ \mathbb{P}^k_{\bar\gamma\gamma}\,\Gamma_{\bar\delta\delta}\ \tilde C_{\alpha\beta}\ \tilde C_{\bar\beta\bar\alpha}\ \gamma^5_{\bar\epsilon\epsilon}\ \Big(D^{cd}_{\gamma\bar\delta}(x,z)D^{a\bar a}_{\alpha\bar\alpha}(x,0)-D^{c\bar a}_{\gamma\bar\alpha}(x,0)D^{ad}_{\alpha\bar\delta}(x,z)\Big)\times \\ & \times\ U^{de}_{\delta\bar\epsilon}(z,y)\Big(U^{e\bar c}_{\epsilon\bar\gamma}(y,0)U^{b\bar b}_{\beta\bar\beta}(x,0)-U^{e\bar b}_{\epsilon\bar\beta}(y,0)U^{b\bar c}_{\beta\bar\gamma}(x,0)\Big)\ . \end{aligned} \tag{D.13}$$

$$\begin{aligned} C^{p+\mathscr{J}_-\to n\pi^0}_{3pt,\,B} =\ & +\epsilon^{abc}\epsilon^{\bar a\bar b\bar c}\ \tilde C_{\alpha\beta}\ \tilde C_{\bar\beta\bar\alpha}\ \mathbb{P}_{\bar\gamma\gamma}\,\Gamma_{\bar\delta\delta}\ \gamma^5_{\bar\epsilon\epsilon}\Big(D^{cd}_{\gamma\bar\delta}(x,z)\ D^{a\bar a}_{\alpha\bar\alpha}(x,0)-D^{c\bar a}_{\gamma\bar\alpha}(x,0)\ D^{ad}_{\alpha\bar\delta}(x,z)\Big)\times \\ & \times\ U^{be}_{\beta\bar\epsilon}(x,y)\Big(\ U^{d\bar c}_{\delta\bar\gamma}(z,0)\ U^{e\bar b}_{\epsilon'\bar\beta}(y,0)-U^{d\bar b}_{\delta\bar\beta}(z,0)\ U^{e\bar c}_{\epsilon'\bar\gamma}(y,0)\Big)+ \\ & -\epsilon^{abc}\epsilon^{\bar a\bar b\bar c}\ \tilde C_{\alpha\beta}\ \tilde C_{\bar\beta\bar\alpha}\mathbb{P}_{\bar\gamma\gamma}\,\Gamma_{\bar\delta\delta}\ \gamma^5_{\bar\epsilon\epsilon}\Big(U^{d\bar b}_{\delta'\bar\beta}(z,0)\ U^{b\bar c}_{\beta\bar\gamma}(x,0)-U^{d\bar c}_{\delta'\bar\gamma}(z,0)\ U^{b\bar b}_{\beta\bar\beta}(x,0)\Big)\times \\ & \times\ D^{e\bar a}_{\epsilon\bar\alpha}(y,0)\Big(D^{ce}_{\gamma\bar\epsilon}(x,y)\ D^{ad}_{\alpha\delta}(x,z)-D^{cd}_{\gamma\bar\delta}(x,z)\ D^{ae}_{\alpha\bar\delta}(x,y)\Big)\ . \end{aligned} \tag{D.14}$$

$$\begin{aligned} C^{p+\mathscr{J}_-\to n\pi^0}_{3pt,\,C} =\ & -\epsilon^{abc}\epsilon^{\bar a\bar b\bar c}\ \tilde C_{\alpha\beta}\ \tilde C_{\bar\beta\bar\alpha}\ \ \mathbb{P}_{\bar\gamma\gamma}\,\Gamma_{\bar\delta\delta}\ \gamma^5_{\bar\epsilon\epsilon}\Big(\ U^{d\bar b}_{\delta\bar\beta}(z,0)\ U^{b\bar c}_{\beta\bar\gamma}(x,0)-U^{d\bar c}_{\delta\bar\gamma}(z,0)\ U^{b\bar b}_{\beta\bar\beta}(x,0)\ \Big) \\ & \Big[\ -D^{ed}_{\epsilon\bar\delta}(y,z)\Big(\ D^{ce}_{\gamma\bar\epsilon}(x,y)\ D^{a\bar a}_{\alpha\bar\alpha}(x,0)-D^{c\bar a}_{\gamma\bar\alpha}(x,0)\ D^{ae}_{\alpha\bar\epsilon}(x,y)\ \Big)\Big]\ . \end{aligned} \tag{D.15}$$

In addition, there are disconnected loops, that in the isospin symmetry limit cancel like in the case of $C^{p+\mathscr{J}_{u-d}\to p}_{3pt}(x,z,0)$.

APPENDIX

FIVE

IMPLEMENTATION OF CORRELATION FUNCTIONS WITH CHROMA

This additional and rather technical Appendix is about the sequential method applied for the processes $p+\mathscr{J}_- \to n+\pi^0$ and $p+\mathscr{J}_- \to p+\pi^-$. In the following, I use CHROMA and GPT notation for the definition of functions like $quarkContractXY$, $traceColor$ and $traceSpin$.

For example, given 2 propagator objects $D^{ab}_{\alpha\beta}(x,0)$ and $D^{b\bar{b}}_{\alpha\bar{\beta}}(x,0)$, with 3 × 3 different color indices (a,b and $\bar{a},\bar{b}$) and 4 × 4 different spin indices (α,β and $\bar{\alpha},\bar{\beta}$), we can compute some the contraction

$$G^{\bar{c}c}_{\beta\bar{\beta}}(x,0) \equiv \epsilon^{abc}\epsilon^{\bar{a}\bar{b}\bar{c}}\, D^{a\bar{a}}_{\alpha\beta}(x,0)\, D^{b\bar{b}}_{\alpha\bar{\beta}}(x,0) = quarkContract13\Big(D(x,0),D(x,0)\Big)\,, \tag{E.1}$$

with $quarkContract13$ being the routine implemented in CHROMA or GPT, in order to do the contraction of the 1^{st} Dirac index with the 3^{rd} one.

The other contraction routines are also implemented in CHROMA and GPT (see). I will use the shorthand notation:

- $quarkContractXY = qCXY$;
- $\tilde{C} = C\gamma^5$;
- $(\cdot)^{T_D} = transposeSpin()$, it interchanges the Dirac indices.

E.1 $p+\mathscr{J}_d \to p$

In the following, I remove the detailed notation from C_{3pt} and the symbol of the sum $\sum$ in the Fourier Transform for brevity. The expression for the three-point function is

$$C_{3pt} = e^{i\mathbf{q}\cdot\mathbf{z}}\mathrm{Tr}\Big\{\Big(\gamma_5\, S^\dagger(z,0)\,\gamma_5\Big)\,\Gamma\, D(z,0)\Big\}\,, \tag{E.2}$$

where the sequential propagator $S(x,0)$ is obtained from the inversion of the sum of the following sequential sources:

$$S(z,0) = \; e^{i\mathbf{q}\cdot\mathbf{z}}\, D(z,x)\, \gamma_5 \big[\tilde{S}^{p\to p}_{\bar{d}d}(x,0)\big]^{\dagger}\, \gamma_5\,, \tag{E.3}$$

with $\tilde{S}^{p\to p}_{\bar{d}d}(x,0)$ being the proton-to-proton sequential source with a $\bar{d}d$-current, defined by

$$\tilde{S}^{p\to p}_{\bar{d}d}(x,0) = \tilde{S}_1(x,0) + \tilde{S}_2(x,0) \tag{E.4}$$

and

$$\tilde{S}_1(x,0) = \big[\; qC12\big(\, U * P\,,\; \tilde{C} * U * \tilde{C}\,\big)\,\big]^{T_D}\,, \tag{E.5}$$

$$\tilde{S}_2(x,0) = qC14\big(\, P * U * \tilde{C}\,,\; \tilde{C} * U\,\big)\,. \tag{E.6}$$

E.2 $p + \mathscr{J}_u \to p$

The expression for the three-point function is

$$C_{3pt}(\mathbf{p}', \mathbf{q}; t, \tau) = e^{i\mathbf{q}\cdot\mathbf{z}}\mathrm{Tr}\Big\{\Big(\gamma_5\; S^{\dagger}(z,0)\; \gamma_5\Big)\,\Gamma\; U(z,0)\Big\}\,, \tag{E.7}$$

where the sequential propagator $S(x,0)$ is obtained from the inversion of the sum of the following sequential sources:

$$S(z,0) = \; e^{i\mathbf{q}\cdot\mathbf{z}}\, U(z,x)\, \gamma_5 \big[\tilde{S}^{p\to p}_{\bar{d}d}(x,0)\big]^{\dagger}\, \gamma_5\,, \tag{E.8}$$

with $\tilde{S}^{p\to p}_{\bar{d}d}(x,0)$ being the proton-to-proton sequential source with a $\bar{d}d$-current, defined by

$$\tilde{S}^{p\to p}_{\bar{u}u}(x,0) = \tilde{S}_1(x,0) + \tilde{S}_2(x,0) + \tilde{S}_3(x,0) + \tilde{S}_4(x,0) \tag{E.9}$$

and

$$\tilde{S}_1 = -TraceSpin\big[\; qC24(\, U * \tilde{C},\; \tilde{C} * D\,)\;\big] * \mathbb{P}\,, \tag{E.10}$$

$$\tilde{S}_2 = -\mathbb{P} * qC24(\, D * \tilde{C},\; \tilde{C} * U\,)\,, \tag{E.11}$$

$$\tilde{S}_3 = qC13(\, \tilde{C} * D * \tilde{C},\; U * \mathbb{P}\,)\,, \tag{E.12}$$

$$\tilde{S}_4 = \big[\; qC12\big(\, U * P\,,\; \tilde{C} * U * \tilde{C}\,\big)\,\big]^{T_D}\,. \tag{E.13}$$

E.3 $p + \mathscr{J}_- \to n$

The expression for the three-point function is

$$C_{3pt}(x,z,0) = e^{i\mathbf{q}\cdot\mathbf{z}}\ \mathrm{Tr}\Big\{\big(\ \gamma_5\ S^\dagger(z,0)\ \gamma_5\ \big)\ \Gamma_\mu\ U(z,0)\Big\}\ .$$

Therefore

$$S(z,0)\ =\ e^{i\mathbf{p}'_N\cdot\mathbf{x}} D(z,x)\gamma_5\ \big[\ \tilde{S}^{p\to n}(x,0)\ \big]^\dagger\ \gamma_5\ , \tag{E.14}$$

with $\tilde{S}^{p\to n}(x,0)$ being the proton-to-neutron sequential source that is defined by the sum of four pieces, i.e.

$$\tilde{S}^{p\to n}(x,0) = \tilde{S}_1(x,0) + \tilde{S}_2(x,0) + \tilde{S}_3(x,0) + \tilde{S}_4(x,0) \tag{E.15}$$

and

$$\tilde{S}_1 = -TraceSpin\big[\ qC24(\ U*\tilde{C},\ \tilde{C}*D\ )\ \big]*\mathbb{P}\ , \tag{E.16}$$
$$\tilde{S}_2 = -\mathbb{P}*qC24(\ D*\tilde{C},\ \tilde{C}*U\ )\ , \tag{E.17}$$
$$\tilde{S}_3 = qC13(\ \tilde{C}*D*\tilde{C},\ U*\mathbb{P}\ )\ , \tag{E.18}$$
$$\tilde{S}_4 = -qC14(\ \mathbb{P}*D*\tilde{C},\ \tilde{C}*U\ )\ . \tag{E.19}$$

E.4 $p + \mathscr{J}_- \to n + \pi^0$

This process is represented in Fig. 4.2.

A-like

$$C_{3pt}(x,y,z) =\ e^{i\mathbf{q}\cdot\mathbf{z}}\ \mathrm{Tr}\Big\{\big(\ \gamma_5\ S_2^\dagger(z,0)\ \gamma_5\ \big)\ \Gamma_\mu\ S_1(z,0)\Big\}\ , \tag{E.20}$$
$$S_1(z,0) =\ e^{-i\mathbf{p}'_\pi\cdot\mathbf{y}}\ U(z,y)\ \gamma_5\ U(y,0)\ , \tag{E.21}$$
$$\begin{aligned} S_2(z,0) =&\ e^{i\mathbf{p}'_N\cdot\mathbf{x}}\ D(z,x)\ \gamma_5\ \Big[\ \tilde{S}_1^\dagger(x,0)+\tilde{S}_2^\dagger(x,0)+\tilde{S}_3^\dagger(x,0)+\tilde{S}_4^\dagger(x,0)\ \Big]\gamma_5 \\ =&\ e^{i\mathbf{p}'_N\cdot\mathbf{x}}\ D(z,x)\ \gamma_5\ \Big[\tilde{S}^{p\to n}(x,0)\Big]^\dagger\ \gamma_5\ , \end{aligned} \tag{E.22}$$

$$\tilde{S}_1(x,0) = -TraceSpin\Big[qC24(\ D(x,0)*\tilde{C}\ ,\ \tilde{C}*U(x,0)\ )\Big]*\mathbb{P}\ , \tag{E.23}$$
$$\tilde{S}_2(x,0) = -\mathbb{P}*qC24(\ D(x,0)*\tilde{C}\ ,\ \tilde{C}*U(x,0)\ )\ , \tag{E.24}$$
$$\tilde{S}_3(x,0) =\ qC13(\ \tilde{C}*D(x,0)*\tilde{C}\ ,\ U(x,0)*\mathbb{P}\ )\ , \tag{E.25}$$
$$\tilde{S}_4(x,0) = -qC14(\ \mathbb{P}*D(x,0)*\tilde{C}\ ,\ \tilde{C}*U(x,0)\ )\ , \tag{E.26}$$

The sequential source for $S_2(z,0)$ is equivalent to the sequential source for the standard nucleon three-point function $p + \mathscr{J}_- \to n$.

B-like

The neutral pion is $\pi^0 = \frac{1}{\sqrt{2}}(\bar{u}\gamma^5 u - \bar{d}\gamma^5 d)$. We divide this expression in two terms: one part coming from $\bar{u}\gamma^5 u$ and the other from $-\bar{d}\gamma^5 d$.
The term resulting from $\bar{u}\gamma^5 u$ is

$$C_{3pt} = e^{i\mathbf{q}\cdot\mathbf{z}}\ \mathrm{Tr}\Big\{\big(\gamma_5\, S_2^{\dagger}(z,0)\,\gamma_5\big)\,\Gamma_\mu\, U(z,0)\Big\}\,, \tag{E.27}$$

$$S_1(x,0) = e^{-i\mathbf{p}'_\pi\cdot\mathbf{y}}\, D(x,y) * \gamma_5 * D(y,0)\,, \tag{E.28}$$

$$S_2(z,0) = e^{i\mathbf{p}'_N\cdot\mathbf{x}}\, D(z,x) * \gamma_5 \left[\tilde{S}_{B_1}(x,0)\right]^{\dagger} \gamma_5\,, \tag{E.29}$$

$$\tilde{S}_{B_1}(x,0) = \tilde{S}_1(x,0) + \tilde{S}_2(x,0) + \tilde{S}_3(x,0) + \tilde{S}_4(x,0)\,, \tag{E.30}$$

$$\tilde{S}_1(x,0) = -TraceSpin\big[qC24\big(\,D(x,0) * \tilde{C},\ \tilde{C} * S_1(x,0)\,\big)\big] * \mathbb{P}\,, \tag{E.31}$$

$$\tilde{S}_2(x,0) = -\mathbb{P} * qC24(\,D(x,0) * \tilde{C}\,,\ \tilde{C} * S_1(x,0)\,)\,, \tag{E.32}$$

$$\tilde{S}_3(x,0) = qC13(\,\tilde{C} * D(x,0) * \tilde{C}\,,\ S_1(x,0) * \mathbb{P}\,)\,, \tag{E.33}$$

$$\tilde{S}_4(x,0) = -qC14(\,\mathbb{P} * D(x,0) * \tilde{C}\,,\ \tilde{C} * S_1(x,0)\,)\,. \tag{E.34}$$

The term resulting from $-\bar{d}\gamma^5 d$ is

$$C_{3pt}(x,y,z) = e^{i\mathbf{q}\cdot\mathbf{z}}\ \mathrm{Tr}\Big\{\big(\gamma_5\, S_2^{\dagger}(z,0)\,\gamma_5\big)\,\Gamma_\mu\, U(z,0)\Big\}\,, \tag{E.35}$$

$$S_1(x,0) = e^{-i\mathbf{p}'_\pi\cdot\mathbf{y}}\, D(x,y) * \gamma_5 * D(y,0)\,, \tag{E.36}$$

$$S_2(z,0) = e^{i\mathbf{p}'_N\cdot\mathbf{x}}\, D(z,x) * \gamma_5 \left[\tilde{S}_{B_2}(x,0)\right]^{\dagger} \gamma_5\,, \tag{E.37}$$

$$\tilde{S}_{B_2}(x,0) = \tilde{S}_5(x,0) + \tilde{S}_6(x,0) + \tilde{S}_7(x,0) + \tilde{S}_8(x,0)\,, \tag{E.38}$$

$$\tilde{S}_5 = -qC13(\,\tilde{C} * S_1(x,0) * \tilde{C}\,,\ U(x,0) * \mathbb{P}\,)\,, \tag{E.39}$$

$$\tilde{S}_6 = qC14(\,\mathbb{P} * S_1(x,0) * \tilde{C}\,,\ \tilde{C} * U(x,0)\,)\,, \tag{E.40}$$

$$\tilde{S}_7 = \mathbb{P} * qC24(\,S_1(x,0) * \tilde{C}\,,\ \tilde{C} * U(x,0)\,)\,, \tag{E.41}$$

$$\tilde{S}_8 = TraceSpin\Big[qC24(\,S_1(x,0) * \tilde{C}\,,\ \tilde{C} * U(x,0)\,)\Big] * \mathbb{P}\,. \tag{E.42}$$

The sequential source for $S_2(z,0)$ has the same expression as the sequential source for the standard nucleon three-point function $p + \mathscr{J}_- \to n$, but it also involves the first sequential propagator $S_1(z,0)$.

C-like

$$\begin{aligned}
C_{3pt}(x,y,z) = &\ e^{i\mathbf{q}\cdot\mathbf{z}}\ \mathrm{Tr}\Big\{\big(\ \gamma_5\ S_2^\dagger(z,0)\ \gamma_5\ \big)\ \Gamma_\mu\ U(z,0)\Big\}\ , && \text{(E.43)}\\
S_2(z,0) = &\ e^{+i\mathbf{p}'_\pi\cdot\mathbf{y}}\ D(z,y)\ \gamma_5\ S_1(y,0)\ , && \text{(E.44)}\\
S_1(y,0) = &\ e^{i\mathbf{p}'_N\cdot\mathbf{x}}\ D(y,x)\ \gamma_5\ \Big[\ \tilde{S}_1^\dagger(x,0) + \tilde{S}_2^\dagger(x,0) + \tilde{S}_3^\dagger(x,0) + \tilde{S}_4^\dagger(x,0)\ \Big]\gamma_5 && \\
= &\ e^{i\mathbf{p}'_N\cdot\mathbf{x}}\ D(z,x) * \gamma_5\ \Big[-\tilde{S}^{p\to n}(x,0)\Big]^\dagger\ \gamma_5\ , && \text{(E.45)}
\end{aligned}$$

$$\begin{aligned}
\tilde{S}_1(x,0) = &\ qC13(\ \tilde{C} * D(x,0) * \tilde{C}\ ,\ U(x,0) * \mathbb{P})\ , && \text{(E.46)}\\
\tilde{S}_2(x,0) = &\ -qC14(\ \mathbb{P} * D(x,0) * \tilde{C}\ ,\ \tilde{C} * U(x,0)\ )\ , && \text{(E.47)}\\
\tilde{S}_3(x,0) = &\ -TraceSpin(\ qC24(\ D(x,0) * \tilde{C}\ ,\ \tilde{C} * U(x,0)\ )\ ) * \mathbb{P}\ , && \text{(E.48)}\\
\tilde{S}_4(x,0) = &\ -\mathbb{P} * qC24(\ D(x,0) * \tilde{C}\ ,\ \tilde{C} * U(x,0)\ )\ . && \text{(E.49)}
\end{aligned}$$

The sequential source for $S_1(z,0)$ is equivalent to the sequential source for the standard nucleon three-point function $p + \mathscr{J}_- \to n$, apart from an overall minus sign.

E.5 $p + \mathscr{J}_- \to p + \pi^-$

See Fig. 4.1.

A-like

$$\begin{aligned}
C_{3pt} = &\ e^{i\mathbf{q}\cdot\mathbf{z}}\ \mathrm{Tr}\Big\{\big(\gamma_5\ S_2^\dagger(z,0)\ \gamma_5\big)\ \Gamma_\mu\ S_1(z,0)\Big\}\ , && \text{(E.50)}\\
S_1(z,0) = &\ e^{-i\mathbf{p}'_\pi\cdot\mathbf{y}}\ U(z,y)\ \gamma_5\ D(y,0)\ , && \text{(E.51)}\\
S_2(z,0) = &\ e^{+i\mathbf{p}'_N\cdot\mathbf{x}}\ D(z,x)\ \gamma_5\ \big[\ \tilde{S}_1^\dagger(x,0) + \tilde{S}_2^\dagger(x,0)\ \big]\ \gamma_5 && \\
= &\ e^{i\mathbf{p}'_N\cdot\mathbf{x}}\ D(z,x)\ \gamma_5\ \Big[\tilde{S}^{p\to p}_{\bar{d}d}(x,0)\Big]^\dagger\ \gamma_5\ , && \text{(E.52)}\\
\tilde{S}_1(x,0) = &\ qC12(\ U(x,0) * \mathbb{P}\ ,\ \tilde{C} * U(x,0) * \tilde{C}\ )^{T_D}\ , && \text{(E.53)}\\
\tilde{S}_2(x,0) = &\ qC14(\ \mathbb{P} * U(x,0) * \tilde{C}\ ,\ \tilde{C} * U(x,0)\ )\ . && \text{(E.54)}
\end{aligned}$$

Notice that one sequential source corresponds to the one for $p + \mathscr{J}_d \to p$, see App. E.1.

B-like

$$C_{3pt} = e^{i\mathbf{q}\cdot\mathbf{z}}\ \mathrm{Tr}\Big\{\big(\,\gamma_5\, S_2^\dagger(z,0)\,\gamma_5\,\big)\,\Gamma_\mu\, U(z,0)\Big\}\ , \tag{E.55}$$

$$S_2(z,0) = e^{i\mathbf{p}'_N\cdot\mathbf{x}}\, D(x,z)\,\gamma_5\,\big[\ \tilde{S}_1(x,0)^\dagger + \tilde{S}_2(x,0)^\dagger + \tilde{S}_3(x,0)^\dagger + \tilde{S}_4(x,0)^\dagger\ \big]\,\gamma_5\ , \tag{E.56}$$

$$\tilde{S}_1(x,0) = -\mathbb{P} * qC24(\,S_1(x,0) * \tilde{C},\ \tilde{C} * U(x,0)\,)\ , \tag{E.57}$$

$$\tilde{S}_2(x,0) = \mathbb{P} * qC24(\,U(x,0) * \tilde{C}\,,\ \tilde{C} * S_1(x,0)\,)\ , \tag{E.58}$$

$$\tilde{S}_3(x,0) = -qC14(\,\mathbb{P} * S_1(x,0) * \tilde{C}\,,\ \tilde{C} * U(x,0)\,)\ , \tag{E.59}$$

$$\tilde{S}_4(x,0) = -\Big[qC12(\,U(x,0) * \mathbb{P}\,,\ \tilde{C} * S_1(x,0) * \tilde{C}\,)\Big]^{T_D}\ , \tag{E.60}$$

$$\tag{E.61}$$

$$S_1(x,0) = e^{-i\mathbf{p}'_\pi\cdot\mathbf{y}}\, U(x,y)\,\gamma_5\, D(y,0)\ . \tag{E.62}$$

C-like

$$C_{3pt} = e^{i\mathbf{q}\cdot\mathbf{z}}\ \mathrm{Tr}\Big\{\big(\,\gamma_5\, S_2^\dagger(z,0)\,\gamma_5\,\big)\,\Gamma_\mu\, D(z,0)\Big\}\ , \tag{E.63}$$

$$S_2(z,0) = e^{i\mathbf{p}'_\pi\cdot\mathbf{y}}\, D(z,y)\,\gamma_5\, S_1(y,0)\ , \tag{E.64}$$

$$\begin{aligned} S_1(y,0) &= e^{i\mathbf{p}'_N\cdot\mathbf{x}}\, D(y,x)\,\gamma_5\,\big[\ \tilde{S}_1(x,0)^\dagger + \tilde{S}_2(x,0)^\dagger + \tilde{S}_3(x,0)^\dagger + \tilde{S}_4(x,0)^\dagger\ \big]\,\gamma_5 \\ &= e^{i\mathbf{p}'_N\cdot\mathbf{x}}\, D(z,x)\,\gamma_5\,\Big[\tilde{S}^{p\to p}_{\bar{u}u}(x,0)\Big]^\dagger\,\gamma_5\ , \end{aligned} \tag{E.65}$$

$$\tilde{S}_1(x,0) = -TraceSpin\Big[qC24(\,D(x,0) * \tilde{C}\,,\ \tilde{C} * U(x,0)\,)\Big] * \mathbb{P}\ , \tag{E.66}$$

$$\tilde{S}_2(x,0) = -\mathbb{P} * \Big[qC24(\,D(x,0) * \tilde{C}\,,\ \tilde{C} * U(x,0)\,)\Big]\ , \tag{E.67}$$

$$\tilde{S}_3(x,0) = qC13(\,\tilde{C} * D(x,0) * \tilde{C}\,,\ U(x,0) * \mathbb{P}\,)\ , \tag{E.68}$$

$$\tilde{S}_4(x,0) = qC12(\,U(x,0) * \mathbb{P}\,,\ \tilde{C} * D(x,0) * \tilde{C}\,)^{T_D}\ . \tag{E.69}$$

Notice that one sequential source is equivalent to the one in the process $p + \mathscr{J}_u \to p$, see App. E.2.

D-like

One-End trick:

$$C^D_{3pt}(\mathbf{p}'_N,\, \mathbf{p}'_\pi, \mathbf{q}; t, \tau) = \langle \sum_{\mathbf{x}} e^{-i\mathbf{p}'_N\cdot\mathbf{x}}\, C^{NN}_{2pt}(\mathbf{x}, t) \sum_{\mathbf{z},\mathbf{y}} e^{i\mathbf{q}\cdot\mathbf{z}} e^{-i\mathbf{p}'_\pi\cdot\mathbf{y}}\, C^{\pi\mathscr{J}}_{2pt}(\mathbf{z}, \tau; \mathbf{y}; t)\,\rangle \tag{E.70}$$

where the symbol $\langle\cdot\rangle$ means that the correlation functions must be multiplied for each gauge configuration. The expressions for these are:

$$\begin{aligned} C^{NN}_{2pt}(\mathbf{x},t) = &+\mathrm{Tr}\Big\{\mathbb{P} * traceColor\{D(x,0) * traceSpin\{G(x,0)\}\}\Big\} + \\ &+\mathrm{Tr}\{\mathbb{P} * traceColor\{D(x,0) * G(x,0)\}\}\,, \end{aligned} \tag{E.71}$$

$$C^{\pi\mathscr{J}}_{2pt}(\mathbf{z},\tau;\mathbf{y};t) = \mathrm{Tr}\Big\{D(z,y)^{\dagger}\,\gamma_5\Gamma\,U(z,y)\Big\}\,, \tag{E.72}$$

where

$$G(x,0) = qC13(D(x,0) * \tilde{C}^t, \tilde{C} * D(x,0))\,. \tag{E.73}$$

C^{NN}_{2pt} represents the nucleon-to-nucleon term depicted in Fig. $C^{\pi\mathscr{J}}_{2pt}$ represents the current-to-pion term depicted in Fig. Notice that two all-to-all propagators are needed to compute $C^{\pi\mathscr{J}}_{2pt}$ and in Sec. 2.9, I explain how to compute it with the One-End trick.

APPENDIX

SIX

ENSEMBLE USED FOR THE SIMULATIONS

Ensemble	β	$N_s^3 \times N_t$	Boundary condition	a[fm]	m_π[MeV]	$m_\pi L$	N_{cfgs}
A653	3.34	$24^3 \times 48$	periodic	0.098	426	5.1	800

Table F.1:
CLS gauge ensemble analysed in this exploratory work. The lattice unit momentum corresponds to $|\mathbf{p}| = \frac{2\pi}{L} \approx 525$ MeV.

BIBLIOGRAPHY

[1] A. Abdel-Rehim et al. Nucleon and pion structure with lattice QCD simulations at physical value of the pion mass. *Phys. Rev. D*, 92(11):114513, 2015. [Erratum: Phys.Rev.D 93, 039904 (2016)]. `arXiv:1507.04936`, `doi:10.1103/PhysRevD.92.114513`.

[2] K. Abe et al. Measurements of $\bar{\nu}_\mu$ and $\bar{\nu}_\mu + \nu_\mu$ charged-current cross-sections without detected pions or protons on water and hydrocarbon at a mean anti-neutrino energy of 0.86 GeV. *Progress of Theoretical and Experimental Physics*, 2021(4), Mar 2021. URL: `http://dx.doi.org/10.1093/ptep/ptab014`, `doi:10.1093/ptep/ptab014`.

[3] (T2K Collaboration) K. Abe et al. Constraint on the matter-antimatter symmetry-violating phase in neutrino oscillations. *Nature*, 580(7803):339–344, Apr 2020. URL: `https://doi.org/10.1038%2Fs41586-020-2177-0`, `doi:10.1038/s41586-020-2177-0`.

[4] (DUNE Collaboration) B. Abi et al. Deep Underground Neutrino Experiment (DUNE), Far Detector Technical Design Report, Volume I: Introduction to DUNE, 2020. `arXiv:2002.02967`.

[5] M. A. Acero et al. Improved measurement of neutrino oscillation parameters by the NOvA Experiment. *Phys. Rev. D*, 106:032004, Aug 2022. URL: `https://link.aps.org/doi/10.1103/PhysRevD.106.032004`, `arXiv:2108.08219`, `doi:10.1103/PhysRevD.106.032004`.

[6] M. Ademollo and R. Gatto. Nonrenormalization theorem for the strangeness-violating vector currents. *Phys. Rev. Lett.*, 13:264–266, Aug 1964. URL: `https://link.aps.org/doi/10.1103/PhysRevLett.13.264`, `doi:10.1103/PhysRevLett.13.264`.

[7] (OPERA Collaboration) N. Agafonova et al. Final results on neutrino oscillation parameters from the OPERA experiment in the CNGS beam. *Physical Review D*, 100(5), Sep 2019. URL: `http://dx.doi.org/10.1103/PhysRevD.100.051301`, `doi:10.1103/physrevd.100.051301`.

[8] (MiniBooNE Collaboration) A. A. Aguilar-Arevalo et al. First measurement of the muon neutrino charged current quasielastic double differential cross section. *Phys. Rev. D*, 81:092005, May 2010.

URL: `https://link.aps.org/doi/10.1103/PhysRevD.81.092005`, `doi:10.1103/PhysRevD.81.092005`.

[9] (MiniBooNE Collaboration) A. A. Aguilar-Arevalo et al. Measurement of Muon Neutrino Quasielastic Scattering on Carbon. *Phys. Rev. Lett.*, 100:032301, Jan 2008. URL: `https://link.aps.org/doi/10.1103/PhysRevLett.100.032301`, `doi:10.1103/PhysRevLett.100.032301`.

[10] (MiniBooNE Collaboration) A. A. Aguilar-Arevalo et al. Measurement of the neutrino neutral-current elastic differential cross section on mineral oil at $E_\nu \sim 1$ GeV. *Phys. Rev. D*, 82:092005, Nov 2010. URL: `https://link.aps.org/doi/10.1103/PhysRevD.82.092005`, `doi:10.1103/PhysRevD.82.092005`.

[11] (MiniBooNE Collaboration) A. A. Aguilar-Arevalo et al. Improved search for $\bar{\nu}_\mu \rightarrow \bar{\nu}_e$ oscillations in the MiniBooNE Experiment. *Physical Review Letters*, 110(16), Apr 2013. URL: `http://dx.doi.org/10.1103/PhysRevLett.110.161801`, `doi:10.1103/physrevlett.110.161801`.

[12] (MiniBooNE Collaboration) A. A. Aguilar-Arevalo et al. Measurement of the antineutrino neutral-current elastic differential cross section. *Phys. Rev. D*, 91:012004, Jan 2015. URL: `https://link.aps.org/doi/10.1103/PhysRevD.91.012004`, `doi:10.1103/PhysRevD.91.012004`.

[13] Z. Ahmad et al. Exploring neutrino–nucleus interactions in the GeV regime using MINERvA. *The European Physical Journal Special Topics*, Nov 2021. URL: `http://dx.doi.org/10.1140/epjs/s11734-021-00296-6`, `doi:10.1140/epjs/s11734-021-00296-6`.

[14] (KATRIN Collaboration) M. Aker et al. Direct neutrino-mass measurement with sub-electronvolt sensitivity. *Nature Phys.*, 18(2):160–166, 2022. `arXiv:2105.08533`, `doi:10.1038/s41567-021-01463-1`.

[15] M. Aker et al. Analysis methods for the first KATRIN neutrino-mass measurement. *Physical Review D*, 104(1), Jul 2021. URL: `http://dx.doi.org/10.1103/PhysRevD.104.012005`, `doi:10.1103/physrevd.104.012005`.

[16] C. Alabiso and G. Schierholz. Asymptotic behavior of form factors for two- and three-body bound states. *Phys. Rev. D*, 10:960–967, Aug 1974. URL: `https://link.aps.org/doi/10.1103/PhysRevD.10.960`, `doi:10.1103/PhysRevD.10.960`.

[17] (APE Collaboration) M. Albanese et al. Glueball Masses and String Tension in Lattice QCD. *Phys. Lett. B*, 192:163–169, 1987. `doi:10.1016/0370-2693(87)91160-9`.

[18] C. Alexandrou. Nucleon axial form factors from lattice QCD. *SciPost Phys. Proc.*, 6:006, 2022. `doi:10.21468/SciPostPhysProc.6.006`.

[19] C. Alexandrou et al. Nucleon axial form factors using $N_f = 2$ twisted mass fermions with a physical value of the pion mass. *Phys. Rev. D*, 96:054507, Sep 2017. URL: `https://link.aps.org/doi/10.1103/PhysRevD.96.054507`, `doi:10.1103/PhysRevD.96.054507`.

[20] C. Alexandrou et al. Nucleon axial and pseudoscalar form factors from lattice QCD at the physical point. *Phys. Rev. D*, 103(3):034509, 2021. `arXiv:2011.13342`, `doi:10.1103/PhysRevD.103.034509`.

[21] (UKQCD Collaboration) C. R. Allton et al. Gauge-invariant smearing and matrix correlators using Wilson fermions at $\beta = 6.2$. *Phys. Rev. D*, 47:5128–5137, Jun 1993. URL: `https://link.aps.org/doi/10.1103/PhysRevD.47.5128`, `doi:10.1103/PhysRevD.47.5128`.

[22] (FLAG) Y. Aoki et al. FLAG Review 2021. 2021. URL: `https://arxiv.org/abs/2111.09849`, `doi:10.48550/ARXIV.2111.09849`.

[23] (UA1 Collaboration) G. Arnison et al. Experimental observation of isolated large transverse energy electrons with associated missing energy at s=540 GeV. *Physics Letters B*, 122(1):103–116, 1983. URL: `https://www.sciencedirect.com/science/article/pii/0370269383911772`, `doi:https://doi.org/10.1016/0370-2693(83)91177-2`.

[24] J. N. Bahcall and R. Davis. Solar Neutrinos - a Scientific Puzzle. *Science*, 191:264–267, 1976. `doi:10.1126/science.191.4224.264`.

[25] N. J. Baker et al. Quasielastic neutrino scattering: A measurement of the weak nucleon axial-vector form factor. *Phys. Rev. D*, 23:2499–2505, Jun 1981. URL: `https://link.aps.org/doi/10.1103/PhysRevD.23.2499`, `doi:10.1103/PhysRevD.23.2499`.

[26] G. Bali et al. Observation of string breaking in QCD. *Phys. Rev. D*, 71:114513, Jun 2005. URL: `https://link.aps.org/doi/10.1103/PhysRevD.71.114513`, `doi:10.1103/PhysRevD.71.114513`.

[27] (RQCD Collaboration) G. Bali, L. Barca, et al. Nucleon axial structure from lattice QCD. *JHEP*, 05:126, 2020. `arXiv:1911.13150`, `doi:10.1007/JHEP05(2020)126`.

[28] (RQCD Collaboration) G. Bali et al. nucleon isovector couplings from $N_f = 2$ lattice QCD. *Phys. Rev. D*, 91(5):054501, Mar 2015. `arXiv:1412.7336`, `doi:10.1103/PhysRevD.91.054501`.

[29] (RQCD Collaboration) G. Bali et al. Nucleon generalized form factors from two-flavor lattice QCD. *Phys. Rev. D*, 100(1):014507, 2019. `arXiv:1812.08256`, `doi:10.1103/PhysRevD.100.014507`.

[30] (RQCD Collaboration) G. Bali et al. Solving the PCAC puzzle for nucleon axial and pseudoscalar form factors. *Physics Letters B*, 789:666–674, Feb 2019. URL:

`http://dx.doi.org/10.1016/j.physletb.2018.12.053`, `doi:10.1016/j.physletb.2018.12.053`.

[31] (RQCD Collaboration) G. Bali et al. Nonperturbative Renormalization in Lattice QCD with three Flavors of Clover Fermions: Using Periodic and Open Boundary Conditions. *Phys. Rev. D*, 103(9):094511, 2021. `arXiv:2012.06284`, `doi:10.1103/PhysRevD.103.094511`.

[32] (UA2 Collaboration) M. Banner et al. Observation of single isolated electrons of high transverse momentum in events with missing transverse energy at the CERN pp collider. *Physics Letters B*, 122(5):476–485, 1983. URL: `https://www.sciencedirect.com/science/article/pii/0370269383916052`, `doi:https://doi.org/10.1016/0370-2693(83)91605-2`.

[33] O. Bär. Nucleon-pion-state contribution to nucleon two-point correlation functions. *Phys. Rev. D*, 92(7):074504, 2015. `arXiv:1503.03649`, `doi:10.1103/PhysRevD.92.074504`.

[34] O. Bär. Nucleon-pion-state contributions in the determination of the nucleon axial charge. *PoS*, LATTICE2015:123, 2016. `arXiv:1508.01021`, `doi:10.22323/1.251.0123`.

[35] O. Bär. Three-particle $N\pi\pi$ state contribution to the nucleon two-point function in lattice QCD. *Phys. Rev. D*, 97(9):094507, 2018. `arXiv:1802.10442`, `doi:10.1103/PhysRevD.97.094507`.

[36] L. Barca, G. Bali, and S. Collins. Investigating $N \to N\pi$ axial matrix elements. *PoS*, LATTICE2021:359, 2022. `arXiv:2110.11908`, `doi:10.22323/1.396.0359`.

[37] A. Bellerive et al. The Sudbury Neutrino Observatory. *Nuclear Physics B*, 908:30–51, Jul 2016. URL: `http://dx.doi.org/10.1016/j.nuclphysb.2016.04.035`, `doi:10.1016/j.nuclphysb.2016.04.035`.

[38] (ALPHA Collaboration) B. Benoit et al. On the generalized eigenvalue method for energies and matrix elements in lattice field theory. *Journal of High Energy Physics*, 2009(04):094–094, Apr 2009. URL: `http://dx.doi.org/10.1088/1126-6708/2009/04/094`, `doi:10.1088/1126-6708/2009/04/094`.

[39] B. Berg. Glueball calculation in lattice gauge theories. In *Aspen Workshop on Glueballs and Lattice QCD*, 8 1984.

[40] V. Bernard, L. Elouadrhiri, and U. G. Meißner. Axial structure of the nucleon. *Journal of Physics G: Nuclear and Particle Physics*, 28(1):R1–R35, nov 2001. `doi:10.1088/0954-3899/28/1/201`.

[41] V. Bernard, N. Kaiser, and U. G. Meissner. QCD accurately predicts the induced pseudoscalar coupling constant. *Phys. Rev. D*, 50:6899–6901, Dec 1994. URL: `https://link.aps.org/doi/10.1103/PhysRevD.50.6899`, `doi:10.1103/PhysRevD.50.6899`.

[42] V. Bernard and U. G. Meißner. Chiral Perturbation Theory. *Annual Review of Nuclear and Particle Science*, 57(1):33–60, Nov 2007. URL: `http://dx.doi.org/10.1146/annurev.nucl.56.080805.140449`, `doi:10.1146/annurev.nucl.56.080805.140449`.

[43] B. Bhattacharya, R. J. Hill, and G. Paz. Model-independent determination of the axial mass parameter in quasielastic neutrino-nucleon scattering. *Physical Review D*, 84(7), Oct 2011. URL: `http://dx.doi.org/10.1103/PhysRevD.84.073006`, `doi:10.1103/physrevd.84.073006`.

[44] B. Bhattacharya, G. Paz, and A. J. Tropiano. Model-independent determination of the axial mass parameter in quasielastic antineutrino-nucleon scattering. *Physical Review D*, 92(11), Dec 2015. URL: `http://dx.doi.org/10.1103/PhysRevD.92.113011`, `doi:10.1103/physrevd.92.113011`.

[45] T. Bhattacharya et al. Axial, Scalar and Tensor Charges of the Nucleon from 2+1+1-flavor Lattice QCD. *Phys. Rev. D*, 94(5):054508, 2016. `arXiv:1606.07049`, `doi:10.1103/PhysRevD.94.054508`.

[46] J. Bickerton et al. Patterns of flavor symmetry breaking in hadron matrix elements involving u, d, and s quarks. *Physical Review D*, 100(11), Dec 2019. URL: `https://doi.org/10.1103%2Fphysrevd.100.114516`, `doi:10.1103/physrevd.100.114516`.

[47] (ETM Collaboration) P. Boucaud et al. Dynamical twisted mass fermions with light quarks: simulation and analysis details. *Computer Physics Communications*, 179(10):695–715, Nov 2008. URL: `http://dx.doi.org/10.1016/j.cpc.2008.06.013`, `doi:10.1016/j.cpc.2008.06.013`.

[48] C. Bourrely, L. Lellouch, and I. Caprini. Model-independent description of $B \to \pi l \nu$ decays and a determination of $|V_{ub}|$. *Phys. Rev. D*, 79:013008, Jan 2009. URL: `https://link.aps.org/doi/10.1103/PhysRevD.79.013008`, `doi:10.1103/PhysRevD.79.013008`.

[49] M. A.-P. Brown et al. New result for the neutron β-asymmetry parameter A_0 from UCNA. *Physical Review C*, 97(3), Mar 2018. URL: `http://dx.doi.org/10.1103/PhysRevC.97.035505`, `doi:10.1103/physrevc.97.035505`.

[50] M. Bruno, T. Korzec, and S. Schaefer. Setting the scale for the CLS 2+1 flavor ensembles. *Physical Review D*, 95(7), Apr 2017. URL: `http://dx.doi.org/10.1103/PhysRevD.95.074504`, `doi:10.1103/physrevd.95.074504`.

[51] (ALPHA Collaboration) J. Bulava, M. Donnellan, and R. Sommer. On the computation of hadron-to-hadron transition matrix elements in lattice QCD. *Journal of High Energy Physics*, 2012(1), Jan 2012. URL: `http://dx.doi.org/10.1007/JHEP01(2012)140`, `doi:10.1007/jhep01(2012)140`.

[52] J. Bulava et al. Non-perturbative improvement of the axial current in $N_f = 3$ lattice QCD with Wilson fermions and tree-level improved gauge action. *Nuclear Physics B*, 896:555–568, jul 2015. URL: `https://doi.org/10.1016%2Fj.nuclphysb.2015.05.003`, `doi:10.1016/j.nuclphysb.2015.05.003`.

[53] N. Cabibbo. Unitary Symmetry and Leptonic Decays. *Phys. Rev. Lett.*, 10:531–533, Jun 1963. URL: `https://link.aps.org/doi/10.1103/PhysRevLett.10.531`, `doi:10.1103/PhysRevLett.10.531`.

[54] C. G. Callan et al. Structure of Phenomenological Lagrangians. II. *Phys. Rev.*, 177:2247–2250, Jan 1969. URL: `https://link.aps.org/doi/10.1103/PhysRev.177.2247`, `doi:10.1103/PhysRev.177.2247`.

[55] N. A. Campbell, L. A. Griffiths, C. Michael, and P. E. L. Rakow. Mesons with excited glue from SU(3) lattice gauge theory. *Phys. Lett. B*, 142:291–293, 1984. `doi:10.1016/0370-2693(84)91200-0`.

[56] S. Capitani et al. Renormalisation and off-shell improvement in lattice perturbation theory. *Nuclear Physics B*, 593(1-2):183–228, Jan 2001. URL: `http://dx.doi.org/10.1016/S0550-3213(00)00590-3`, `doi:10.1016/s0550-3213(00)00590-3`.

[57] S. Capitani et al. The nucleon axial charge from lattice QCD with controlled errors. *Phys. Rev. D*, 86:074502, 2012. `arXiv:1205.0180`, `doi:10.1103/PhysRevD.86.074502`.

[58] S. Capitani et al. Nucleon electromagnetic form factors in two-flavor QCD. *Physical Review D*, 92(5), Sep 2015. URL: `http://dx.doi.org/10.1103/PhysRevD.92.054511`, `doi:10.1103/physrevd.92.054511`.

[59] S. Capitani et al. Isovector axial form factors of the nucleon in two-flavor lattice QCD. *International Journal of Modern Physics A*, 34(02):1950009, jan 2019. URL: `https://doi.org/10.1142%2Fs0217751x1950009x`, `doi:10.1142/s0217751x1950009x`.

[60] C. E. Carlson and J. L. Poor. Nucleon axial-vector form factor in perturbative QCD. *Phys. Rev. D*, 34:1478–1481, Sep 1986. URL: `https://link.aps.org/doi/10.1103/PhysRevD.34.1478`, `doi:10.1103/PhysRevD.34.1478`.

[61] D. Casper. The nuance neutrino physics simulation and the future. *Nuclear Physics B - Proceedings Supplements*, 112(1-3):161–170, Nov 2002. URL: `http://dx.doi.org/10.1016/S0920-5632(02)01756-5`, `doi:10.1016/s0920-5632(02)01756-5`.

[62] C. C. Chang et al. A percent-level determination of the nucleon axial coupling from Quantum Qhromodynamics. *Nature*, 558(7708):91–94, 2018. `arXiv:1805.12130`, `doi:10.1038/s41586-018-0161-8`.

[63] S. Coleman, J. Wess, and B. Zumino. Structure of Phenomenological Lagrangians. I . *Phys. Rev.*, 177:2239–2247, Jan 1969. URL: `https://link.aps.org/doi/10.1103/PhysRev.177.2239`, `doi:10.1103/PhysRev.177.2239`.

[64] R. Dashen. Chiral $SU(3) \times SU(3)$ as a Symmetry of the Strong Interactions. *Phys. Rev.*, 183:1245–1260, Jul 1969. URL: `https://link.aps.org/doi/10.1103/PhysRev.183.1245`, `doi:10.1103/PhysRev.183.1245`.

[65] R. Dashen and M. Weinstein. Soft Pions, Chiral Symmetry and Phenomenological Lagrangians. *Phys. Rev.*, 183:1261–1291, Jul 1969. URL: `https://link.aps.org/doi/10.1103/PhysRev.183.1261`, `doi:10.1103/PhysRev.183.1261`.

[66] D. Djukanovic. Quark Contraction Tool – QCT. *Comp. Phys. Comm.*, 247:106950, Feb 2020. URL: `http://dx.doi.org/10.1016/j.cpc.2019.106950`, `doi:10.1016/j.cpc.2019.106950`.

[67] S. J. Dong and K. F. Liu. Stochastic estimation with Z_2 noise. *Physics Letters B*, 328(1-2):130–136, May 1994. URL: `http://dx.doi.org/10.1016/0370-2693(94)90440-5`, `doi:10.1016/0370-2693(94)90440-5`.

[68] J. F. Donoghue and D. Wyler. Isospin breaking and the precise determination of V_{ud}. *Physics Letters B*, 241(2):243–248, 1990. URL: `https://www.sciencedirect.com/science/article/pii/037026939091287L`, `doi:https://doi.org/10.1016/0370-2693(90)91287-L`.

[69] R. G. Edwards et al. The Nucleon axial charge in full lattice QCD. *Phys. Rev. Lett.*, 96:052001, 2006. `arXiv:hep-lat/0510062`, `doi:10.1103/PhysRevLett.96.052001`.

[70] J. P. Elliott and P. G. Dawber. *Symmetry in Physics VOL. 1: Principles and Simple Applications.* 1987.

[71] J. P. Ellis. TikZ-feynman: Feynman diagrams with TikZ. *Computer Physics Communications*, 210:103–123, Jan 2017. URL: `http://dx.doi.org/10.1016/j.cpc.2016.08.019`, `doi:10.1016/j.cpc.2016.08.019`.

[72] Z. Epstein, G. Paz, and J. Roy. Model independent extraction of the proton magnetic radius from electron scattering. *Physical Review D*, 90(7), Oct 2014. URL: `http://dx.doi.org/10.1103/PhysRevD.90.074027`, `doi:10.1103/physrevd.90.074027`.

[73] (RQCD Collaboration) R. Evans, G. Bali, and S. Collins. Improved semileptonic form factor calculations in lattice QCD. *Physical Review D*, 82(9), Nov 2010. URL: `http://dx.doi.org/10.1103/PhysRevD.82.094501`, `doi:10.1103/physrevd.82.094501`.

[74] E. Fermi. An attempt of a theory of beta radiation. 1. *Z. Phys.*, 88:161–177, 1934. `doi:10.1007/BF01351864`.

[75] J. A. Formaggio and G. P. Zeller. From eV to EeV: Neutrino cross sections across energy scales. *Reviews of Modern Physics*, 84(3):1307–1341, Sep 2012. URL: `https://doi.org/10.1103%2Frevmodphys.84.1307`, `doi:10.1103/revmodphys.84.1307`.

[76] M. Foster and C. Michael. Quark mass dependence of hadron masses from lattice qcd. *Physical Review D*, 59(7), Feb 1999. URL: `http://dx.doi.org/10.1103/PhysRevD.59.074503`, `doi:10.1103/physrevd.59.074503`.

[77] R. Frezzotti, V. Lubicz, and S. Simula. Electromagnetic form factor of the pion from twisted-mass lattice QCD at $N_f = 2$. *Physical Review D*, 79(7), Apr 2009. URL: `http://dx.doi.org/10.1103/PhysRevD.79.074506`, `doi:10.1103/physrevd.79.074506`.

[78] A. Frommer et al. Adaptive Aggregation Based Domain Decomposition Multigrid for the Lattice Wilson Dirac Operator. *SIAM J. Sci. Comput.*, 36:A1581–A1608, 2014. `arXiv:1303.1377`, `doi:10.1137/130919507`.

[79] W. H. Furry. On transition probabilities in double beta-disintegration. *Phys. Rev.*, 56:1184–1193, Dec 1939. URL: `https://link.aps.org/doi/10.1103/PhysRev.56.1184`, `doi:10.1103/PhysRev.56.1184`.

[80] J. Gasser and H. Leutwyler. Chiral perturbation theory to one loop. *Annals of Physics*, 158(1):142–210, 1984. URL: `https://www.sciencedirect.com/science/article/pii/0003491684902422`, `doi:https://doi.org/10.1016/0003-4916(84)90242-2`.

[81] J. Gasser and H. Leutwyler. Chiral perturbation theory: Expansions in the mass of the strange quark. *Nuclear Physics B*, 250(1):465–516, 1985. URL: `https://www.sciencedirect.com/science/article/pii/0550321385904924`, `doi:https://doi.org/10.1016/0550-3213(85)90492-4`.

[82] C. Gattringer and C. B. Lang. *Quantum Chromodynamics on the lattice*, volume 788. Springer, Berlin, 2010. `doi:10.1007/978-3-642-01850-3`.

[83] M. Gell-Mann, R. J. Oakes, and B. Renner. Behavior of Current Divergences under $\mathrm{SU}_3 \times \mathrm{SU}_3$. *Phys. Rev.*, 175:2195–2199, Nov 1968. URL: `https://link.aps.org/doi/10.1103/PhysRev.175.2195`, `doi:10.1103/PhysRev.175.2195`.

[84] L. Giusti et al. The QCD chiral condensate from the lattice. *Nuclear Physics B*, 538(1-2):249–277, Jan 1999. URL: `http://dx.doi.org/10.1016/S0550-3213(98)00659-2`, `doi:10.1016/s0550-3213(98)00659-2`.

[85] M. Göckeler et al. Scattering phases for meson and baryon resonances on general moving-frame lattices. *Physical Review D*, 86(9), Nov 2012. URL: `http://dx.doi.org/10.1103/PhysRevD.86.094513`, `doi:10.1103/physrevd.86.094513`.

[86] M. F. L. Golterman. How good is the quenched approximation of QCD? *Pramana*, 45(S1):141–154, Oct 1995. URL: `https://doi.org/10.1007%2Fbf02907971`, `doi:10.1007/bf02907971`.

[87] J. Green. Systematics in nucleon matrix element calculations. *PoS*, LATTICE2018:016, 2018. `arXiv:1812.10574`, `doi:10.22323/1.334.0016`.

[88] R. Gupta et al. Axial-vector form factors of the nucleon from lattice QCD. *Physical Review D*, 96(11), Dec 2017. URL: `http://dx.doi.org/10.1103/PhysRevD.96.114503`, `doi:10.1103/physrevd.96.114503`.

[89] S. Güsken. A study of smearing techniques for hadron correlation functions. *Nucl. Phys. B*, 17:361–364, 1990. URL: `https://www.sciencedirect.com/science/article/pii/092056329090273W`, `doi:https://doi.org/10.1016/0920-5632(90)90273-W`.

[90] M. T. Hansen and H. B. Meyer. On the effect of excited states in lattice calculations of the nucleon axial charge. *Nuclear Physics B*, 923:558–587, Oct 2017. URL: `http://dx.doi.org/10.1016/j.nuclphysb.2017.08.017`, `doi:10.1016/j.nuclphysb.2017.08.017`.

[91] N. Hasan et al. Nucleon axial, scalar and tensor charges using lattice QCD at the physical pion mass. *Physical Review D*, 99(11), Jun 2019. URL: `http://dx.doi.org/10.1103/PhysRevD.99.114505`, `doi:10.1103/physrevd.99.114505`.

[92] A. Hasenfratz and F. Knechtli. Flavor symmetry and the static potential with hypercubic blocking. *Physical Review D*, 64(3), Jul 2001. URL: `http://dx.doi.org/10.1103/PhysRevD.64.034504`, `doi:10.1103/physrevd.64.034504`.

[93] R. J. Hill and G. Paz. Model-independent extraction of the proton charge radius from electron scattering. *Phys. Rev. D*, 82:113005, Dec 2010. URL: `https://link.aps.org/doi/10.1103/PhysRevD.82.113005`, `doi:10.1103/PhysRevD.82.113005`.

[94] R. Horsley et al. Nucleon axial charge and pion decay constant from two-flavor lattice QCD. *Phys. Lett. B*, 732:41–48, 2014. `arXiv:1302.2233`, `doi:10.1016/j.physletb.2014.03.002`.

[95] (Hyper-Kamiokande Collaboration) J. R. Wilson. The Hyper-Kamiokande Experiment. *J. Phys. Conf. Ser.*, 2156:012153, 2021. `doi:10.1088/1742-6596/2156/1/012153`.

[96] K. I. Ishikawa et al. Nucleon form factors on a large volume lattice near the physical point in $2+1$ flavor QCD. *Physical Review D*, 98(7), oct 2018. URL: `https://doi.org/10.1103%2Fphysrevd.98.074510`, `doi:10.1103/physrevd.98.074510`.

[97] K. I. Ishikawa et al. Nucleon form factors on a large volume lattice near the physical point in 2+1 flavor QCD. *Physical Review D*, 98(7), Oct 2018. URL: `http://dx.doi.org/10.1103/PhysRevD.98.074510`, `doi:10.1103/physrevd.98.074510`.

[98] Y. C. Jang et al. Nucleon Axial and Electromagnetic Form Factors. *EPJ Web Conf.*, 175:06033, 2018. `arXiv:1801.01635`, `doi:10.1051/epjconf/201817506033`.

[99] Y. C. Jang et al. Nucleon axial and electromagnetic form factors. *EPJ Web of Conferences*, 175:06033, 2018. URL: `http://dx.doi.org/10.1051/epjconf/201817506033`, `doi:10.1051/epjconf/201817506033`.

[100] Y. C. Jang et al. Axial Vector Form Factors from Lattice QCD that Satisfy the PCAC Relation. *Physical Review Letters*, 124(7), Feb 2020. URL: `http://dx.doi.org/10.1103/PhysRevLett.124.072002`, `doi:10.1103/physrevlett.124.072002`.

[101] M. Kobayashi and T. Maskawa. CP Violation in the Renormalizable Theory of Weak Interaction. *Prog. Theor. Phys.*, 49:652–657, 1973. `doi:10.1143/PTP.49.652`.

[102] P. Korcyl and G. Bali. Nonperturbative determination of improvement coefficients using coordinate space correlators in $N_f = 2+1$ lattice QCD. *Phys. Rev. D*, 95:014505, Jan 2017. URL: `https://link.aps.org/doi/10.1103/PhysRevD.95.014505`, `doi:10.1103/PhysRevD.95.014505`.

[103] A. S. Kronfeld et al. Lattice QCD and Neutrino-Nucleus Scattering. *Eur. Phys. J. A*, 55(11):196, 2019. `arXiv:1904.09931`, `doi:10.1140/epja/i2019-12916-x`.

[104] G. Lee, J. R. Arrington, and R. J. Hill. Extraction of the proton radius from electron-proton scattering data. *Phys. Rev. D*, 92:013013, Jul 2015. URL: `https://link.aps.org/doi/10.1103/PhysRevD.92.013013`, `doi:10.1103/PhysRevD.92.013013`.

[105] P. G. Lepage and S. J. Brodsky. Exclusive Processes in Perturbative Quantum Chromodynamics. *Phys. Rev. D*, 22:2157, 1980. `doi:10.1103/PhysRevD.22.2157`.

[106] H. Leutwyler. On the Foundations of Chiral Perturbation Theory. *Annals of Physics*, 235(1):165–203, Oct 1994. URL: `http://dx.doi.org/10.1006/aphy.1994.1094`, `doi:10.1006/aphy.1994.1094`.

[107] J. Liang et al. Lattice calculation of nucleon isovector axial charge with improved currents. *Physical Review D*, 96(3), aug 2017. URL: `https://doi.org/10.1103%2Fphysrevd.96.034519`, `doi:10.1103/physrevd.96.034519`.

[108] (Fermilab Lattice Collaboration) Y. Lin et al. Computing Nucleon Charges with Highly Improved Staggered Quarks, 2020. `arXiv:2010.10455`.

[109] M. Lüscher and P. Weisz. On-Shell Improved Lattice Gauge Theories. *Commun. Math. Phys.*, 97:59, 1985. [Erratum: Commun.Math.Phys. 98, 433 (1985)]. `doi:10.1007/BF01206178`.

[110] M. Lüscher and U. Wolff. How to Calculate the Elastic Scattering Matrix in Two-dimensional Quantum Field Theories by Numerical Simulation. *Nucl. Phys. B*, 339:222–252, 1990. `doi:10.1016/0550-3213(90)90540-T`.

[111] L. Maiani et al. Scalar densities and baryon mass differences in lattice QCD with Wilson fermions. *Nuclear Physics B*, 293:420–444, 1987. URL: `https://www.sciencedirect.com/science/article/pii/0550321387900782`, `doi:https://doi.org/10.1016/0550-3213(87)90078-2`.

[112] Z. Maki, M. Nakagawa, and S. Sakata. Remarks on the unified model of elementary particles. *Prog. Theor. Phys.*, 28:870–880, 1962. `doi:10.1143/PTP.28.870`.

[113] F. Mandl and G. Shaw. *Quantum Field Theory*. 1985.

[114] G. Martinelli and C. T. Sachrajda. A Lattice Study of Nucleon Structure. *Nucl. Phys. B*, 316:355–372, 1989. `doi:10.1016/0550-3213(89)90035-7`.

[115] P. T. Matthews and A. Salam. The Green's functions of quantized fields. *Nuovo Cim.*, 12:563–565, 1954. `doi:10.1007/BF02781302`.

[116] P. T. Matthews and A. Salam. Propagators of quantized field. *Nuovo Cim.*, 2:120–134, 1955. `doi:10.1007/BF02856011`.

[117] C. McNeile and C. Michael. Decay width of light quark hybrid meson from the lattice. *Physical Review D*, 73(7), Apr 2006. URL: `http://dx.doi.org/10.1103/PhysRevD.73.074506`, `doi:10.1103/physrevd.73.074506`.

[118] (UKQCD Collaboration) C. McNeile and C. Michael. Hadronic decay of a vector meson from the lattice. *Physics Letters B*, 556(3-4):177–184, Mar 2003. URL: `http://dx.doi.org/10.1016/S0370-2693(03)00130-8`, `doi:10.1016/s0370-2693(03)00130-8`.

[119] S. Meinel and G. Rendon. $\Lambda_b \to \Lambda^*(1520)\, l^+ l^-$ form factors from lattice QCD. *Physical Review D*, 103(7), Apr 2021. URL: `http://dx.doi.org/10.1103/PhysRevD.103.074505`, `doi:10.1103/physrevd.103.074505`.

[120] S. Meinel and G. Rendon. Charm-baryon semileptonic decays and the strange Λ^* resonances: New insights from lattice QCD. *Phys. Rev. D*, 105:L051505, Mar 2022. URL: `https://link.aps.org/doi/10.1103/PhysRevD.105.L051505`, `doi:10.1103/PhysRevD.105.L051505`.

[121] M. P. Mendenhall et al. Precision measurement of the neutron β-decay asymmetry. *Physical Review C*, 87(3), Mar 2013. URL: `http://dx.doi.org/10.1103/PhysRevC.87.032501`, `doi:10.1103/physrevc.87.032501`.

[122] A. S. Meyer. *The Nucleon Axial Form Factor and Staggered Lattice QCD.* PhD thesis, Chicago U., 2017. `doi:10.2172/1416547`.

[123] C. Michael and I. Teasdale. Extracting Glueball Masses From Lattice QCD . *Nucl. Phys. B*, 215:433–446, 1983. `doi:10.1016/0550-3213(83)90674-0`.

[124] W. Miller. *Symmetry groups and their applications.* Academic Press New York, 1972.

[125] D. Mohler, S. Schaefer, and J. Simeth. CLS 2+1 flavor simulations at physical light-and strange-quark masses. *EPJ Web of Conferences*, 175:02010, 2018. URL: `http://dx.doi.org/10.1051/epjconf/201817502010`, `doi:10.1051/epjconf/201817502010`.

[126] C. Morningstar and M. Peardon. Analytic smearing of SU(3) link variables in lattice QCD. *Physical Review D*, 69(5), Mar 2004. URL: `http://dx.doi.org/10.1103/PhysRevD.69.054501`, `doi:10.1103/physrevd.69.054501`.

[127] D. Mund et al. Determination of the Weak Axial Vector Coupling $\lambda = g_A/g_V$ from a Measurement of the β-Asymmetry Parameter A in Neutron Beta Decay. *Physical Review Letters*, 110(17), Apr 2013. URL: `http://dx.doi.org/10.1103/PhysRevLett.110.172502`, `doi:10.1103/physrevlett.110.172502`.

[128] T. Muta. *Foundations of Quantum Chromodynamics. Second edition*, volume 57. 1998.

[129] Y. Nambu and G. Jona-Lasinio. Dynamical model of elementary particles based on an analogy with superconductivity. i. *Phys. Rev.*, 122:345–358, Apr 1961. URL: `https://link.aps.org/doi/10.1103/PhysRev.122.345`, `doi:10.1103/PhysRev.122.345`.

[130] B. J. Owen et al. *Physics Letters B*, 723(1–3):217–223, Jun 2013. URL: `http://dx.doi.org/10.1016/j.physletb.2013.04.063`, `doi:10.1016/j.physletb.2013.04.063`.

[131] H. Panagopoulos and Y. Proestos. The Critical hopping parameter in O(a) improved lattice QCD. *Phys. Rev. D*, 65:014511, 2002. `arXiv:hep-lat/0108021`, `doi:10.1103/PhysRevD.65.014511`.

[132] B. Pontecorvo. Mesonium and anti-mesonium. *Sov. Phys. JETP*, 6:429, 1957.

[133] B. Pontecorvo. Neutrino Experiments and the Problem of Conservation of Leptonic Charge. *Zh. Eksp. Teor. Fiz.*, 53:1717–1725, 1967.

[134] B. Sheikholeslami and R. Wohlert. Improved Continuum Limit Lattice Action for QCD with Wilson Fermions. *Nucl. Phys. B*, 259:572, 1985. `doi:10.1016/0550-3213(85)90002-1`.

[135] S. Sint and P. Weisz. Further results on O(a) improved lattice QCD to one-loop order of perturbation theory. *Nuclear Physics B*, 502(1-2):251–268, Sep 1997. URL: `http://dx.doi.org/10.1016/S0550-3213(97)00372-6`, `doi:10.1016/s0550-3213(97)00372-6`.

[136] Y. Taniguchi and A. Ukawa. Perturbative calculation of improvement coefficients to $O(g^2 a)$ for bilinear quark operators in lattice qcd. *Phys. Rev. D*, 58:114503, Oct 1998. URL: `https://link.aps.org/doi/10.1103/PhysRevD.58.114503`, `doi:10.1103/PhysRevD.58.114503`.

[137] A. W. Thomas and W. Weise. *The Structure of the Nucleon*. Wiley, Germany, 2001. `doi:10.1002/352760314X`.

[138] B. C. Tiburzi. Chiral Corrections to Nucleon Two- and Three-Point Correlation Functions. *Phys. Rev. D*, 91:094510, 2015. `arXiv:1503.06329`, `doi:10.1103/PhysRevD.91.094510`.

[139] N. Tsukamoto et al. Nucleon structure from 2+1 flavor lattice QCD near the physical point. *EPJ Web of Conferences*, 175:06007, 2018. URL: `http://dx.doi.org/10.1051/epjconf/201817506007`, `doi:10.1051/epjconf/201817506007`.

[140] (UKQCD and RBC Collaborations). The pion's electromagnetic form factor at small momentum transfer in full lattice QCD. *Journal of High Energy Physics*, 2008(07):112–112, Jul 2008. URL: `http://dx.doi.org/10.1088/1126-6708/2008/07/112`, `doi:10.1088/1126-6708/2008/07/112`.

[141] (UKQCD and RBC Collaborations). Use of stochastic sources for the lattice determination of light quark physics. *Journal of High Energy Physics*, 2008(08):086–086, Aug 2008. URL: `http://dx.doi.org/10.1088/1126-6708/2008/08/086`, `doi:10.1088/1126-6708/2008/08/086`.

[142] S. Weinberg. Phenomenological Lagrangians. *Physica A: Statistical Mechanics and its Applications*, 96(1):327–340, 1979. URL: `https://www.sciencedirect.com/science/article/pii/0378437179902231`, `doi:https://doi.org/10.1016/0378-4371(79)90223-1`.

[143] E. P. Wigner. On Unitary Representations of the Inhomogeneous Lorentz Group. *Annals Math.*, 40:149–204, 1939. `doi:10.2307/1968551`.

[144] K. G. Wilson. Confinement of Quarks. *Phys. Rev. D*, 10:2445–2459, 1974. `doi:10.1103/PhysRevD.10.2445`.

[145] K. G. Wilson. Talk at the Abingdon Meeting on Lattice Gauge Theories. 1981.

[146] T. Wurm. *Nucleon axial and pseudoscalar isovector form factors from lattice QCD*. PhD thesis, Regensburg U., 2021. `doi:10.5283/EPUB.46419`.

[147] F. J. Yndurain. *The Theory of Quark and Gluon Interactions*. Theoretical and Mathematical Physics. Springer, Berlin, Germany, 2006. `doi:10.1007/3-540-33210-3`.

ACKNOWLEDGEMENTS

I am extremely grateful to my supervisors Gunnar Bali and Sara Collins for their renowned scientific wisdom because this endeavour would not have been possible without their technical advice. I am also grateful to them for all the opportunities they have given me. During my PhD, I travelled to both ends of the world. I have been in China to attend a 3-week Summer School and travelled to USA, where I spent 2 weeks visiting Fermilab and MIT. I would like to extend my sincere thanks to the PhD committee members, namely Gunnar Bali, Christoph Lehner, Juan-Diego Urbina and Jörg Wunderlich for their advice to better prepare for my defence. I am very honoured for the 2-week visiting position at MIT, so I would like to thank Phiala Shanahan and Will Detmold. Extended gratefulness is obliged to Andreas Kronfeld for the opportunity that I had to visit Fermilab and give a seminar there. Many thanks also to Gregorio Herdoiza for the 8-month virtual secondment to IFT in Madrid and all the interesting discussions about physics and everyday life. This work has received funding from the European Union's Horizon 2020 research and innovation programme under the Marie Skodowska-Curie grant agreement No. 813942 (ITN EuroPLEx). I am also happy to have met all the EuroPLEx fellows and other members of the network like in particular, Francesco di Renzo and Petros Dimopoulos. I would like to thank all the colleagues at the department I have interacted with for everyday conversations or coffee breaks, namely Simon Bürger, Davide Giusti, Daniel Jenkins, Marius Löffler, Lisa Walter, Philipp Wein, Simon Weishaüpl and Thomas Wurm. In particular, I would like to emphasize the technical support given by my office mates Simon Bürger and Thomas Wurm and the sysadmin Marius Löffler. Also, I am grateful to Philipp Wein for useful discussions about physics. This manuscript was proofread by Lisa Walter. A special mention goes to Nithin Thomas, a genuinely kind person with whom I shared very nice moments during this time and who has probably got to know me best. I want to acknowledge my best friends Alessio and Edoardo for the support that they have given me over these years. Last but not least, I would like to thank my beloved ones: my family and my girlfriend. I am extremely grateful to my family for their never-ending support and care, and it is also thanks to them if I reached this stage. Finally, I would like to thank my girlfriend Rossella for her objectivity in everyday conversations, love, support, and her precious help during the last writing of this dissertation.